PSFC/RR-02-4

Advanced Hydrotest Facility (AHF) Case II Quadrupole Design Study

Final Report

February 2002

Schultz, J.H., Radovinsky, A.L., Smith, B.A., Minervini, J.V.,
Myatt, R.L.*, Camille, R.J.Jr.*

Plasma Science and Fusion Center
Massachusetts Institute of Technology
Cambridge MA 02139 USA

* Myatt Consulting, Inc.
Norfolk MA 02056 USA

Advanced Hydrotest Facility (AHF) Case II Quadrupole Design Study

Final Report

Joel H. Schultz, A. Radovinsky, B. Smith, J.V. Minervini
M.I.T. Plasma Science and Fusion Center

R.L. Myatt and R.J. Camille, Jr.
Myatt Consulting, Inc.

February 26, 2002

AHF No: AHF-MIT-JHSchultz-010902-01

Table of Contents

I. Introduction

In present radiography facilities, magnetic lenses are made with normal, conducting coils. If these are to be upgraded to a next-generation facility with large-bore viewing capabilities, it is necessary to use superconducting magnets, because of their greatly reduced overall power requirements. The most important and costly component in a new facility would be the large-bore quadrupoles, used for focusing a proton beam. The purpose of this study is to identify a feasible design for a set of superconducting quadrupoles that achieve the specifications of the larger bore (Case II) and higher field-of-view radiography system.

Conventional superconducting quadrupoles are typically limited to bores of 0.7 m or to squared bore-flux density products of 0.7 T^2-m^2, because the forces on the conductor scale with size and flux density a conventional Rutherford cable would quench prematurely, because of conductor motion. A large-bore magnet requires conductor that has high load-carrying capability, high electrical integrity and excellent stability against mechanical training and nuclear heating. It is well known that the Cable-in-Conduit SuperConductor (CICC) has excellent properties in all three categories. This is why early studies done by MIT for the Los Alamos National Laboratory in 1999 focused on CICC solutions to large-bore magnetic lens designs. However, since that time, the magnetic lens specification has been relaxed so that the force requirements have been reduced by an order of magnitude, compared with the 1999 design. Instead of being an order of magnitude higher than any other quadrupole magnet, the forces on the Case II quadrupole lenses are comparable to other state-of-the-art magnets, such as the Thomas Jefferson National Accelerator Facility's (TJNAF) Hall C Q2 lens. This presents the possibility of making the lenses with conventional Rutherford cable or with Rutherford cable soldered into a copper channel (cable-in-channel). This has the benefits of less expensive conductor and winding and also develops smaller stresses when winding around a small radius in the end-turns. (A further advantage of designing about a Rutherford cable is the possibility of using some of the 100 km of free cable left over from the canceled Superconducting Supercoller (SSC) project, although, at present, the Muon-Electron Converter (MECO) at Brookhaven has precedence over AHF for the use of this cable). At present, conventional Rutherford cable is adopted for the smaller bore Case I quadrupoles and cable-in-channel for the larger bore Case II quadrupoles. The design is still state-of-the-art in lens size, if not an order-of-magnitude beyond it, suggesting that the cable-in-channel design, which is intermediate in cost/performance, but stronger and more easily protected than unreinforced Rutherford cable, should be the first alternative to CICC that is studied. This study searches for and finds a cable-in-channel solution to the LANL requirements for a large-bore quadrupole.

A key issue is that of stabilizing the conductor against bursts of nuclear heating during each pulse of high-energy protons. Within the option of cable-in-channel design, two suboptions are investigated as possible solutions. One suboption is to pot the windings, which has the advantage of high mechanical and electrical strength and of restricting the possibility of helium overpressure to small diameter coolant lines. The other suboption is to allow helium to permeate the winding pack. This has the disadvantages of being less stiff and permitting tracking along kapton tape surfaces. However, it has the advantage of providing a local helium reservoir and the possibility of removing most of the heat from a conductor after a nuclear heating or stick-slip event in only a few milliseconds. The slip-plane between the insulation and the conductor in this option may actually have mechanical design advantages, by eliminating shear in the insulation. A second method for increasing energy margin by an order of magnitude is the use of Nb_3Sn, instead of NbTi. The quantitative study of these two tradeoffs has been

deferred until CY2002, although the absorption and removal of high-energy nuclear heating is reported in Chapter 8.

The following report includes a Design Description Document and supporting analysis for the Case II quadrupole magnet system of the Advanced Hydrotest Facility (AHF). The interfaces with the Case I magnets and the Sample Under Test are included.

Chapter 1: Advanced Hydrotest Facility Overview

The following is a description of the AHF project and facility. An overview of the AHF facility, as it appears on a map of the Los Alamos National Laboratory is given in Figure 1.
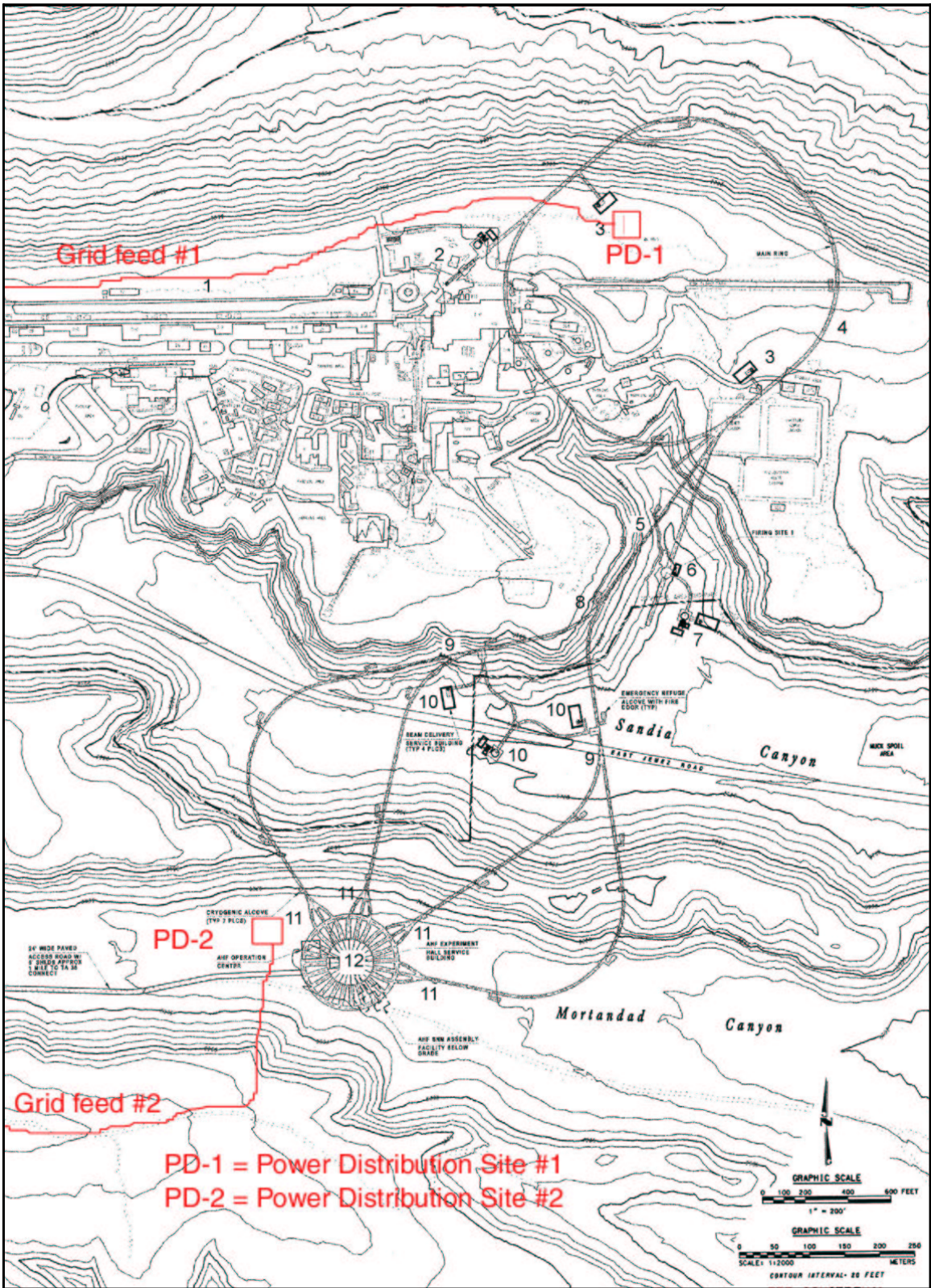
Figure 1: Overview of AHF facility at Los Alamos National Laboratory

The synchrotron has a circumference of 1200 m. A schematic diagram of AHF, including the synchroton, beam transport, and proton radiography system is given in Figure 2.
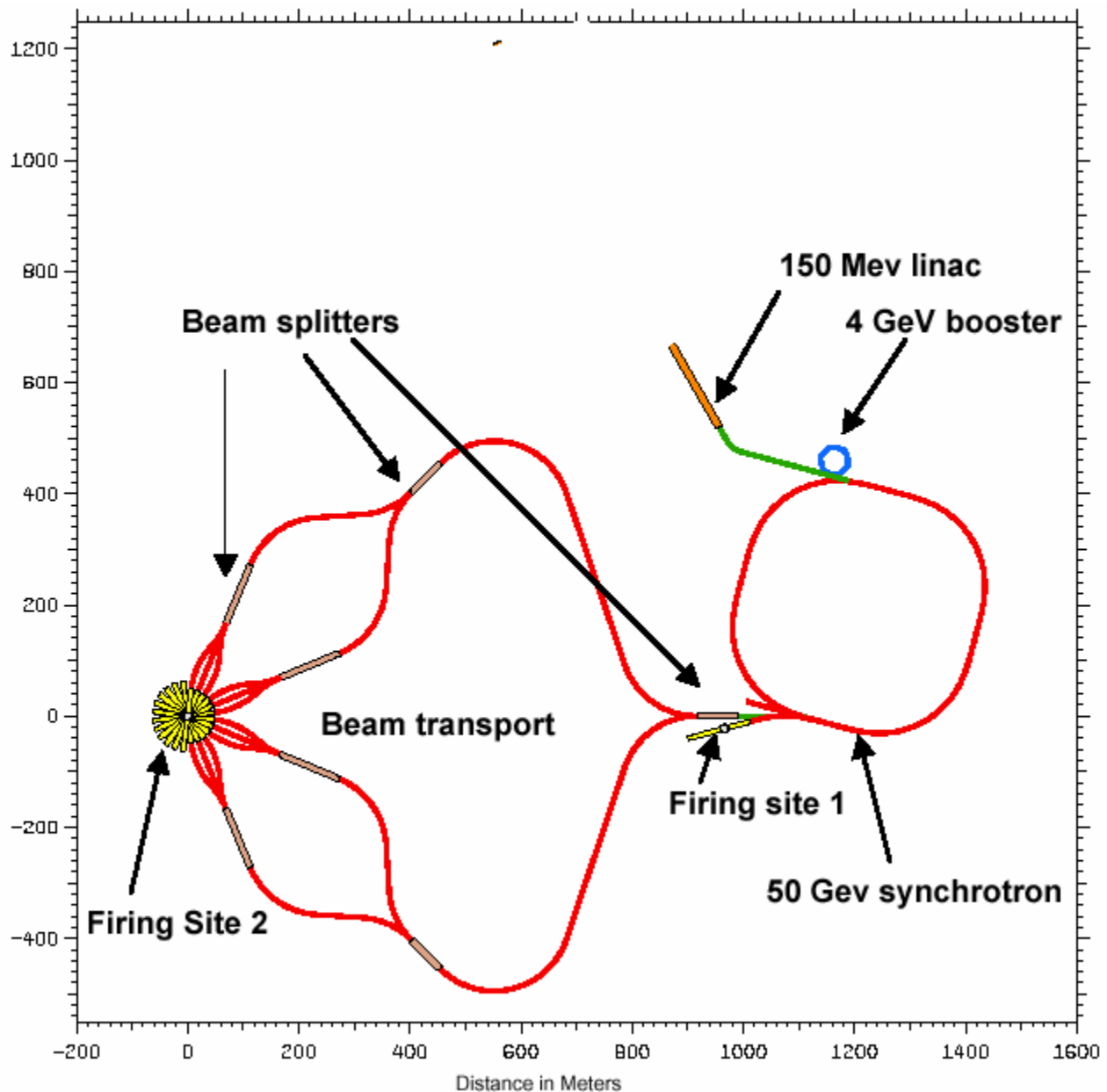
Figure 2: Schematic of AHF Beamlines

The HEBT lines transfer the beam to the illuminator and monitor lens magnets, then to the target. Further quadrupole "identity" lens magnets collect the beam after it passes through the target. Each downstream magnetic optical system includes two image planes. The array of medium Field of View (FOV) magnets (Case I) and high FOV magnets (Case II), surrounding the explosion chamber with the Sample Under Test, is shown in Figure 3. The cryogenic delivery system is also shown. The Case II magnets are in the smaller cryostats that are closer to the SUT. A single circular header supplies all twenty four of the magnet lines.
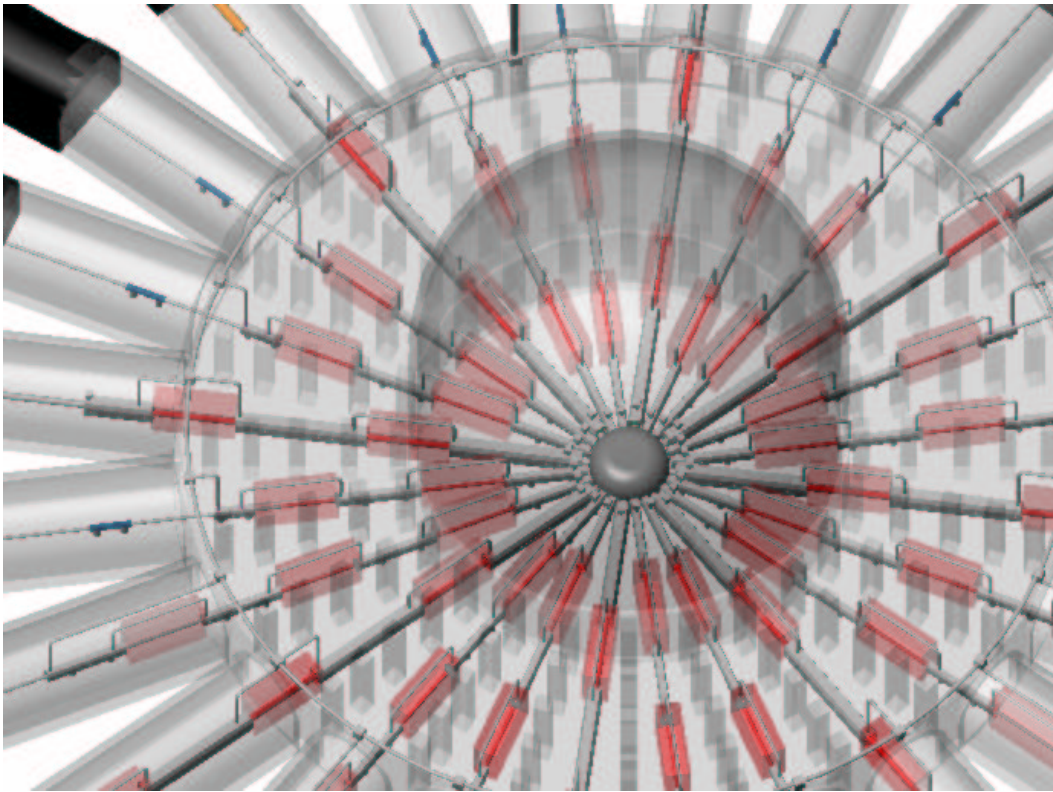
Figure 3: AHF Case I and Case II Magnetic Lens System, including Cryogenic Delivery System

An isometric cutaway of the AHF test cell is shown in Figure 4, showing the explosion chamber, the iron shields and gravity supports for Case I and Case II magnet lines, along with a beam tunnel.
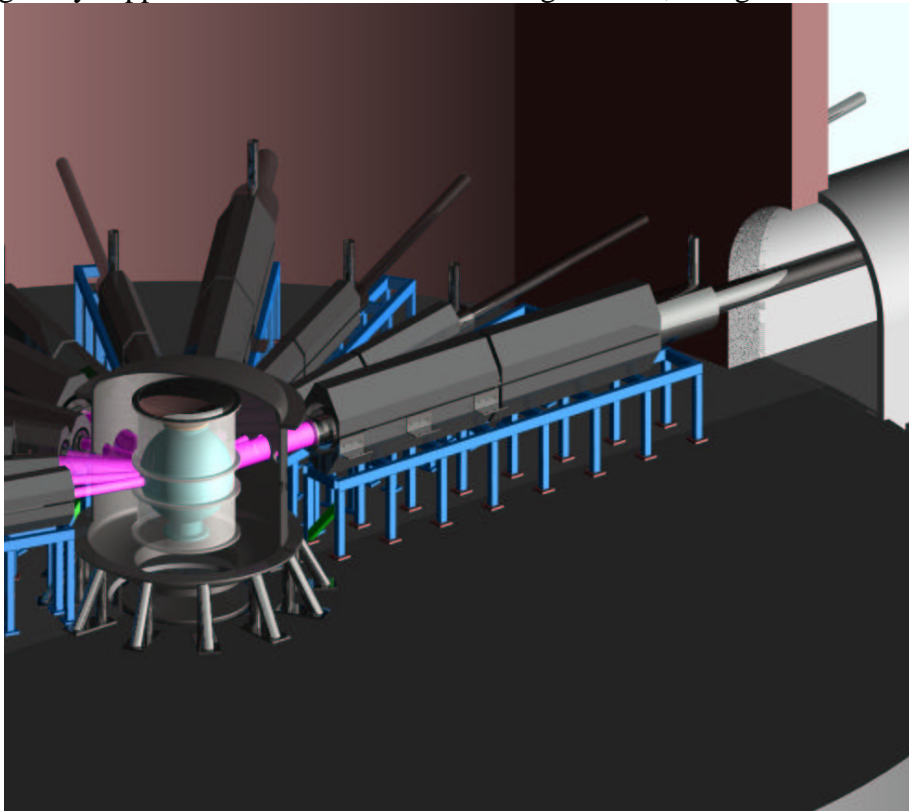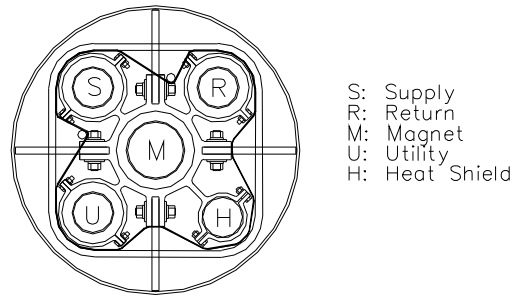

Figure 4: Isometric Cutaway of AHF Test Cell

A possible vacuum-jacketed helium transfer line to the magnets is illustrated in Figure 5.

Cross Sectional View of VJR

S: Supply
R: Return
M: Magnet
U: Utility
H: Heat Shield

Figure 5: Example of vacuum-jacketed helium transfer line to magnets

Each beam line has an illuminator and monitor lens upstream of the Sample Under Test and two sets of (Identity) Imaging Lenses downstream of the Sample Under Test. The three smaller coils in the illuminator are normal copper. The illuminator's pattern is the same on either side of the Monitor Lens, which allows confirmation of the beam pattern that will be illuminating the Sample Under Test, shown as a circle in Figure 6. After each of the imaging lenses, there is an imaging "plate", allowing two "snapshots" of the sample per imaging line. Snapshots can be repeated at high-frequency, creating "movies" of rapid hydrodynamic events. The use of multiple focusing lines allows viewing of the events from several different angles and even of tomographic imaging. A schematic of the magnetic optics system is given in Figure 6. The detailed topology of the magnetic optics system has been changing relatively frequently and this inventory is subject to change.
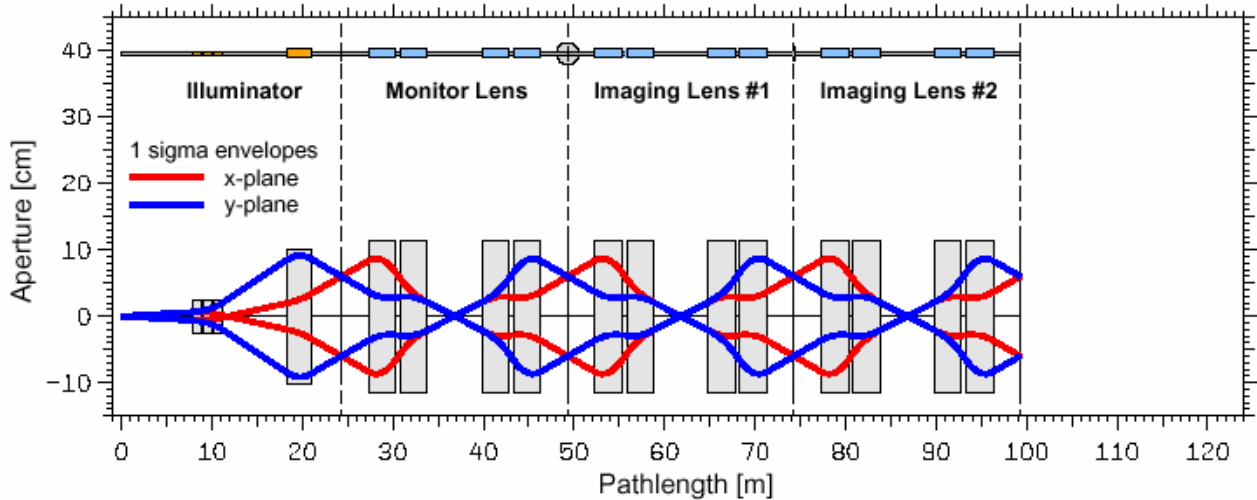

Figure 6: Magnetic Optics Focusing System, Case I or Case II

There are eight beam lines with the smaller FOV Case I identity lenses and four beam lines with the larger FOV Case II identity lenses. Each "Identity" or "Imaging" lens consists of four quadrupoles packaged in doublets. A doublet is a two quadupole set, housed in a single cryostat. Both quadrupoles in a doublet are identical, but one is rotated 90° with respect to the other, so that the beam is focused

along both axes in the x-y plane. Stated differently, the polarity of the current of each of the four coils in the "front" quadrupole of a doublet is opposite to the polarity of the coil whose axis is at the same angle in the "rear" quadrupole. Two doublets in series make a point-to-point focus unity lens. Including the monitor lens, there are three identity lenses per beam line. The large superconducting quadrupole in the illuminator may be identical with each of the four quadrupoles in an Imaging Lens, although it is depicted as being smaller. It is "fed" by three small copper quadrupoles. With the monitor lens, there are thirteen large-bore superconducting quadrupoles in each beamline. Therefore, the total number of quadrupole magnets is 156, of which 52 are the larger Case II quadrupoles. Each beamline has 6 doublet cryostats and there are total of 24 doublet cryostats in the Case II quadrupole system. A cost-saving option is to eliminate the monitor lens, which should reduce the cost of doublet cryostats by one-third. The inventory of superconducting quadrupole magnets and cryostats is given in Table I. The total number of imaging, monitor, and illuminating magnetic lens are given in Table II. I made these numbers up to force an accurate description.

Table I: Case I and Case II System Summary

Parameter	Case I (Small Lens)	Case II (Large Lens)
No. upstream (illuminator/monitor) lines	8	4
No. downstream (imaging) lines	8	4
No. quadrupoles/doublet	2	2
No. quadrupoles/imaging (identity) lens	4	4
No. imaging lenses/line	2	2
No. monitor lenses/ illuminator/monitor line	1	1
No. illuminating lenses/ illuminator/monitor line	1	1
No. quadrupoles/ illuminator/monitor line	5	5
No. quadrupoles/imaging line	8	8
No. quadrupoles, all illuminator/monitor lines	40	40
No. quadrupoles, all imaging lines	64	32
Total quadrupoles, system	104	52
Total singlets, system	8	4
Total doublets, system	48	24

The magnetic lenses themselves and their specified capabilities are described in Table II.

Table II: Case I (Small Lens) and Case II (Large Lens) Descriptions

Parameter	Units	Case I (Small Lens)	Case II (Large Lens)
FOV radius	(mm)	60	150
FOV angle	(mrad)	6	6
$R_{inner, \text{ beam pipe}}$	(mm)	114	241
$R_{inner, \text{ winding (approx)}}$	(mm)	182	330
Standoff distance	(m)	3	4
L_{quad}	(m)	3.1	4.25
Space between quad windings in doublet	(m)	0.5	0.4
Hard-edge equivalent quadrupole gradient	(T/m)	18.4	10.4
Winding average quadrupole gradient*	(T/m)	17.13	9.75
Central quadrupole gradient	(T/m)	18.58	10.14
Total lens length	(m)	25.4	33.8
Chromatic aberration coefficient T_{126}	(m)	34.7	46.2
Chromatic correlation coefficient W_x	(m^{-1})	0.12758	0.0964

* Integral of the gradient with respect to z for an isolated quadrupole, divided by the length of the windings

Chapter 2: Specifications

Magnet system specifications are taken from three documents, provided by LANL[1]. A complete set of self-consistent specifications doesn't exist in one document yet. This subchapter is based on an earlier attempt at synthesis[2] and modfied by the latest (Aug 23) of the LANL documents.

The Case I and Case II magnets must satisfy the following specifications:

        Case I. Gradient of 18.4 T/m, 26.7-cm-diameter bore, 3.0-m effective length

        Case II. Gradient of 10.4 T/m, 52.3-cm-diameter bore, 4.3-m effective length.

The warm bores are larger by 1.5 inches than the specified pipe apertures to allow space for the beam vacuum chamber and possible pipe expansion or motion during an explosive event. The beam tube is specified as having an inner diameter of 19"and an outer diameter of 20". This implies that the inner diameter of the cryostat may be no smaller than 23". In each case, cryostats were also designed to accommodate a doublet, with respective outer diameters of 64.6 cm and 97.8 cm. The magnet cryostats do not include an iron yoke for flux return. However, the design includes a warm iron shield to eliminate cross-coupling between Case I and Case II magnets.

Summary of Guidelines and Requirements

Conductor:
- Conductor shall be cable in channel.
- Conductor type (Nb_3Sn or NbTi) and cross-section (circular or rectangular) are TBD by MIT.
- Magnets shall be cooled by the forced-flow of two-phase helium through coolant pipes.

Windings:
- Windings shall be saddle-shaped (not racetracks).
- Coils shall be oriented to produce so-called Normal Quad fields (poles 45° from the horizontal and vertical axes).
- Quads within a doublet shall produce opposite field gradients.
- Axes of adjacent front-line quads (12 per side) shall be offset by 15° about the central target vertical axis.

Yoke/Shield:
- Case I & Case II quadrupoles shall include warm iron yokes in order to reduce error fields due to adjacent beamlines to levels consistent with overall error field specifications. The first iteration will assume a yoke with a 10 mm thickness at the equator.
- The standoff distance to the Case I quads shall be 3.0 m, where standoff is defined as the midpoint of the end turns. Assume that the boundary of the Case I quads is increased by a yoke with a thickness of 1 cm.

---

[1] P.L. Walstrom, "Case 2 Iron Yoke Specifications," AHF-LANL-PWalstrom-040901-01; P. L. Walstrom, LANSCE 1:-1-037 (TN), , "Geometric Aberrations in the AHF Quadrupole Lenses", Aug 8, 2001; P. L. Walstrom, "Magnetic Field Quality Specifications for the AHF Magnetic-Lens SuperconductingQuadrupoles," Aug. 23, 2001

[2] AHF-MIT-LMyatt-042001-01, R. L. Myatt and Joel H. Schultz, "Restatement of LANL FY01 Guidelines as Design Specifications," April 20, 2001

- Yokes shall be shaped to minimize the standoff distance
- Pion shielding is TBD by LANL but preliminarily achieved with a 1" thick pipe.

Field Quality and Shielding:
- 3D field analyses with saturable iron shall be used.
- Field quality requirements are defined below by LANL, as a fraction of the quadrupole field in the cross-section and integrated along the coils axis.
- Complete shielding requirements are TBD by LANL, but shall include the following: fields produced by either Case I or Case II quads (not both) at the 2.5 m radius iron sphere (centered at the firing point) and adjacent (zero-current) beam-lines, shall be kept below 10 gauss.
- End-turn shaping shall be used to reduce the need for correction coils. Correction coil currents or individual field error specifications are TBD.

The field quality specifications have been refined by Walstrom[3] to include three zones, as illustrated in Figure 7.
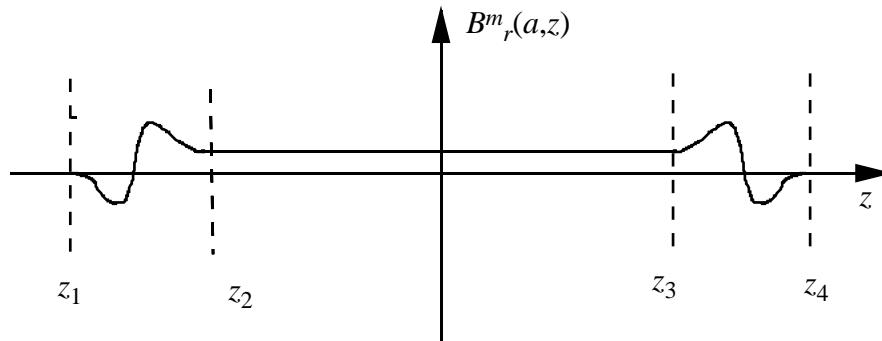

Fig. 7. Hypothetical profile of the mth Fourier component of B_r or B
on a cylinder of radius a in the bore of a single quadrupole magnet .

Since the effects of adjacent end-turns in a doublet aren't analyzed at this level, z1-z2 and z3-z4 are essentially identical. The general purpose of specifying the zones separately is to insist on low local field errors and not permitting equal and opposite field errors in the end turns and straight sections to cancel as a method of satisfying specifications.

The Fourier coefficients of the transverse field components on a reference cylinder of radius a with an axis that coincides with the magnet axis are defined for an arbitrary interval $[z_a, z_b]$ as

$$\int_{z_a}^{z_b} B_r(a,\theta,z)dz = \sum_{m=1}^{\infty}\left[a_m \sin m\theta - b_m \cos m\theta\right] \tag{1}$$

$$\int_{z_a}^{z_b} B_\theta(a,\theta,z)dz = \sum_{m=1}^{\infty}\left[c_m \sin m\theta + d_m \cos m\theta\right] \tag{2}$$

a_m and d_m are the normal Fourier coefficients. The skew Fourier coefficients $b_m = c_m$. All of the Fourier coefficients for integrated B_z are zero.

---

[3] P. L. Walstrom, "Magnetic Field Quality Specifications for the AHF Magnetic-Lens SuperconductingQuadrupoles," Aug. 23, 2001

The specified limits of the Fourier coefficients are:

Table III: Allowable Random Integral Field Errors in the AHF Lens Quadrupoles*

m value	Normal component over interval $[z_1, z_4]$	Skew component over interval $[z_1, z_4]$
2	5.0×10^{-4}	0**
3	1.0×10^{-4}	1.0×10^{-4}
4	1.0×10^{-4}	1.0×10^{-4}
5	1.0×10^{-4}	1.0×10^{-4}
6	1.0×10^{-4}	1.0×10^{-4}
7	1.0×10^{-4}	1.0×10^{-4}
8	1.0×10^{-4}	1.0×10^{-4}
9	1.0×10^{-4}	1.0×10^{-4}
10	1.0×10^{-4}	1.0×10^{-4}

*Allowable ratio of maximum in angular distribution of vector sum of integrated random field errors, m=3 to m=10 to the integrated quadrupole gradient is 2.0×10^{-4}.
**It is assumed that the as-built magnet is rotated until the integral skew quadrupole is zero. The dipole terms (m=1) are also assumed to be removed by alignment.

Table IV. Allowable Systematic Integral Field Errors in the AHF Lens Quadrupoles*

m value	Normal component over end intervals $[z_1, z_2]$ and $[z_3, z_4]$	Normal component over body interval $[z_2, z_3]$	Skew component over whole magnet interval $[z_1, z_4]$
3	$1.0 \times 10{-4}$	$1.0 \times 10{-4}$	1.0×10^{-4}
4	1.0×10^{-4}	1.0×10^{-4}	1.0×10^{-4}
5	1.0×10^{-4}	1.0×10^{-4}	1.0×10^{-4}
6	5.0×10^{-4}	5.0×10^{-4}	1.0×10^{-4}
7	1.0×10^{-4}	1.0×10^{-4}	1.0×10^{-4}
8	1.0×10^{-4}	1.0×10^{-4}	1.0×10^{-4}
9	1.0×10^{-4}	1.0×10^{-4}	1.0×10^{-4}
10	2.0×10^{-4}	2.0×10^{-4}	1.0×10^{-4}

*Allowable ratio of maximum in angular distribution of vector sum of integrated systematic field errors, m=3 to m=10 to the integrated quadrupole gradient is $6.0 \times 10^{-4.}$.
**It is assumed that the as-built magnet is rotated until the integral skew quadrupole is zero. The dipole terms (m=1) are also assumed to be removed by alignment.

Only the systematic errors are estimated during the preconceptual design period covered in the present Design Description Document.

Chapter 3: Case II Magnet Design Description-CY2001

The following is the design description of the Case II quadrupole for CY2001. The design for FY2000 was an air-core design without a tungsten shield[4]. For CY2001, the design has been modified to accommodate the iron core, tungsten shield, and the new specifications document[5].

IV.i Introduction – Large Bore Quadrupole Design

Conventional superconducting quadrupoles are typically limited to bores of 0.7 m or to squared bore-flux density products of 0.7 T^2-m^2. Because the forces on the conductor scale with size and flux density a conventional Rutherford cable would quench prematurely, because of conductor motion. A large-bore magnet would require conductor that has high load-carrying capability, high electrical integrity and excellent stability against mechanical training and nuclear heating. It is well known that the Cable-in-Conduit SuperConductor (CICC) has excellent properties in all three categories. This is why studies done by MIT for the Los Alamos National Laboratory in 1999 focused on CICC solutions to large-bore magnetic lens designs. However, since that time, the magnetic lens specification has been relaxed so that the force requirements have been reduced by an order of magnitude, compared with the 1999 design. Instead of being an order of magnitude higher than any other quadrupole magnet, the forces on the Case II quadrupole lenses are comparable to other state-of-the-art magnets, such as the Thomas Jefferson National Accelerator Facility's (TJNAF) Hall C Q2 lens. This presents the possibility of making the lenses with conventional Rutherford cable or with Rutherford cable soldered into a copper channel (cable-in-channel). This has the benefits of less expensive conductor and winding and also develops smaller stresses when winding around a small radius in the end-turns. A further advantage of designing about a Rutherford cable is the possibility of using some of the 100 km of free cable left over from the canceled Superconducting Supercollider (SSC) project, although it is now believed that this conductor will be used in the Muon-Electron COLlider (MECO). The design is still state-of-the-art in lens size, if not an order-of-magnitude beyond it, suggesting that the cable-in-channel design, which is intermediate in cost/performance, but stronger and more easily protected than unreinforced Rutherford cable, should be the first alternative to CICC that is studied. This study searches for and finds a cable-in-channel solution to the LANL requirements for a large-bore quadrupole.

A key issue is that of stabilizing the conductor against bursts of nuclear heating during each pulse of high-energy protons. Within the option of cable-in-channel design, two suboptions are investigated as possible solutions. One suboption is to pot the windings, which has the advantage of high mechanical and electrical strength and of restricting the possibility of helium overpressure to small diameter coolant lines. The other suboption is to allow helium to permeate the winding pack. This has the disadvantages of being less stiff and permitting tracking along kapton tape surfaces. However, it has the advantage of providing a local helium reservoir and the possibility of removing most of the heat from a conductor after a nuclear heating or stick-slip event in only a few milliseconds. The slip-plane between the insulation and the conductor in this option may actually have mechanical design advantages, by eliminating shear in the insulation.

---

[4] AHF Report No: AHF-MIT-JHSchultz-061200-01, Joel H. Schultz, R.J. Camille, Jr., R. Leonard Myatt, A. Radovinsky, B. Smith, and R.J. Thome, "Proton Radiography Quadrupole Lens Designs for the Advanced Hydrodynamics Facility (AHF) Final Report," July 12, 2000

[5] P. L. Walstrom, "Magnetic Field Quality Specifications for the AHF Magnetic-Lens SuperconductingQuadrupoles," Aug. 23, 2001

IV.ii Case II Design Description

Two quadrupoles are combined as a quadrupole "doublet" in a single cryostat. The two quadrupoles are seriesed through joints in the space between them and a single pair of leads exits through the service stack. The service stack also provides feedthroughs for the helium coolant and instrumentation lead pairs. The coils are inside the liquid helium can, which may either be actually flooded with liquid helium or be dry, containing liquid helium coolant pipes, tracing the inner surface of the can. The intermediate thermal shield is a thin cylinder of steel or aluminum, covered with multilayer superinsulation, and cooled by intermediate temperature helium vapor. The use of nitrogen is avoided, because of the danger of an asphyxiation accident in the subterranean test cell. The outer vacuum can consists of an outer and inner steel cylinder, connected by end flanges and permitting penetration of the beam line.

The cryostat for the Case II quadrupole is illustrated in Figures 8 and 9. The radial dimensions of the cryostat are listed in Table V.
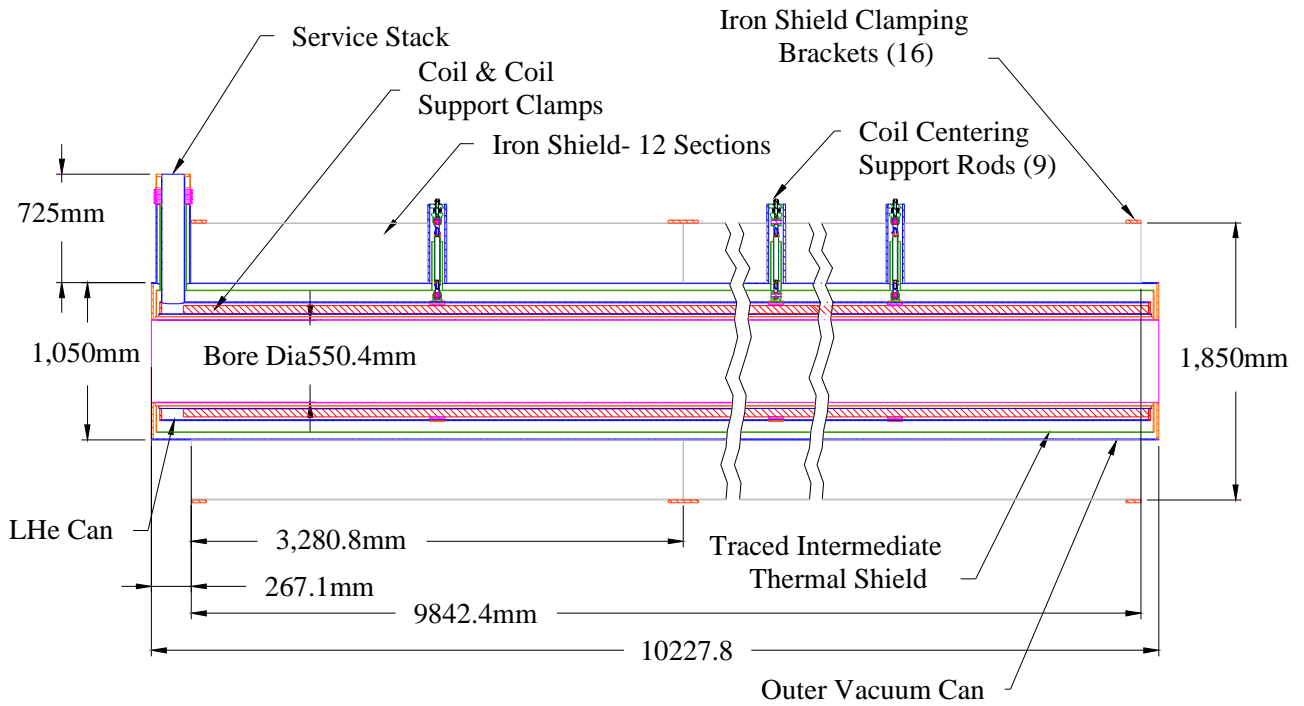
Figure 8: Case II Cryostat Dimensions

SECTION C-C
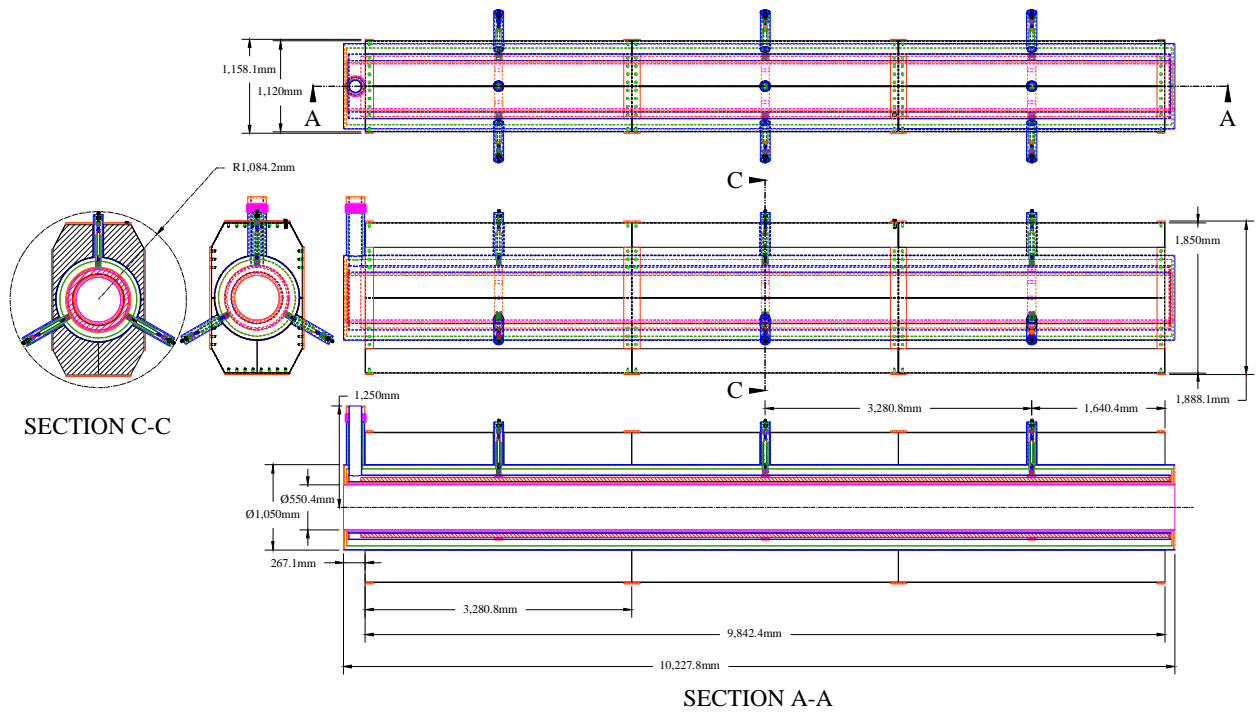
SECTION A-A

Figure 9: Case II Cryostat Envelope, Dimensions, and Cross-Sections with Iron Shield

Table V: Case II Cryostat Major Component Dimensions, Sizes, and Weights

	R_o	R_i	Length	Volume	Weight
				(m^3)	(kg)
Windings & Winding Support	371.55	317.70	9945.60		
Iron Yoke			9842.4		
4K Outer Sup Ring (3ea)	402.7	396.35	100.00	0.00478	38
4K Bore Tube	315.70	312.53	10126.15	0.06345	510
4K Outer Tube	396.35	390.00	10126.15	0.15885	1276
4K End Flange (2ea)	390.00	315.70	12.70	0.00418	34
80K Bore Tube	296.65	293.65	10164.25	0.05655	506
80K Outer Tube	474.60	471.43	10164.25	0.09591	857
80K End Flange (2ea)	471.43	296.65	6.35	0.00536	48
Coil Outer Support Ring (3ea)	393.35	371.95	100.00	0.01544	124
Vac Bore Tube	278.36	275.18	10227.75	0.05647	453
Vac Outer Tube	525.00	518.65	10227.75	0.21294	1710
Vac End Flange (2ea)	518.65	278.36	12.70	0.00764	61
Bellow_Adapt	114.30	111.13	91.98	0.00021	2
Stack 80K Flng	85.90	76.20	5.43	0.00003	0.2
Stack-Vac-4K	111.13	76.20	17.20	0.00035	3
Coil Outer Support Ring	393.35	371.55	100.00	0.00524	42
4K Outer Sup Ring	402.70	396.35	100.00	0.00159	13
80K-Supprt Washer	33.05	18.20	3.00	0.00001	0.1
80 K Stack	85.90	82.73	571.00	0.00096	7.7
4K Stack	76.20	75.00	854.00	0.00049	3.9
Vac Stack	114.30	111.125	522.00	0.00117	9.4
Total				0.69	5697.31

* Note: Coil & Coil Support Tube Weights Not Included Table V: Coil and Cryostat Dimensions
The Case II quadrupole layout is described in Table VI and illustrated in Figure 10.

Table VI: Case II Quadrupole Winding Dimensions

Parameter	Units	Value
Rinner + gndwrap	(mm)	317.7
Rinner, conductor	(mm)	317.0
Router + gndwrap	(mm)	351.5
Router, conductor	(mm)	350.8
tgndwrap	(mm)	0.5
tins, turn	(mm)	0.2
tins, interlayer	(mm)	0.4
nturns, inner		68[6]
nturns, outer		37
θ_1 (pole to inner layer)	(degrees/radians)	7.7/0.134
θ_2 (pole to outer layer)	(degrees/radians)	25.5/0.445
NIquad	(MAT)	
Bmax, center	(T)	4.28
Bmax,end turns	(T)	5.01
Wm,quadrupole	(MJ)	5.85
Wm,doublet	(MJ)	11.7
Lcoil	(m)	4.46
Lmagnetic	(m)	4.25
Lstraight length	(m)	3.95
Lcond, quad[7]	(m)	4,003

The maximum flux density at the center of the straight leg is 4.28 T, while the maximum flux density at the end turns is estimated to be 5.01 T[8].

The windings are not "cos 2θ", but simply select the angles of the inner and outer layers of the winding in order to eliminate the 6th and 10th harmonics in the straight section[9]. The Dummy Turn Winding Spacer consists of dead turns that are added to the outer layer to square-off the winding cross section and to maintain a consistent structural medium. Circumferential compression in the coil pack is obtained by winding the turns around a solid core, and applying a radial precompression before welding an outer 3 cm thick stainless steel shell. The solid winding core is made of titanium, since a trade study showed that it had lower stresses than a stainless steel core[10]. There is no radial winding bobbin in the completed coil.

The angles extended by the winding pack are given in Table II and Figure 10.

---

[6] AHF-MIT-LMyatt-102601-01, R.L. Myatt, "Re-Optimized End Turns in the Case II Quadrupole," October 26, 2001
[7] ibid
[8] AHF-MIT-LMyatt-072301-01, R.L. Myatt, "2D Turn-Count Optimization for Revised Case II Quad Shield Design," July 23, 2001
[9] AHF-MIT- ALRadovinsky-051700-01, Rev. 0, A.L. Radovinsky, " Elimination of the Field Harmonics in a 2D Model of a Quadrupole with Discrete Conductors," May 17, 2000
[10] AHF-MIT-LMyatt-091901-01, R.L. Myatt, "2.5D Stress Analysis of Shielded Case II Quadrupole," September 19, 2001
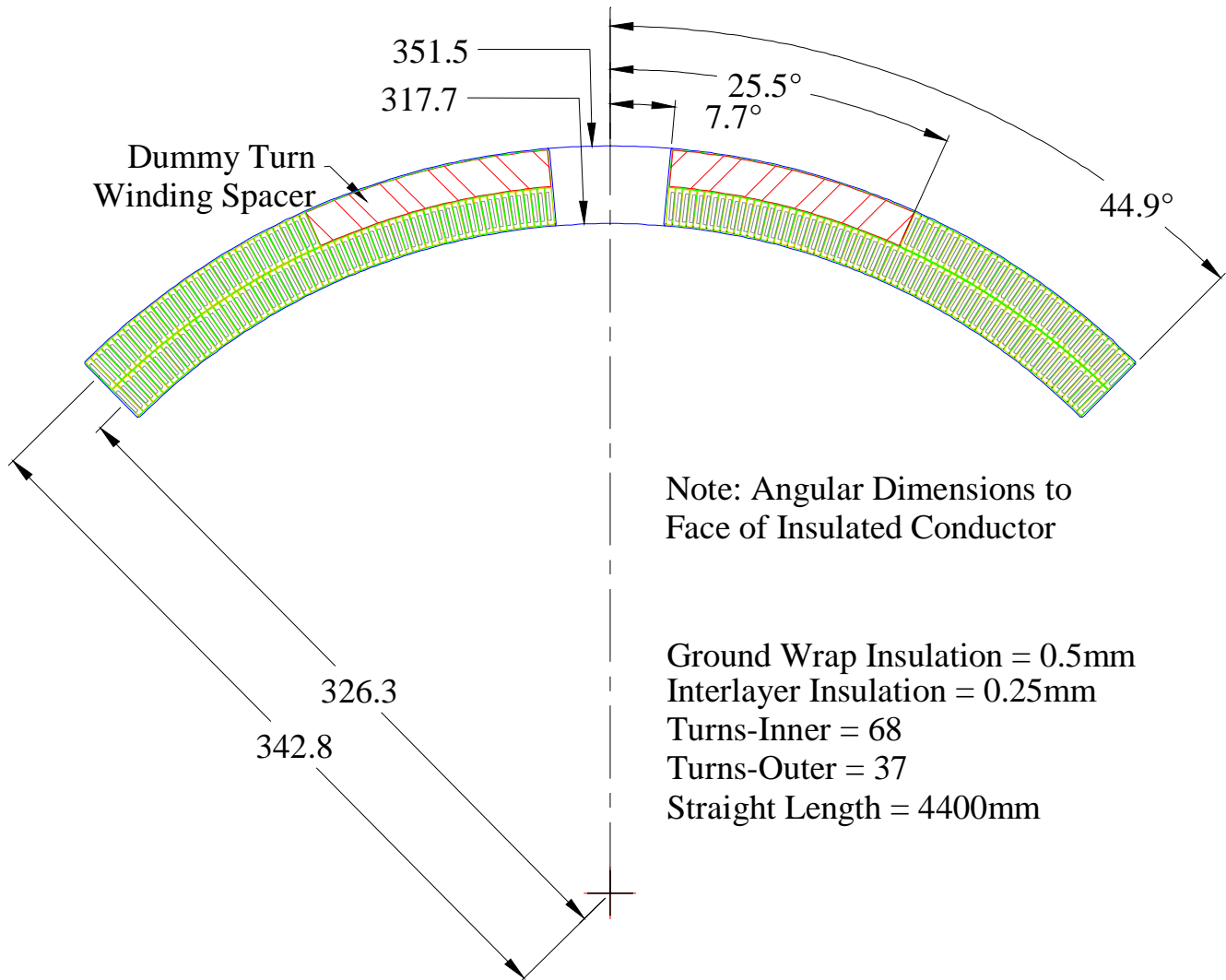
Figure 10: Winding Cross-Section, Case II Quadrupole Design

The iron shield reduces the leakage field from each magnet at its neighbor's beam-line to negligible levels (< 10 gauss). It also has the benefit of enhancing the quadrupole field from the superconducting magnet. The shield has the unusual orientation of being thick on top and thin at the equator, in order to allow stacking shields radially about the Sample under Test with the maximum Field of View. Instead of the normal NEWS orientation of the quadrupoles, the four poles are at NE-SE-SW-SE, so that each magnet can be "pointing" at a thick section of the shield. The polarities of the currents in each of the two quadrupoles in a doublet are rotated by 90 degrees, so that the beam can be focused in two directions.
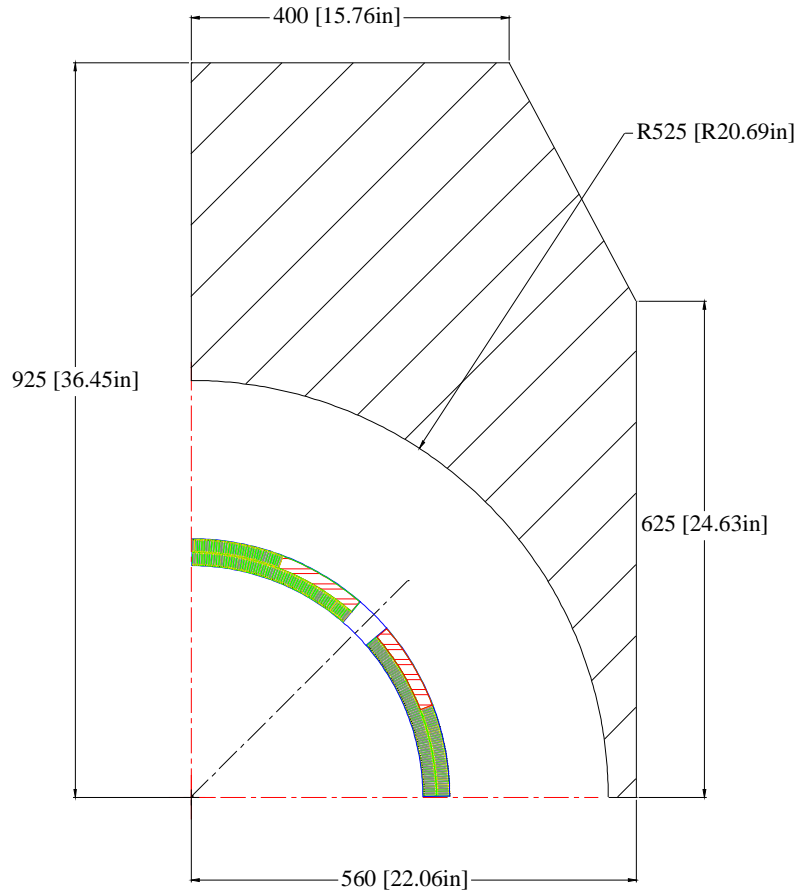
Figure 11: Elevation Cross-section of Winding and Iron Shield

The iron shield is divided into 12 sections, three axial divisions by four sections poloidal sections. Each poloidal section is aligned with one of the NE, SE, SW, and NW quadrupole windings, as shown in Figures 13-15.
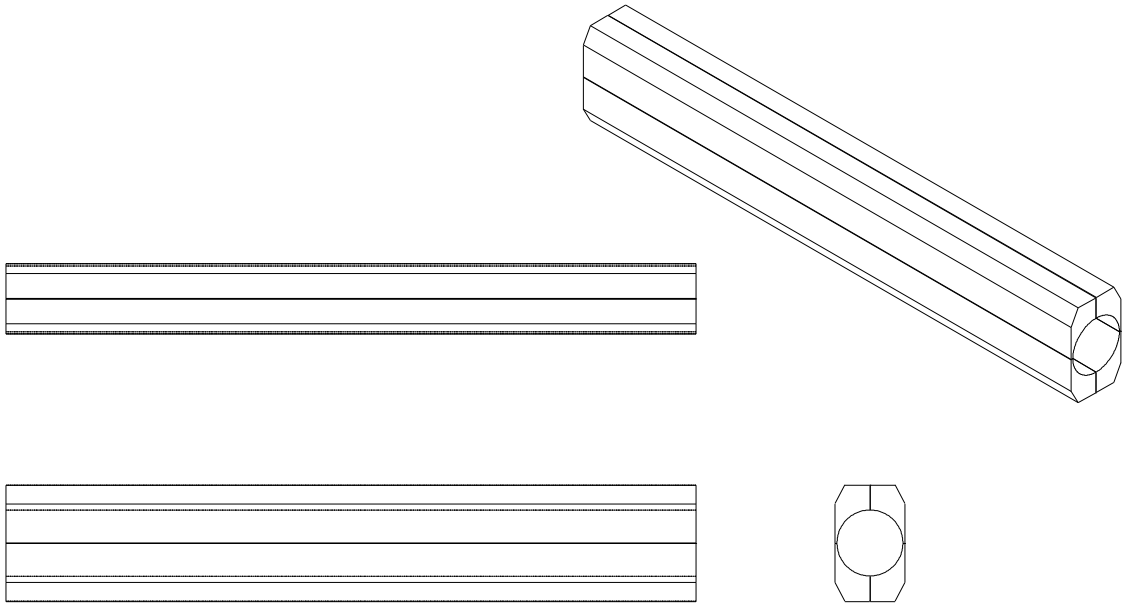
Figure 13: Iron Core
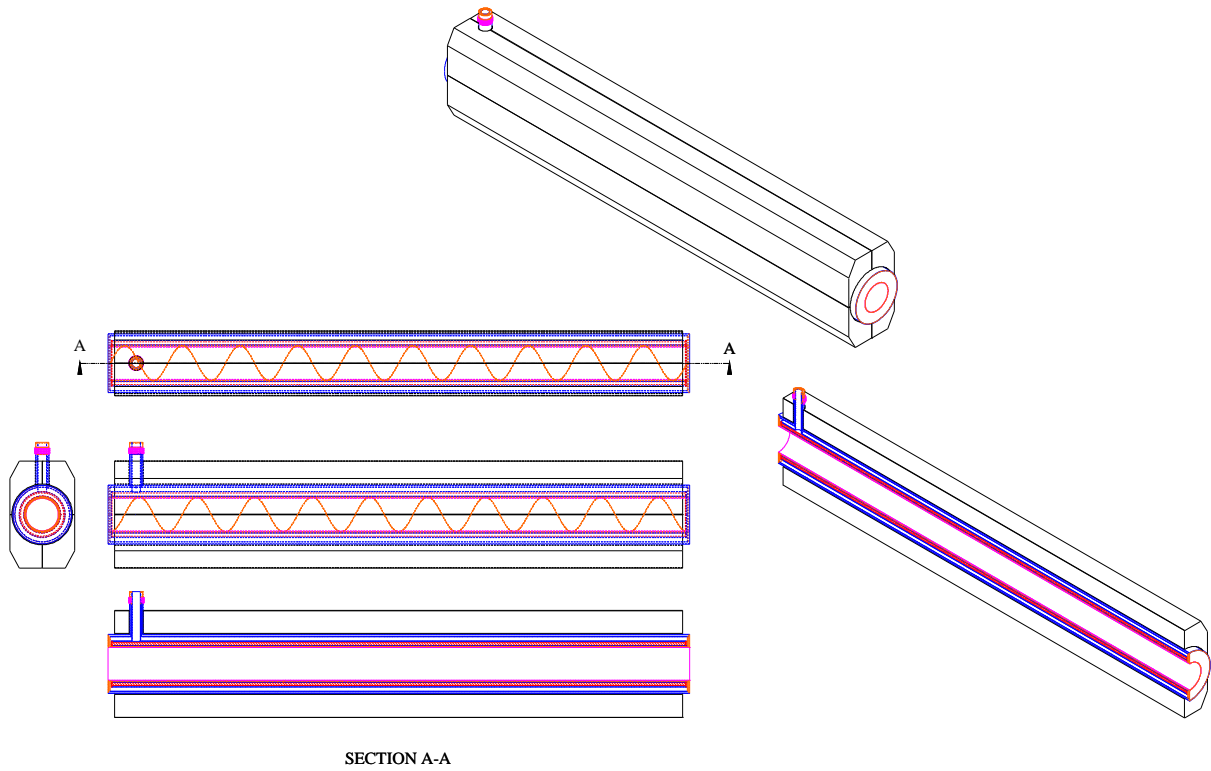
SECTION A-A

Figure 14: Isometric, cutaway, and elevation views of Case II Magnet and Iron Shield
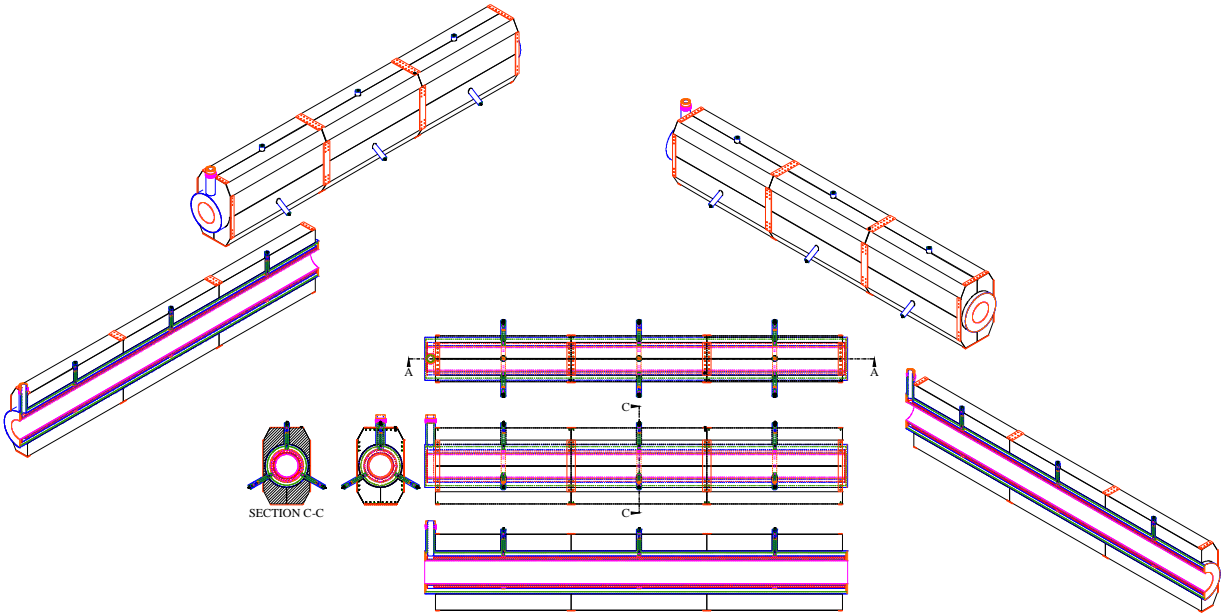
Figure 15: Isometrics and Elevation Views of Cryostat and Iron Shield

The end turns are arranged in a saddle configuration with spacers. There are three spacers in both inner and outer layer end turns. The spacers don't lie exactly on top of each other, but were selected by an ANSYS® optimization routine, minimizing the z1-z2 and z3-z4 integrals of the 6th and 10th harmonics[11].Figure 15a incorrectly states that there are 69 turns in the Inner Layer, when there are now 68, as listed in Table VI. One turn was removed by Myatt, who discovered that this level of "fine-tuning" in the winding was necessary and sufficient to satisfy the field quality specifications.

---

[11] AHF-MIT-LMyatt-092601-01, R. Leonard Myatt, "2D Spacer Optimization for Shielded Case II Quads," September 26, 2001
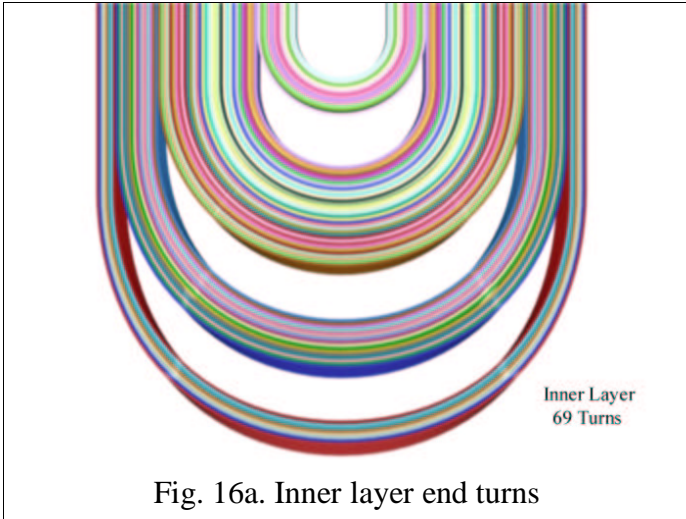
Fig. 16a. Inner layer end turns
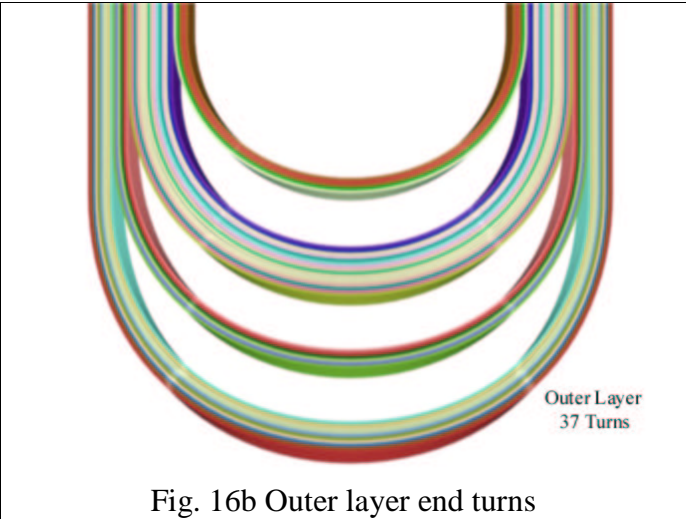
Fig. 16b Outer layer end turns
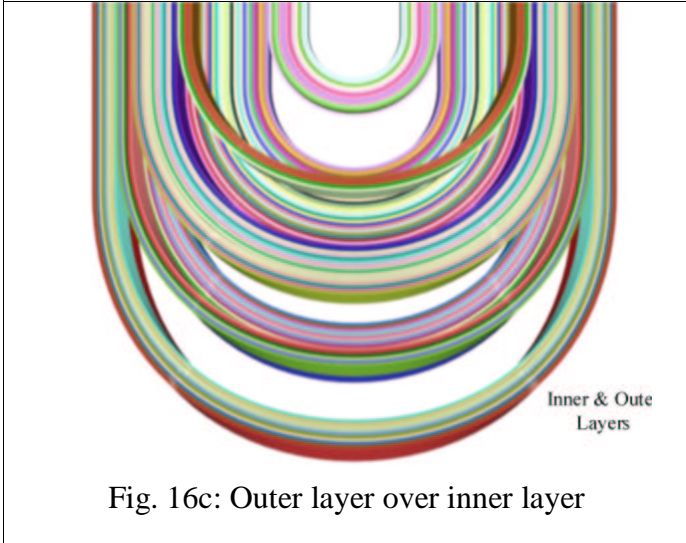
Fig. 16c: Outer layer over inner layer
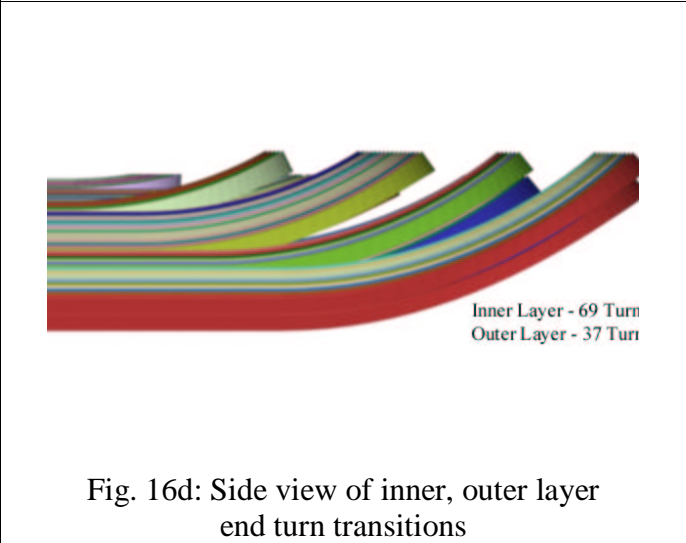
Fig. 16d: Side view of inner, outer layer end turn transitions
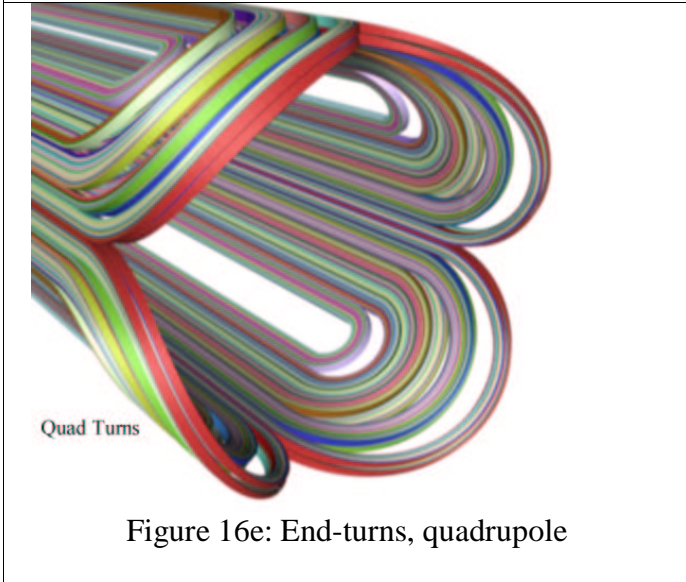
Figure 16e: End-turns, quadrupole
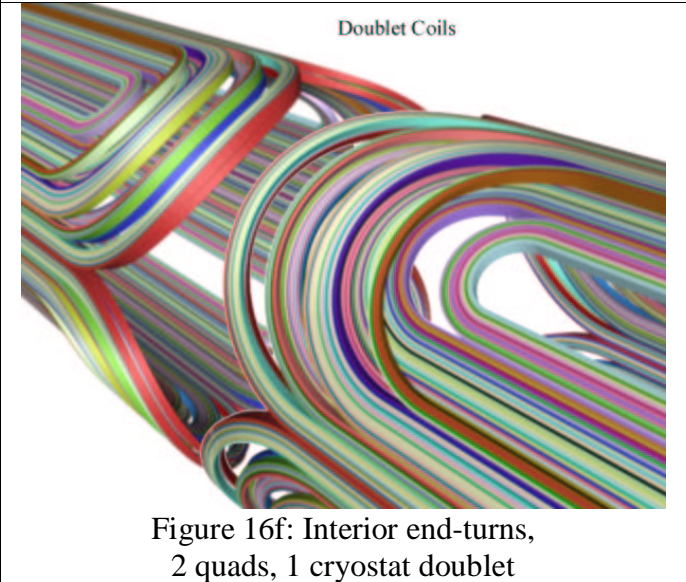
Figure 16f: Interior end-turns, 2 quads, 1 cryostat doublet

Chapter 4. Conductor Design

The conductor is a Rutherford cable in a copper C-channel, as illustrated in Figure 12. The dimensions of the cable-in-channel are listed in Table VII. The design is based on SSC Inner Layer cable, although the design itself does not depend upon the availability of SSC Cable.

Table VII: SSC Cable-in-Channel Conductor Dimensions

Parameter	Units	Value
henv	(mm)	16.3
wenv	(mm)	3.0
hchannel	(mm)	15.9
wchannel	(mm)	2.6
hcablespace	(mm)	12.3
wcablespace	(mm)	1.623
Dstrand	(mm)	0.808
nstrands		30
Cu/Noncu		1.3
tins	(mm)	0.2
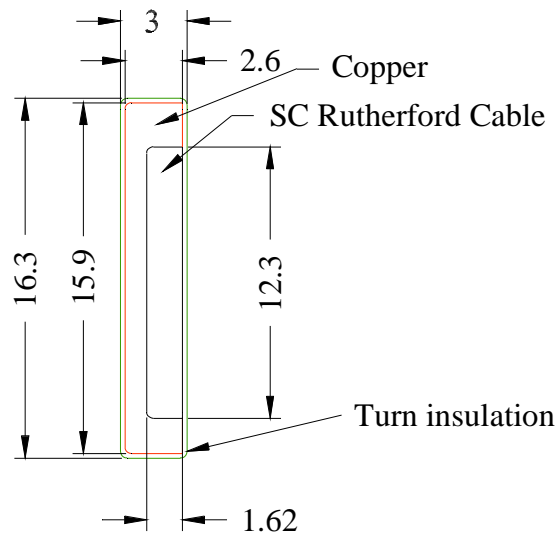
Figure 12
Cross-section of AHF Quadrupole Turn per AHF-MIT-JHSchultz-052300-01

23

Table VIII: Conductor Performance Specifications

Parameter	Units	Value
B_{max}	(T)	5.01
NI	(MAT)	3.084
$N_{turns,quad}$		420
I_{cond}	(kA)	7.343
A_{noncu}	(mm^2)	6.370
$A_{cu,cond}$	(mm^2)	8.28
$A_{cu,channel}$	(mm^2)	21.4
$A_{cu,total}$	(mm^2)	29.66
J_{noncu}	(A/mm^2)	1153
J_{cu}	(A/mm^2)	248

Chapter 5: Cryostat Design

The cryostat provides a 4.2 K helium environment for two quadrupole magnets (a doublet) and includes a helium can, an intermediate temperature helium-cooled shield and an outer vacuum can. The cryostat has a single service stack for leads, coolant lines, and instrumentation feedthroughs. Outlines and isometric cutaways of the interior vessels and the windings, along with the service stack are shown in Figures 17-18.
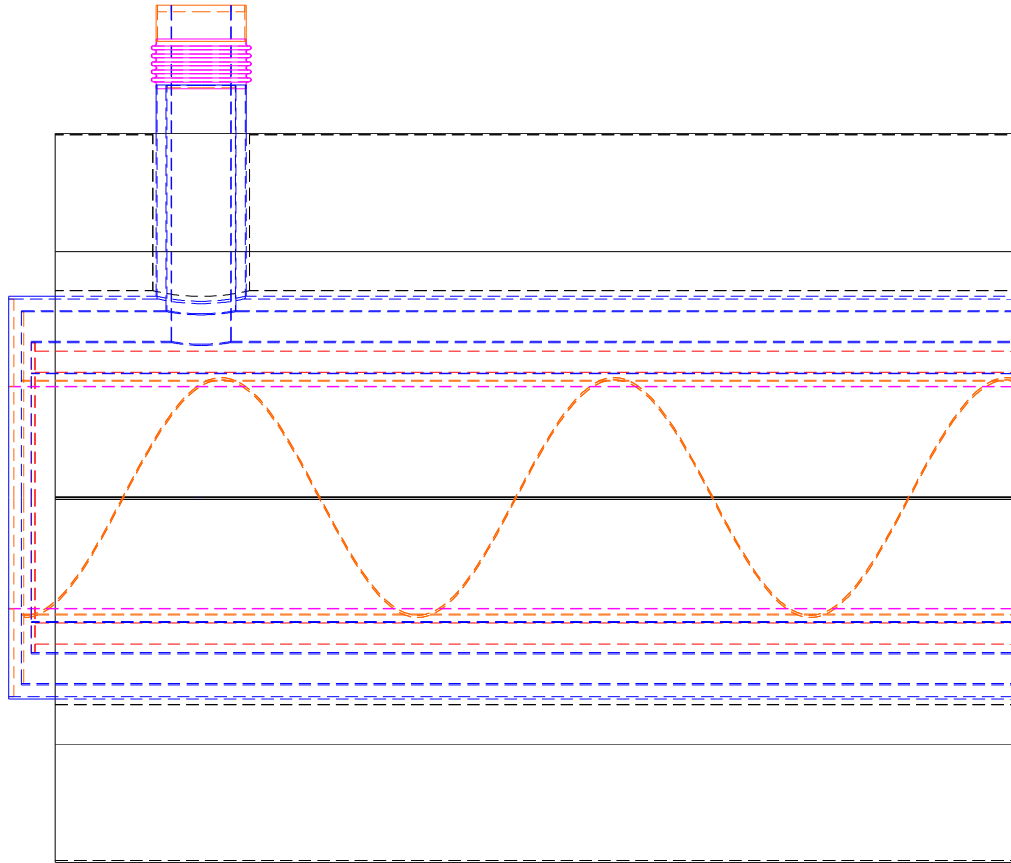
Figure 17: Upstream end of Case II cryostat with lead stack
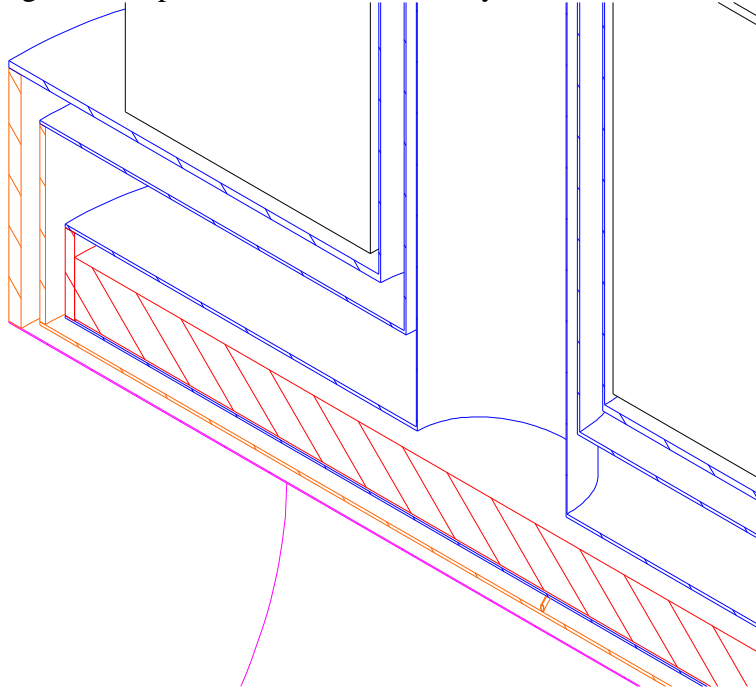
Figure 18: Isometric cutaway of Case II coil, cryostat and lead stack

An elevation section of the cryostat, iron shield, service stack and gravity supports is shown in Figures 19a and 19b.
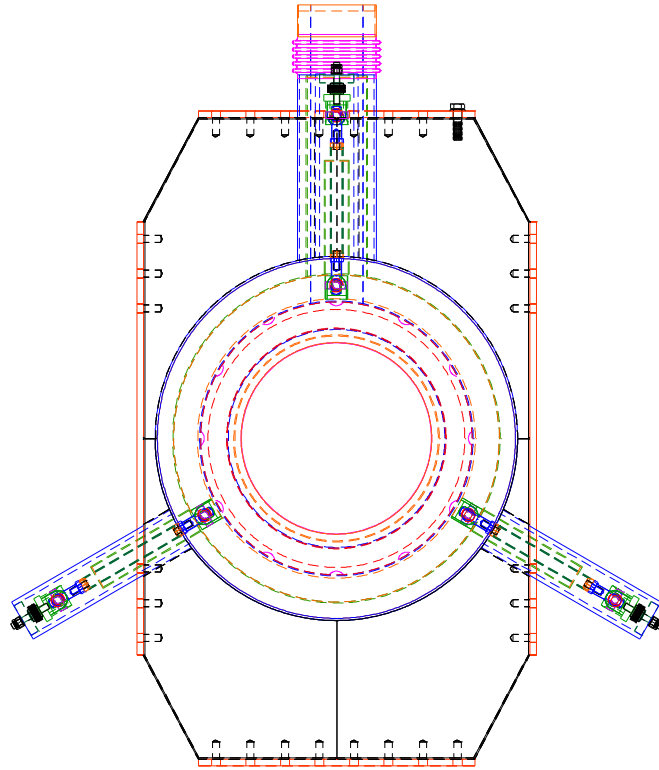
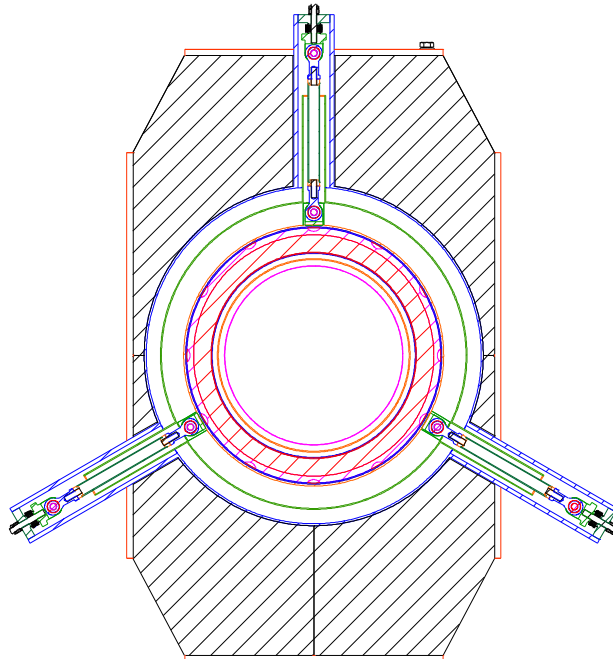Figure 19a: Cryostat, Cold Mass, Iron Shield and Gravity Supports with Lead Stack

Figure 19b: Cryostat, Cold Mass, Iron Shield and Gravity Supports
An external isometric view and a cutaway of the entire cryostat, iron shield, and gravity support system for a doublet are shown in Figures 20a and Figure 20b.
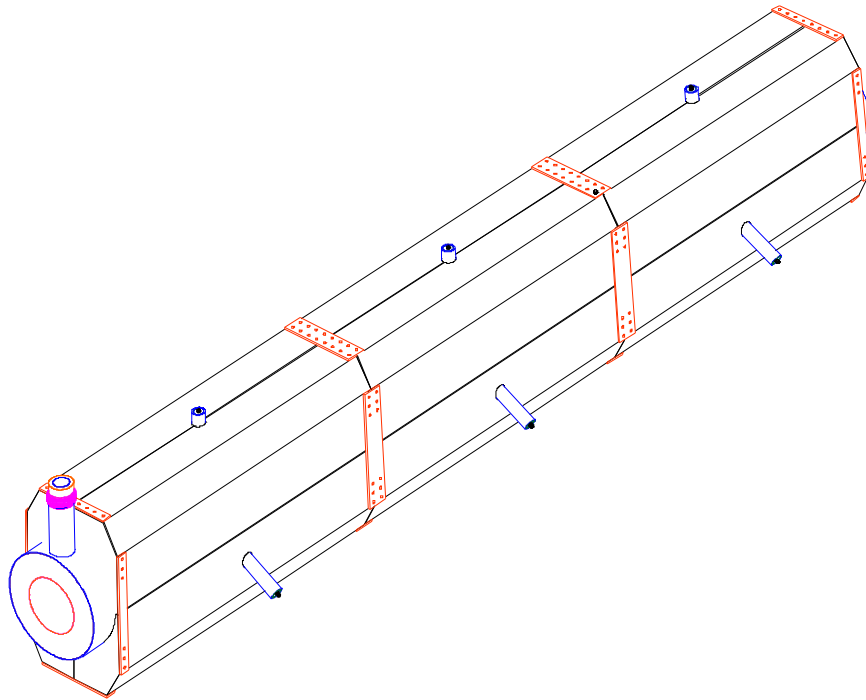
Figure 20a: Isometric of Cryostat, Iron Shield Sections and Straps, Lead Stack, and Gravity Supports
The iron shield is divided into twelve pieces, joined by bolted steel straps. There are three axial
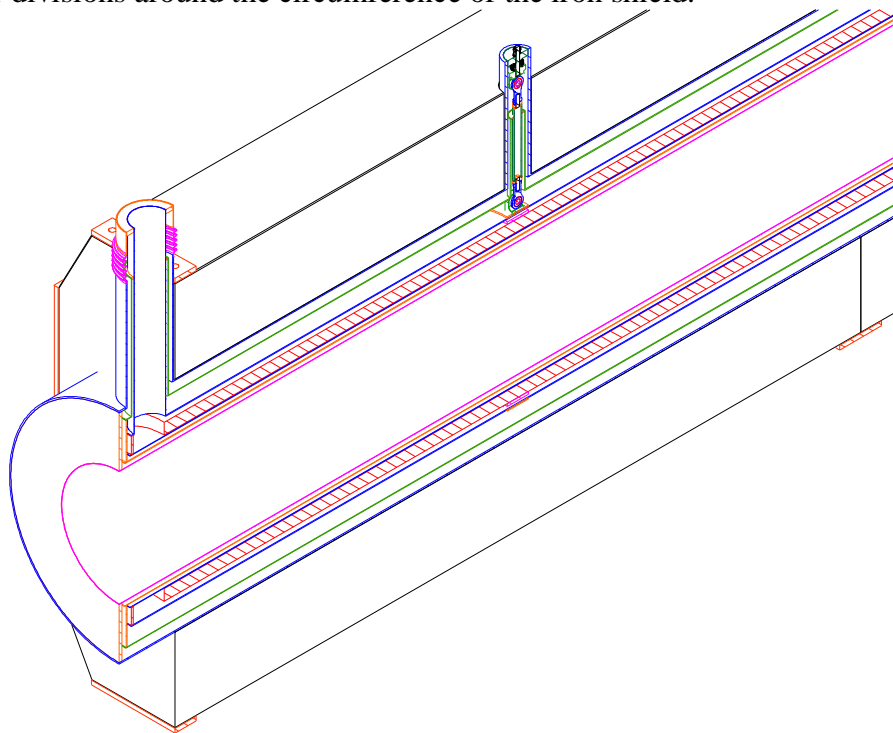divisions and four divisions around the circumference of the iron shield.

Figure 20b: Isometric Cutaway of Cryostat, Winding, Gravity Support, and Lead Stack

The interface between the Case I and Case II coil system iron shields is shown in Figure 21.
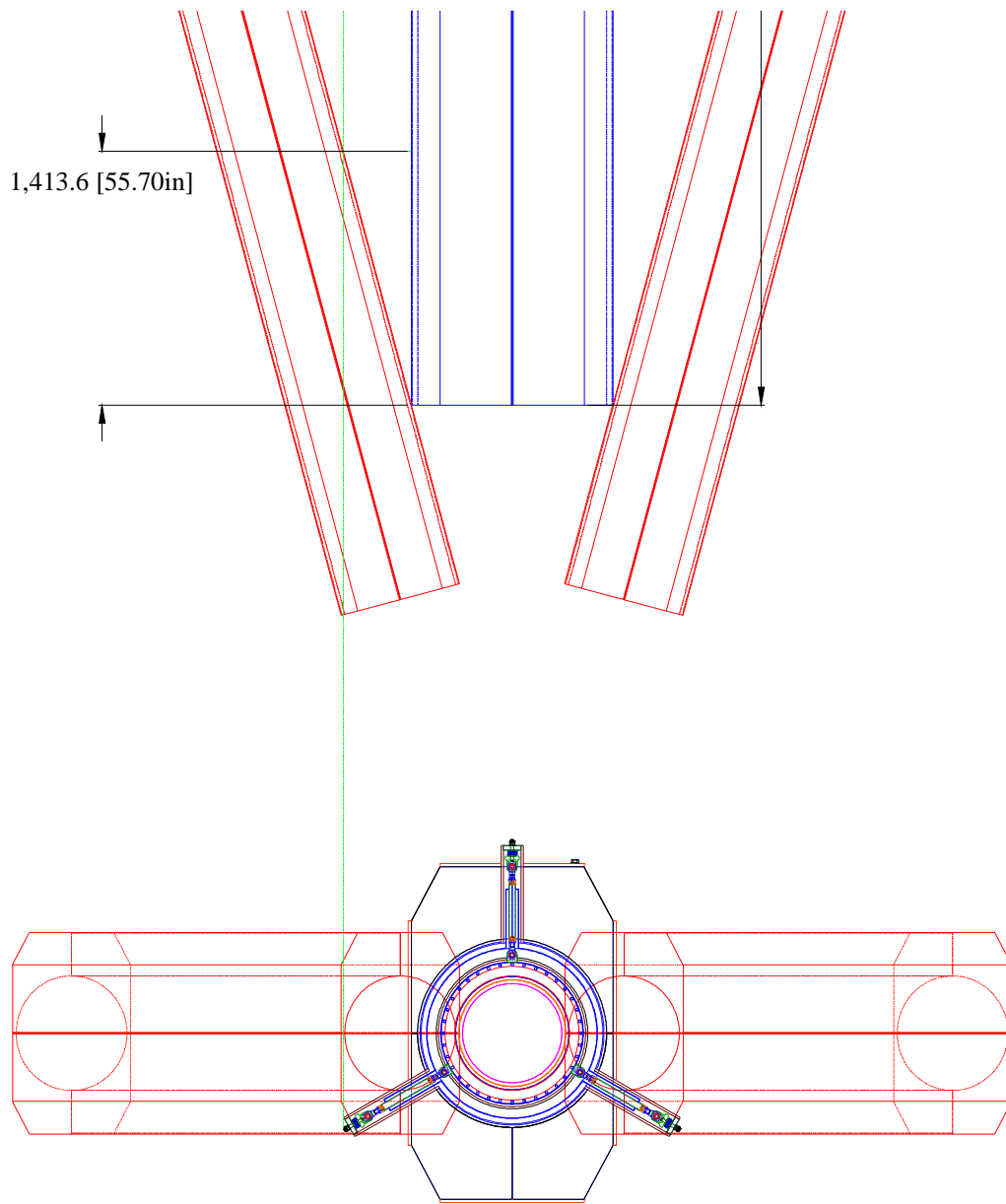
1,413.6 [55.70in]

Figure 21: Plan and Elevation Views of Case Cryostat and Iron Shield and adjacent Case I Iron Shields

28

A solid model of the iron shield (blue), gravity supports (gray), and service stack (gray) is shown in Figure 22.
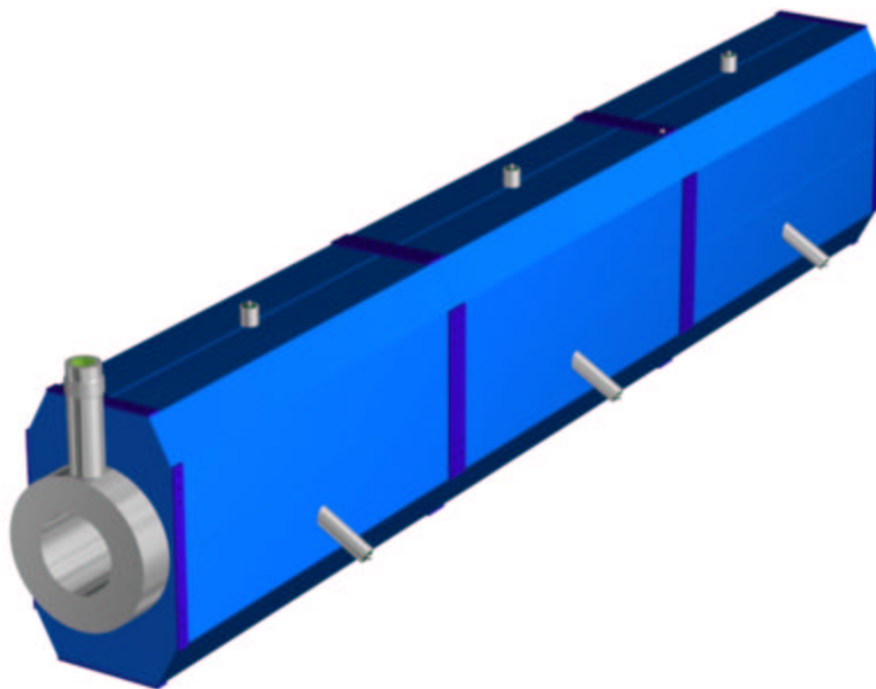

Figure 22: Solid Model lsometric of Cryostat, Iron Shield, and Gravity Supports

A cutaway in Figure 23, shows the cryostat (gold), and the internal components of the lead stack and the gravity supports. The green cylinder is the 80 K shield.
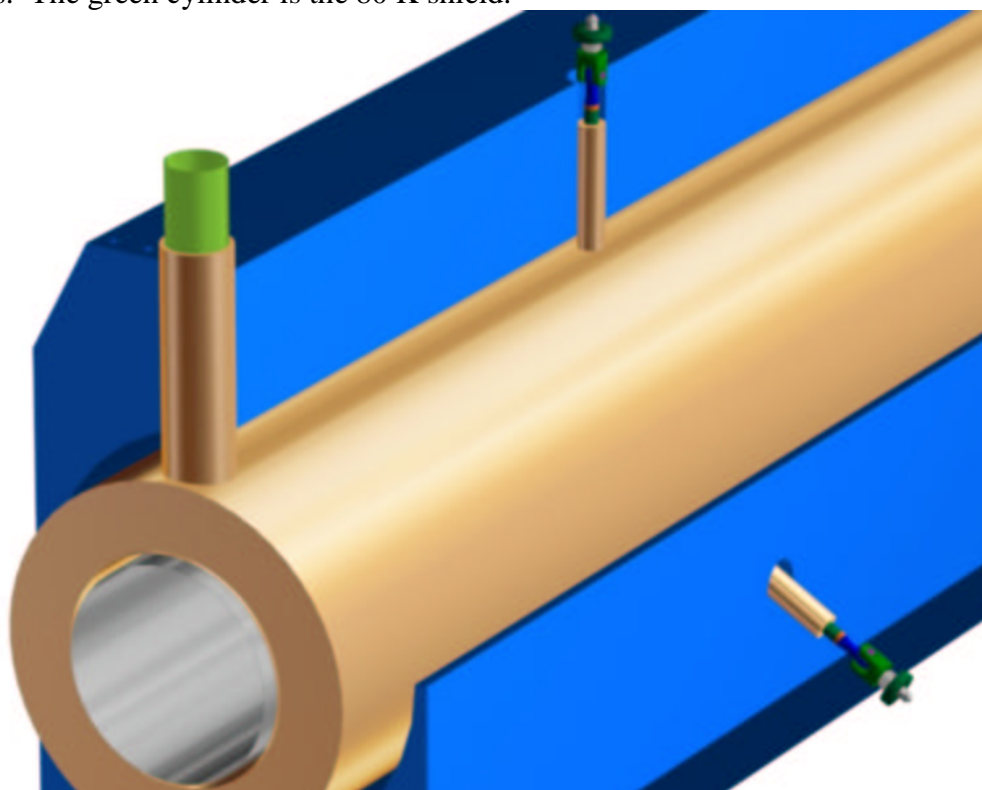

Figure 21: Solid Model of Cryostat and Iron Shield with Cutaways of Gravity Supports and Lead Stack with Helium Vessel Extension
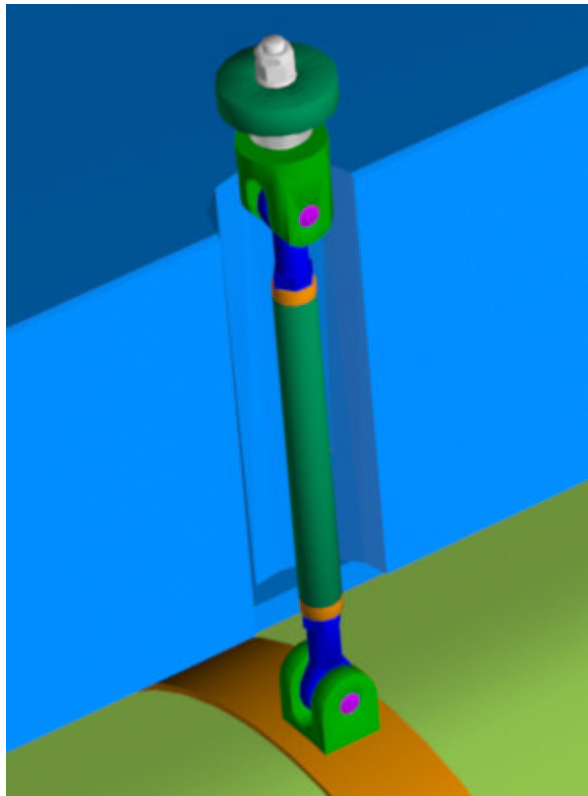
Figure 22: Solid model of a gravity support assembly

Figure 23 shows a solid model of the coil surfaces in the cryostat. The inner surface (grey) is the vacuum can, the gold is the tip of the intermediate temp shield, the green cylinder is the helium can, and the thick red can is the winding and winding support tube. The pink band is one of three supports about that coil that transfer loads to the outer can and gravity supports. The grooves are for helium flow, either through a flooded winding or helium pipes.
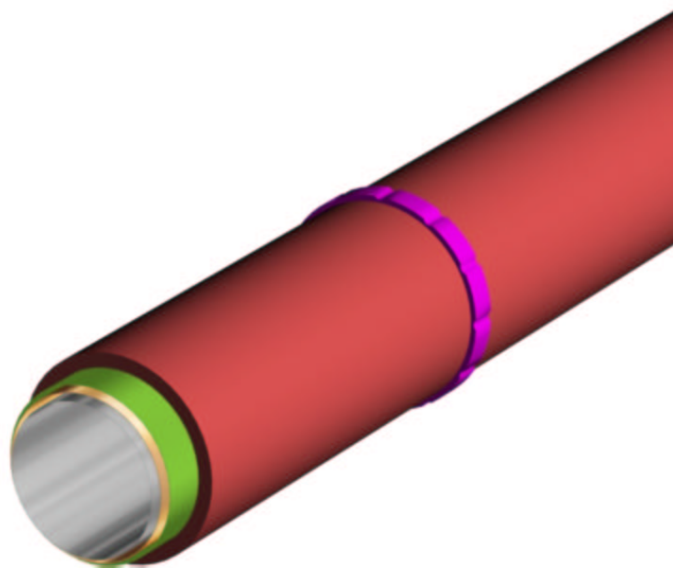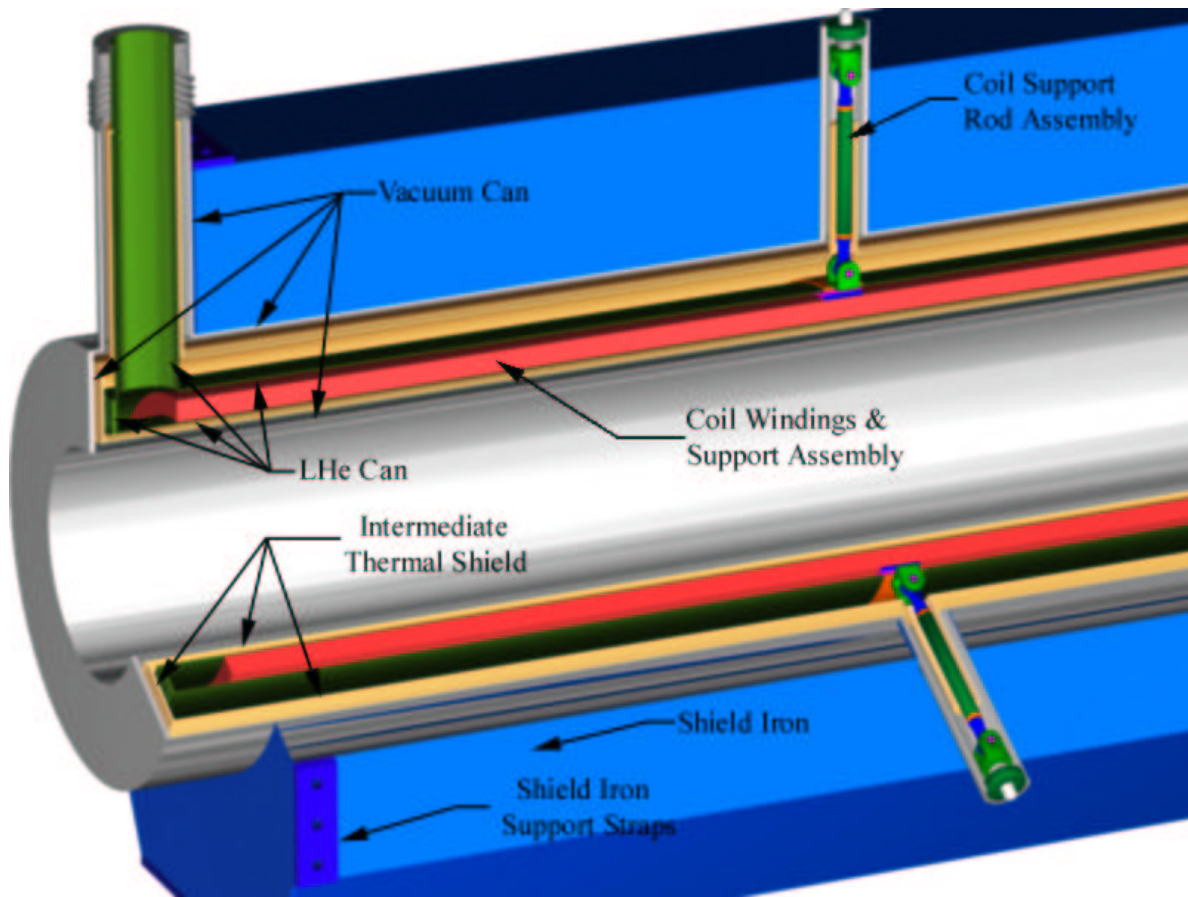

Figure 23: Coil and cryostat

Figure 24: Cutaway solid model of coil and cryostat with service stack and gravity supports. The plenum labeled Intermediate Thermal Shield is filled with gaseous helium at approximately 80 K in order to satisfy safety concerns about the use of nitrogen in an enclosed tunnel. The 80 K heat station at the leads reduces the thermal losses by about a factor of two over a conducting rod without an intermediate heat station.
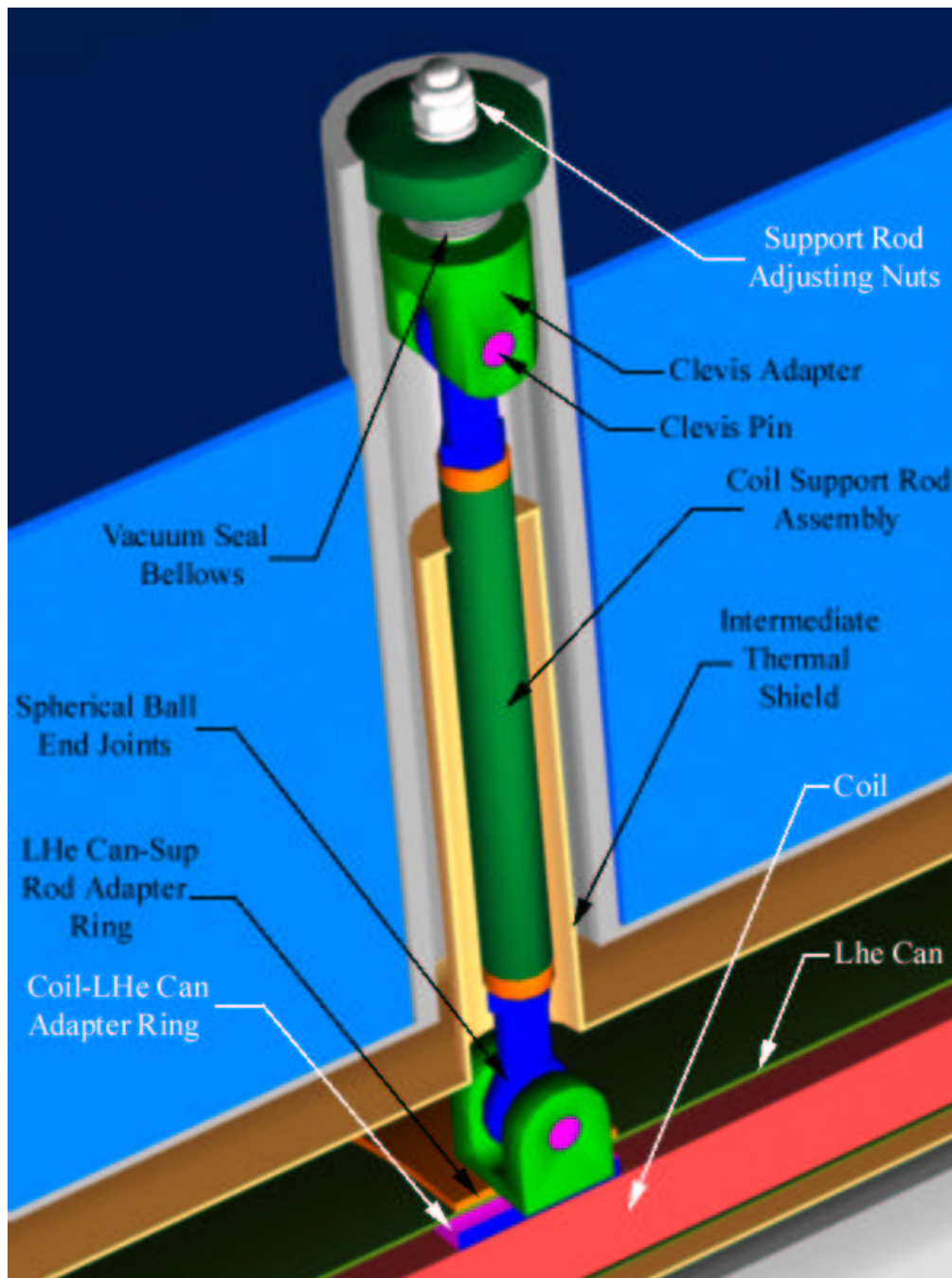
Figure 25: Gravity Support Rod

Figure 27 shows the cold-warm gravity supports for the cold mass. Thermal isolation is achieved by selecting the optimum length/area for the stainless steel coil support rod assembly. Relative contraction of the assembly and the cold mass during a cooldown is taken up in the bellows, which also provides a vacuum seal between the cryostat and adjusting nut volumes. The adjusting nuts are used for magnetic centering of the cold mass in the cryostat. The intermediate temperature shield to reduce radiation losses in the gravity supports is an extension of the helium cooled intermediate temperature shield of the cryostat. The attachment "ring" in the picture is actually a flexible braid, allowing relative motion between the shield and the support rod assembly. Each rod terminates in a ball and pin that are rigidly attached to each other, and that can slide along and rotate about the axis of the pin through the adapter bearing. All unbalanced magnetic forces, as well as the gravitational loads, are taken in tension or

compression through the seats of the clevis pin-bearing assemblies. The top of the supported rod is seated through the nut and top washer assembly. The bottom is supported by the coil-liquid helium can adapter ring and the liquid helium can-support rod adapter ring. The coil-Lhe can adapter ring is fit around the perimeter of the coil, and is one of the rings constricting radial motion of the coil. It has penetrations that allow axial helium flow. The Lhe Can-Support Rod Adapter ring runs around the perimeter of the coil, close to the intermediate thermal shield, and is shown extending on both sides of the coil support rod assembly.

Chapter 6 Field Analysis

The main performance parameters are the field gradient and field gradient integrals. The main error components are the 6th and 10th harmonics and the leakage field in the Case I beamspace. The calculated coil Case II Coil performance is summarized in Table 6-I:

Table 6-I: Case II Coils Performance Summary

Parameter	Units	Value	Specification
Central Field Gradient	(T/m)	10.4	10.4
Integral Gradient $\int(A_2(z)/r)dz$	(T)	47	44.7
$L_{magnetic}$	(m)	4.5	4.3
Bo, magnet	(T)	4.28	
Bmax, magnet	(T)	5.01[12]	
Harmonic Radius	(m)	0.2413	0.2413
$B_{leakage}$, Case I beamline, peak	(mT)	0.1[13]	1[14]

The field errors are compared to the allowable values in Table 6-II:

Table 6-II: Comparison of errors ($\int A_m dz/\int A_2 dz$) to Allowable values[15]

m Value	Z0 to Z3 or Z2 to Z3 (Body-Region)	Z3 to Z4 or Z1 to Z2 (End-Region)	Allowable Error
6	0.14×10^{-4}	0.89×10^{-4}	5.0×10^{-4}
10	0.43×10^{-4}	0.34×10^{-4}	2.0×10^{-4}

Fig. 6.1 is a plot of the flux lines in the model cross-section. The most significant elements of the design are captured in the ANSYS plot title. Notice that the current (7273 A) has been adjusted to produce the design-basis 10.30 T/m.

- Harmonic radius: 241.3 mm
- Field gradient: 10.30 T/m
- Normalized 6th and 10th harmonic coefficients: 0.0013% and 0.0032%

[12] AHF-MIT-LMyatt-072301-01, R.L. Myatt, "2D Turn-Count Optimization for Revised Case II Quad Shield Design," July 23, 2001

[13] AHF-MIT-LMyatt-0720-01, R. Leonard (Len), "Fringe fields at the Case II Beam, Revised Winding Radius," July 20, 2001

[14] AHF-LANL-PWalstrom-040901-01, Peter Walstrom, "Case 2 Iron Yoke Specifications," April 9, 2001

[15] AHF-MIT-LMyatt-102601-01, R.L. Myatt, "Re-Optimized End Turns in the Case II Quadrupole," October 26, 2001

- Inner and outer layer turns + spacers: 69 and 38
- Voided turn locations: 51 (inner layer), 13 (outer layer)

The flux density in the conductor cross-section is shown in Fig. 6.2. The peak (2D) value is reported to be 4.3 T (unchanged from the previous design). It is important to note that the voided turn location is based on counting from the outer turn. A close inspection of the turns in this figure will confirm this nomenclature.
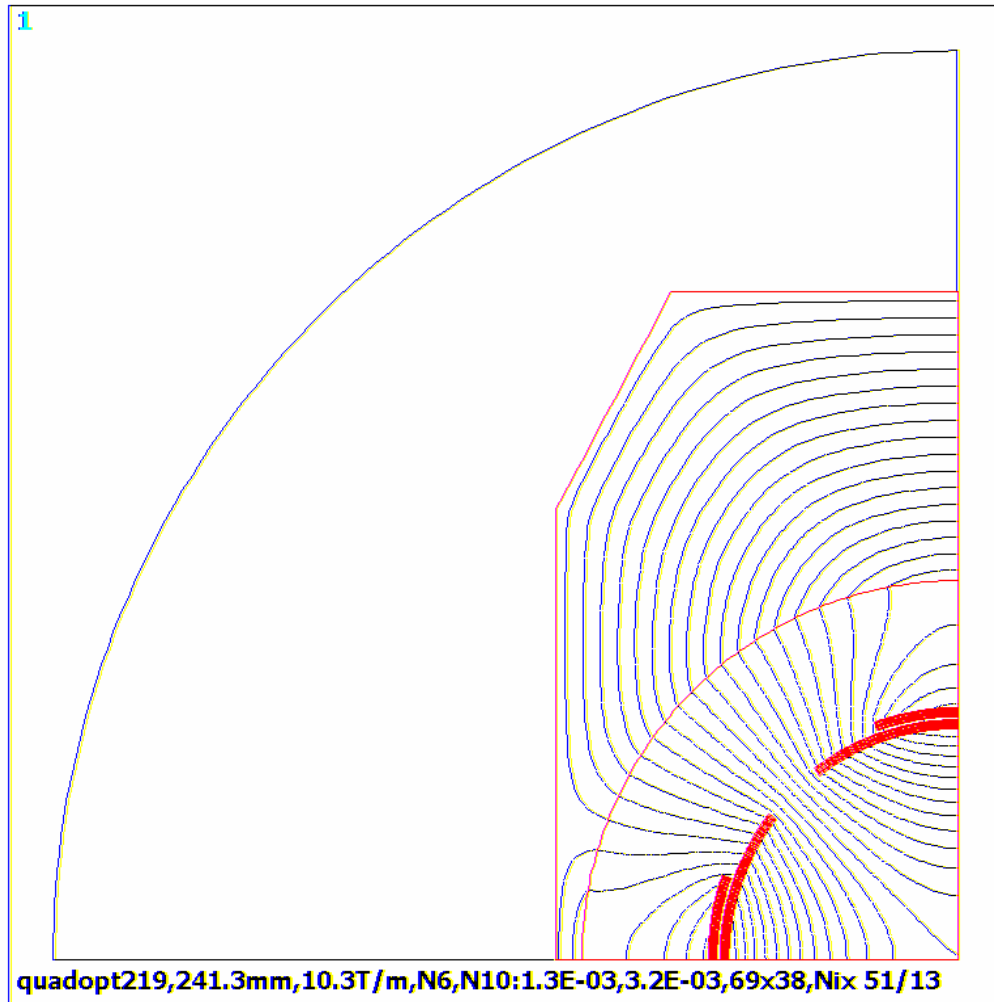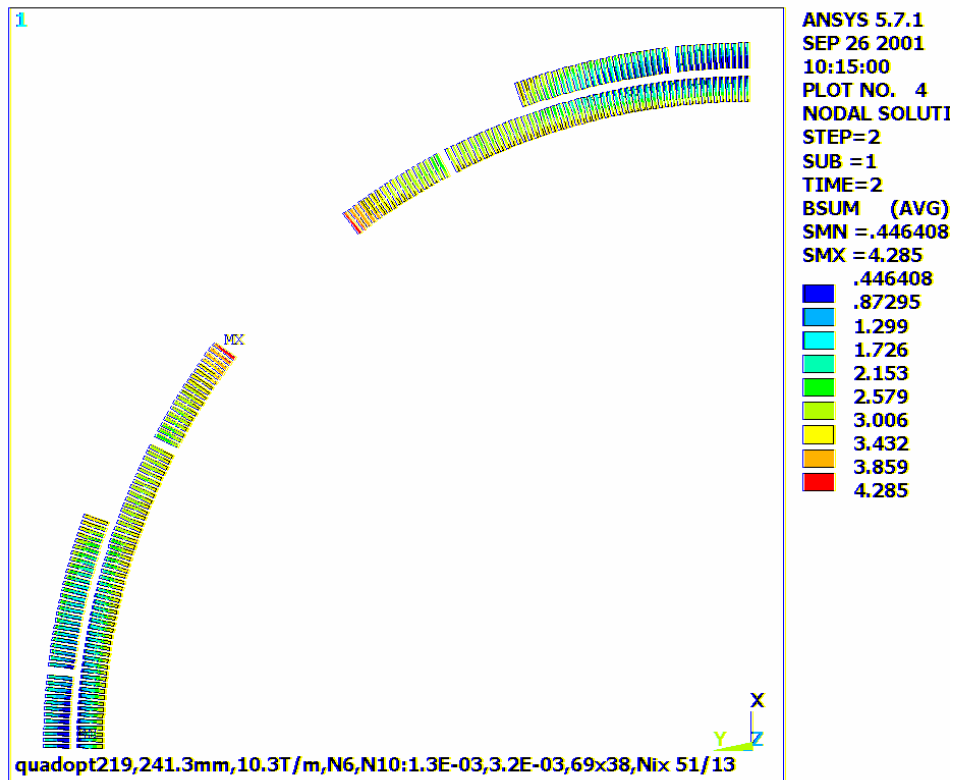

Fig. 6.1 Flux Lines

Fig. 6.2 Flux density in conductor cross-sections [T]

Chapter 6a Field Leakage Analysis

The field leakage from the Case II coil required considerably more effort to calculate than was initially expected. Field leakage calculations were made with 2D and 3D models, using both ANSYS[16] and Vector Fields. Technical assistance consultations not only led to changes in the plot data types and field recovery options[17], but led to a major bug fix in the Vector Fields software. The most definitive and final analysis of the leakage flux was done by Radovinsky[18].

SUMMARY

Myatt's 2D analyses using ANSYS[19] showed that with a tight fit between the upper, and the lower halves of the iron cases at the equatorial plane the fringe fields at the Case I beam line can be reduced to about 1 gauss. Additional 3D analyses of these phenomena were suggested using a 3D model, and another software package, i.e. Tosca by Vector Fields (VF). The first model generated for these analyses failed to work due to a bug in the software[20]. Vector Fields admitted that Tosca had a problem in case of

---

[16] AHF-MIT-LMyatt-0720-01, R.L. Myatt, " Fringe Fields in the Case II Beam, Revised Winding Radius," July 20, 2001
[17] HCX-MIT-JHSchultz-112701-01, Joel H. Schultz, A. R. Radovinsky, L.M. Myatt, "Interpretation of Field Calibration Exercises using Vector Fields and ANSYS," November 27, 2001
[18] AHF-MIT-ARadovinsky-011502-01, A.L. Radovinsky, "Case I Shielding from Case II Coil," January 15, 2002
[19] AHF-MIT-LMyatt-0720-01, R.L. Myatt, " Fringe Fields in the Case II Beam, Revised Winding Radius," July 20, 2001
[20] A.L. Radovinsky, " Progress with VF OPERA3D," October 31, 2001, AHF-MIT-ARadovinsky-103101-01

a large number of current stick elements. A fix was applied, and further studies at MIT were performed with an adequate version of Vector Fields Tosca.

This chapter presents results of a 3D analysis of fringe fields at the beam line of Case I due to the currents in the Case II quadrupole. The maximum field is about 0.45 gauss. It is well below the 10-gauss spec.

MODEL and ANALYSES

The 3D VF model of Cases I&II with a Case II coil set was modeled as shown in Fig. 1. The Case II coils were modeled by 11,760 STRAIGHT CONDUCTOR elements according to build 'sadb516rjc' provided by Myatt. The geometry of the iron cases is as described above in chapter 2.. The lateral gap between the iron Cases I&II at the narrowest place, end of Case II, is 1 cm. Case I extends 1 m towards the center point of the magnet system. The properties of the iron used for both Case I&II iron shields are as specified by the BH curve in Radovinsky's memorandum[21].
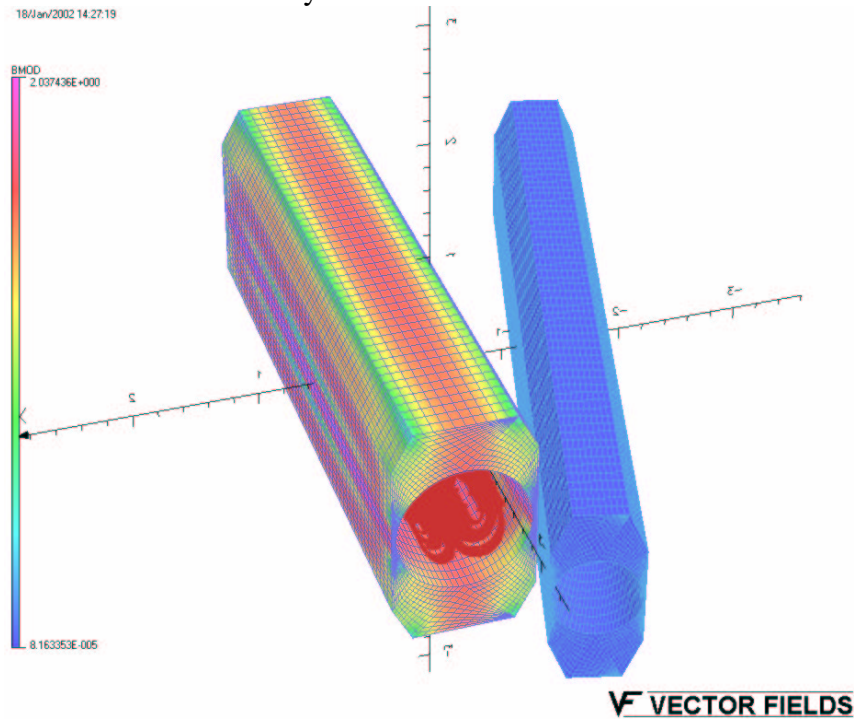

Fig. 1 Model of Cases I&II with Case II Quad Coils.

Orange lines in Figs 2 show the path along the Case I beam line radius, R=11.43 cm, closest to Case II.

---

[21] AHF-MIT-ARadovinsky-011502-01, A.L. Radovinsky, "Case I Shielding from Case II Coil," January 15, 2002

Fig. 2.a Case I Beam Line (orange).
Isometric View.
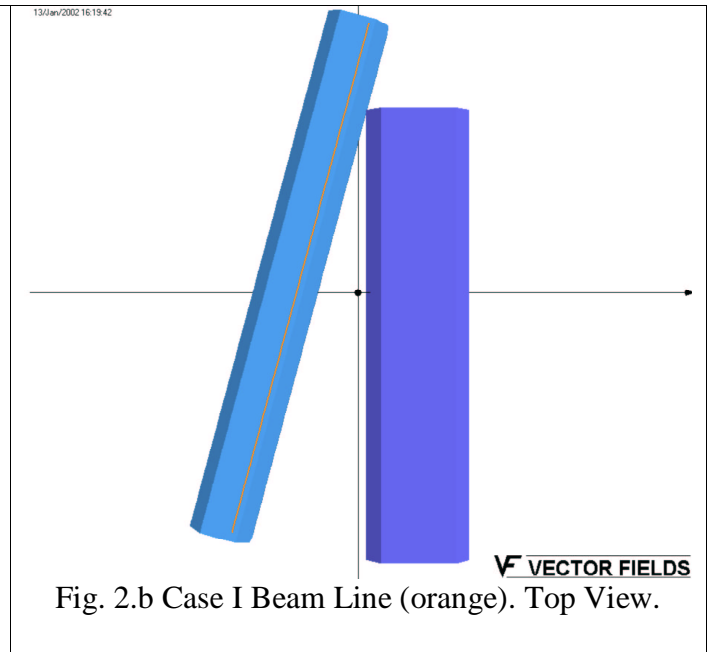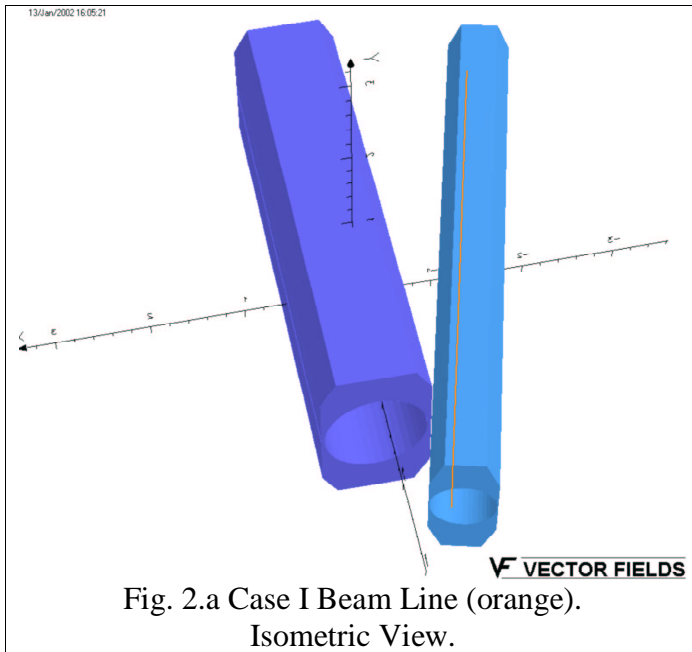
Fig. 2.b Case I Beam Line (orange). Top View.

Figure 3 shows the magnitude of the field calculated along this line. Left end of the interval is at the closest to the center end of Case I iron. The 0.45 gauss peak is in in line with the smallest gap between the cases, i.e. at the end of Case II iron.

This result is the same order of magnitude as the 1.1 gauss calculated for the same cross-sectional geometry of the cases, and the same properties of the iron used in the 2D ANSYS model by Myatt[22]. Note that besides 2D ANSYS vs. 3D VF there is one more difference between the two models. 2D model [1] models an infinite series of cases, Case I - Case II - Case I - Case II - Case I - Case II -…. The 3D VF model has Case II only on one side of Case I. This probably explains the difference between the results.

Figure 1 shows the model with a fine mesh. The run took 114 hours, so no further refinement of the mesh was considered. Instead, a verification run was performed with a mesh twice coarser in both directions of the baseplane. In the direction of extrusion the size of the mesh was left untouched. The peak value of the field along the path changed by 0.1 gauss.

---

[22] AHF-MIT-LMyatt-0720-01, R.L. Myatt, " Fringe Fields in the Case II Beam, Revised Winding Radius," July 20, 2001
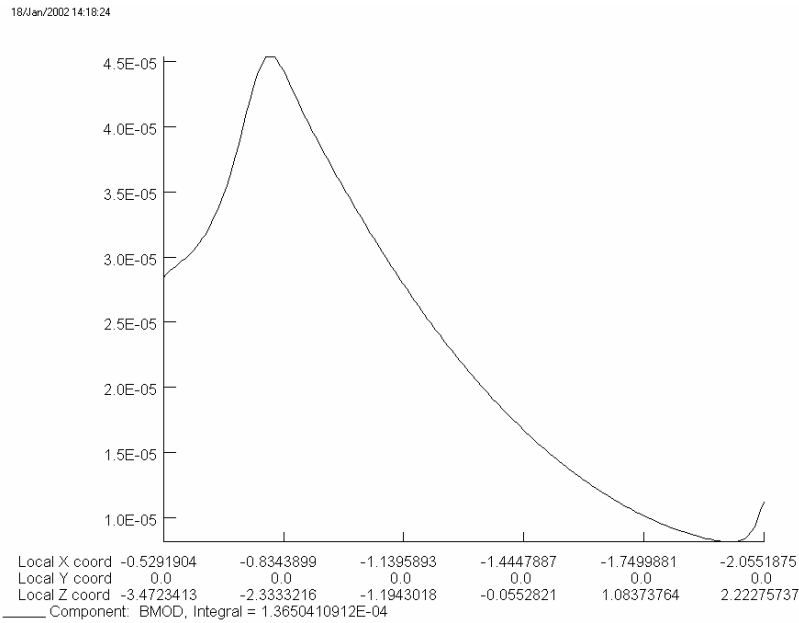
Fig. 3 BMOD along the Case I Beam Line

REFERENCES

1. Len Myatt, " Fringe Fields in the Case II Beam, Revised Winding Radius," July 20, 2001, AHF-MIT-LMyatt-0720-01
2. Joel H. Schultz, "AHF Quadrupoles Design Description Document, Rev.1," January 9, 2002, AHF-MIT JHSchultz-010902-01
3. A.L. Radovinsky, " Progress with VF OPERA3D," October 31, 2001, AHF-MIT-ARadovinsky-103101-01

Chapter 6b Analysis of Higher Harmonics

VI.a.1 Executive Summary

Optimization of the Case II quad with a spacer-free straight section was presented in an earlier project memo[23]. The analysis indicated that a 69-turn inner layer and a 37-turn outer layer (69x37) would produce the lowest 6th and 10th field harmonics for this simple, spacer free design concept. An end-turn study[24] was then performed and determined that three spacers per layer would do a reasonable job at trimming these peak harmonics in this region of the quad. However, when LANL issued a field error

---

[23] Myatt, "2D Turn-Count Optimization for Shielded Case II Quads," AHF-MIT-LMyatt-071601-01.
[24] Myatt, "End-Turn Optimization Study #1," AHF-MIT-LMyatt-082701-01.

requirements document[25], and the reference conceptual design was measured against these standards, it became clear that the design fell short[26], and improvements must be made.

In this 2D re-analysis of the Case II quad straight-section, a small change is proposed[27]: Could the field harmonics be reduced substantially by replacing a single turn in the straight section of each layer with a spacer of like-dimensions? If the answer is yes, then this approach could result in the smallest possible deviation from the present conceptual design, and thereby maintain its characteristic high efficiency (field gradient per Ampere) and simplicity.

Through a combination of various optimization algorithms[28] and computational brute-force, the 2D study has arrived at a single spacer per layer design which should meet the LANL field error design criteria *in the straight-section of the quad* ($Z_2 - Z_3$, [25]). Here, the 51st turn of the inner layer and the 13th turn of the outer layer become spacers. The turn count is nearly unchanged (68 turns plus one turn-equivalent spacer in the inner layer, 37 turns plus one turn-equivalent spacer in the outer layer), but the higher-order field harmonics are substantially smaller, compared to the original design.

The normalized 6th field harmonic (N6=A6/A2) has dropped from 1.7×10^{-4} to 0.13×10^{-4}, and the normalized 10th field harmonic (N10=A10/A2) has dropped from 9.0×10^{-4} to 0.32×10^{-4}. With due respect to the thoughtfulness and complexity of the LANL field error criteria, these values can be simplistically compared to limits of 5×10^{-4} (N6) and 2×10^{-4} (N10) for the straight-section of the quad. Proving this preliminary conclusion, and improving the end-turn field errors are TBD in 3D.

VI.a.2 Analysis

The analysis is based on the 2D electromagnetic ANSYS model of the quadrupole cross-section shown in Fig. 2.0-1. Symmetry about the vertical and horizontal axes allow the use of a quarter model. Individual turns serve as the current sources in this vector potential formulation. A representative section of the conductor array is shown in the Fig. 2.0-1 insert. The current source cross-section is based on a Rutherford cable with a 12.3 mm x 1.62 mm build. Spacing is defined by the 15.9 mm x 2.6 mm Cu channel, a 0.2 mm thick turn-wrap insulation, a 0.25 mm thick layer-to-layer insulation, and a 0.5 mm thick ground wrap. The inside surface of the ground-wrapped coil pack sits on a 0.318 m radius. This is consistent with the project's latest dimension, which puts the cryostat ID at 0.5842 m.

The quad is shielded by an iron yoke with an inside radius of 52.5 cm, a half-width of 56 cm, a half-height of 92.5 cm, and a 0.0 cm gap at the horizontal symmetry plane. The chamfer measures 16 cm x 30 cm. These are all consistent with earlier shield dimensions[29]. External air and infinite domain elements envelope the shielded quadrupole. The inset plot in Fig. 2.0-1 shows the conductors which carry current, and a void in the otherwise constant pitch array which represent the so-called turn-equivalent spacers.

[25] P. L. Walstrom, "Magnetic Field Quality Specifications for the AHF Magnetic-Lens Superconducting Quadrupoles," Aug. 23, 2001.

[26] Myatt, "Case II Field Errors the LANL-Way," AHF-MIT-LMyatt-090701-01

[27] AHF-MIT-LMyatt-092601-01, R.L. Myatt, "2D Spacer Optimization for Shielded Case II Quads," Sept 26, 2001

[28] ANSYS RELEASE 5.7 UP20001208, ANSYS, Inc., Canonsburg, PA.

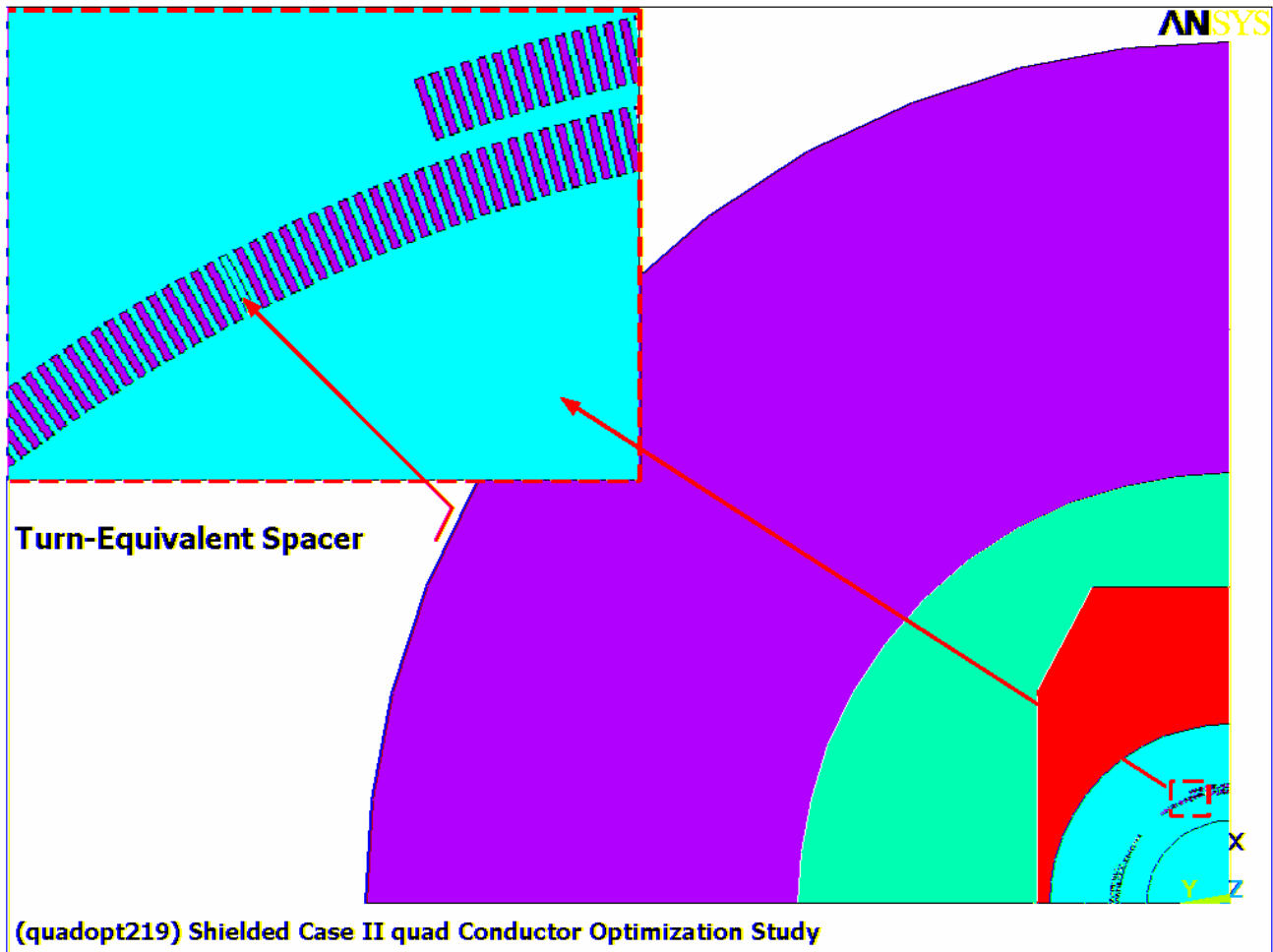[29] Myatt, "Shielding Case II Currents, Part II," AHF-MIT-LMyatt-062201-01

Fig. 2.0-1 2D, Quarter-Symmetric ANSYS model, Shielded Case II quad

The ANSYS design optimization algorithm is invoked as a way to minimize an objective function. In this case, the analyst chooses the objective function: (ABS(A6) + ABS(A10)). The design variable is the voided turn location in each layer of the coil pack. Current is eliminated from one conductor in each layer, thereby making it a spacer (as shown in Fig. 2.0-1). Harmonics are re-calculated, and a database of sensitivity functions are filled (by the program) with each iteration. Logic within the program optimizer searches over the entire design space in order to minimize this objective function.

A series of ANSYS optimization analyses point to an area in the design-space which contains the optimum design. However, finding it requires a more methodical approach. The analysis proceeds by brute-force, sweeping through all combinations of voided turn locations: 45-60 in the inner layer, 1-6 in the outer layer. This is manageable because the problem is formulated in 2D.

Upon review of the design-space sweep discussed above, the minimum error design was not found. But the results pointed the analysis in a more focused subspace: 50-52 in the inner layer, 10-14 in the outer layer. Notice that the ANSYS optimizer did not give accurate insight into the outer layer voided turn location. This revised range, indeed, leads to the optimum, single-spacer per layer design, as discussed in the Results section of this memo.

VII.a.3 Results

The most useful results of the 100+ analyses are captured in two plots. Figs. 3.0-1 and 3.0-2 are plots of the normalized 6th and 10th harmonic coefficients as a function of the location of the outer-layer voided turn, for a family of inner layer voided turn locations. The normalizing factor is the 2nd harmonic coefficient. Recall that the project field quality guideline is 2.0×10^{-4} for the 6th harmonic and 5.0×10^{-4} for the 10th harmonic. These limits must be compared to field errors integrated over various axial regions of the quad. However, if we assume that these harmonics are relatively constant in Z in the straight length region ($Z_2 - Z_3$, [25]) which they are, then a preliminary evaluation at this mid-quad location is a reasonable screening procedure.

Fig. 3.0-1 shows a number of important results associated with the normalized 6th harmonic:

- It is a minimum over a rather narrow range of outer-layer voided-turn locations (11-13).
- The 51st turn of the inner layer produces the lowest normalized harmonic.
- All of the design points are below the 5.0×10^{-4} design criteria.

Fig. 3.0-2 is a similar plot of the effects of the voided turn location on the normalized 10th harmonic coefficient. In this case, the minima occur over a slightly broader range of outer layer void locations (10-14). Also, all of the designs in this range meet the project's 5.0×10^{-4} design criteria for the 10th harmonic.

Studying the two figures together leads to the optimum design: inner-layer void at turn location 51, and outer-layer void at turn location 12. This combination produces the lowest harmonic coefficients, both of which are preliminarily well below the referenced design criteria.

The 2D optimization story is not yet complete, however. All of these analyses are performed with an idealized external shield (flux-normal boundary conditions on the inside surface of the constant radius yoke). This allows very fast run-times for the large number of designs which need to be considered. In order to confirm the selection of the optimum spacer locations, the saturable iron model (shown in Fig. 2.0-1) is exercised over a much reduced design-space (inner void at turn 51, outer voids at 11,12, 13 or 14). Results are listed in Table 3.0-1. Notice that all of these candidate designs pass the screening criteria (Normalized/Allowable<1). However, (51/12) and (51/13) are the best of the bunch. It is not clear which of these two designs is the very best. One has the most margin compared to the 6th harmonic requirement, and the other has the most margin compared to the 10th harmonic requirement.

Table 3.0-1 Harmonic coefficients and screening results for some candidate designs
(Saturable yoke results, slightly too little current leads to 10.22 T/m, not 10.3 T/m)

Inner/Outer Layer Voided Turns	N6x10000	6th Harmonic Screening (N6/5.0x10⁻⁴)	N10x10000	10th Harmonic Screening (N10/2.0x10⁻⁴)
51/11	1.33	0.27	0.57	0.29
51/12	0.61	0.12	0.14	0.07
51/13	0.17	0.03	0.32	0.16
51/14	1.00	0.20	0.80	0.40

Fig. 3.0-1 (A6/A2) as a function of voided turn location
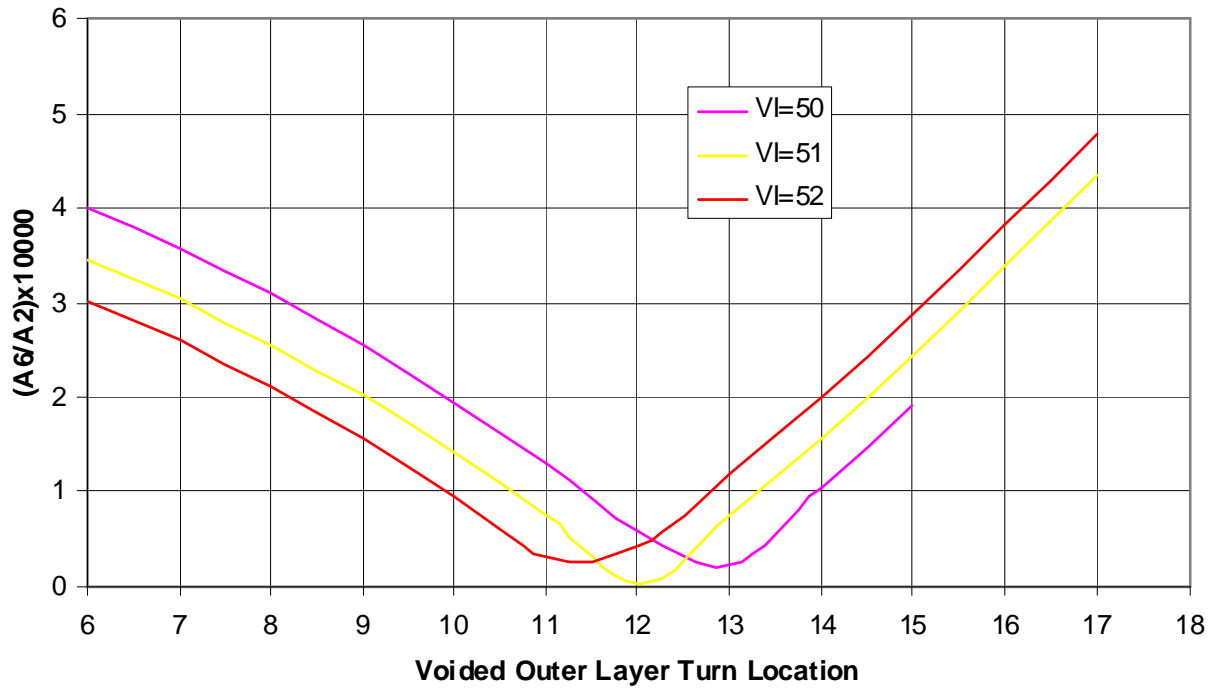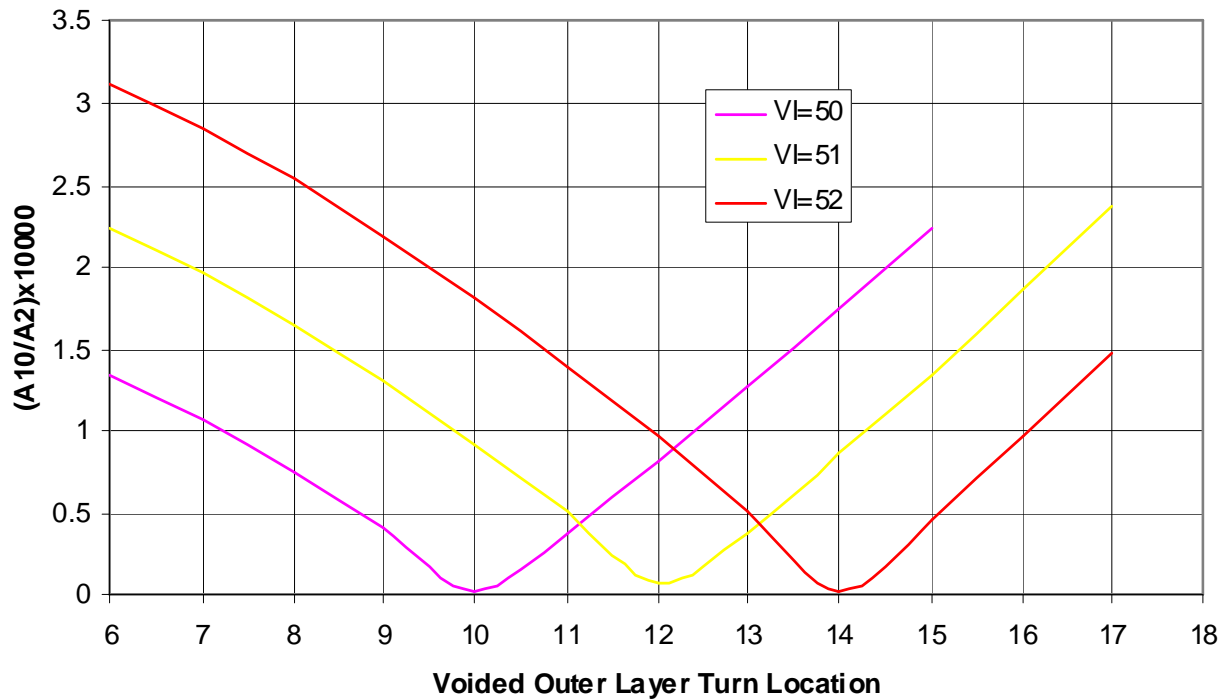

Fig. 3.0-2 (A10/A2) as a function of voided turn location

A few representative ANSYS plots are included to show the salient results of the optimized design. The optimum design is taken to be the one with the smallest 6th harmonic and combined 6th and 10th harmonic sum, which is (51/13). The project may favor the other candidate optimum design, which has more margin in the 10th harmonic contribution.

Chapter 7: Stress Analysis

VII.1 Executive Summary

A 2.5D electromagnetic-structural ANSYS[30] analysis of the FY01 Case II quadrupole was completed[31]. The model and analysis are nearly identical to those applied to the FY00 design[32]. Minor differences include the turn-count, winding radius, shell thickness and the external iron shield.

The analysis evaluates a simple, spacer-free winding pack, which has been optimized with 68 turns in the inner layer and 37 turns in the outer layer[33]. Dead turns are added to the outer layer to square-off the winding cross section and to maintain a consistent structural medium. Circumferential compression in the coil pack is obtained by winding the turns around a solid core, and applying a radial pre-compression before welding the outer stainless steel cylinder. The solid winding core can be made from SS or Ti, since both have negligible magnetic characteristics. A SS core has a thermal contraction rate (α) which is roughly comparable with the coil pack, while a Ti core shrinks substantially less than either during the 293-4K cool-down. The advantage of the Ti core is that it reduces the assembly preload. Some of the required circumferential compression is developed during cool-down by the differential α between the core and the external shell.

The analyses show that only the design which uses a Ti winding core leads to acceptable stresses. The required assembly preload is 7.3 MN/m (42 k-lb/in). Glass-epoxy insulation, Cu channel, and 3 cm thick external SS shell all meet their respective design criteria, indicating that this design concept is feasible. The design based on the SS winding core requires a 40% large assembly preload, and produces stresses which are borderline or above typical design values.

VII.2 Analysis

The structural elements of the ANSYS model are shown in Fig. 2.0-1. The neighboring free-space elements are unselected so that the focus can be on the structural aspects of the model. Field and structural boundary conditions of the one-eighth quadrupole model are discussed in a previous memorandum[34] and the interested reader is referred there for such details. The figure shows a full view of a winding pack cross-section and a close-up. All 106 turns (69+37) of the two-layer saddle coil are modeled explicitly. In addition there are 35 *Dead Turns* added to the inside of the outer layer. These turns do not carry current, but help maintain a consistent stiffness and thermal contraction throughout the coil pack cross-section, which would not occur with a G10, copper or steel filler.

---

[30] ANSYS RELEASE 5.7.1 UP20010418, ANSYS, Inc., Canonsburg, PA.

[31] AHF-MIT-LMyatt-091901-01, R. Leonard (Len) Myatt, "2.5D Stress Analysis of Shielded Case II Quadrupole," September 19, 2001

[32] Myatt & Camille, "2.5D Stress Analysis of Case II Quadrupole," AHF-MIT-LMyatt-061500-01.

[33] Myatt, "End-Turn Optimization Study #1," AHF-MIT-LMyatt-082701-01

[34] R. Leonard Myatt, "Stress Analyses of Four and Six-Layer Quadrupoles with US-DPC Conductor," PRad-MIT-LMyatt-082699-01.
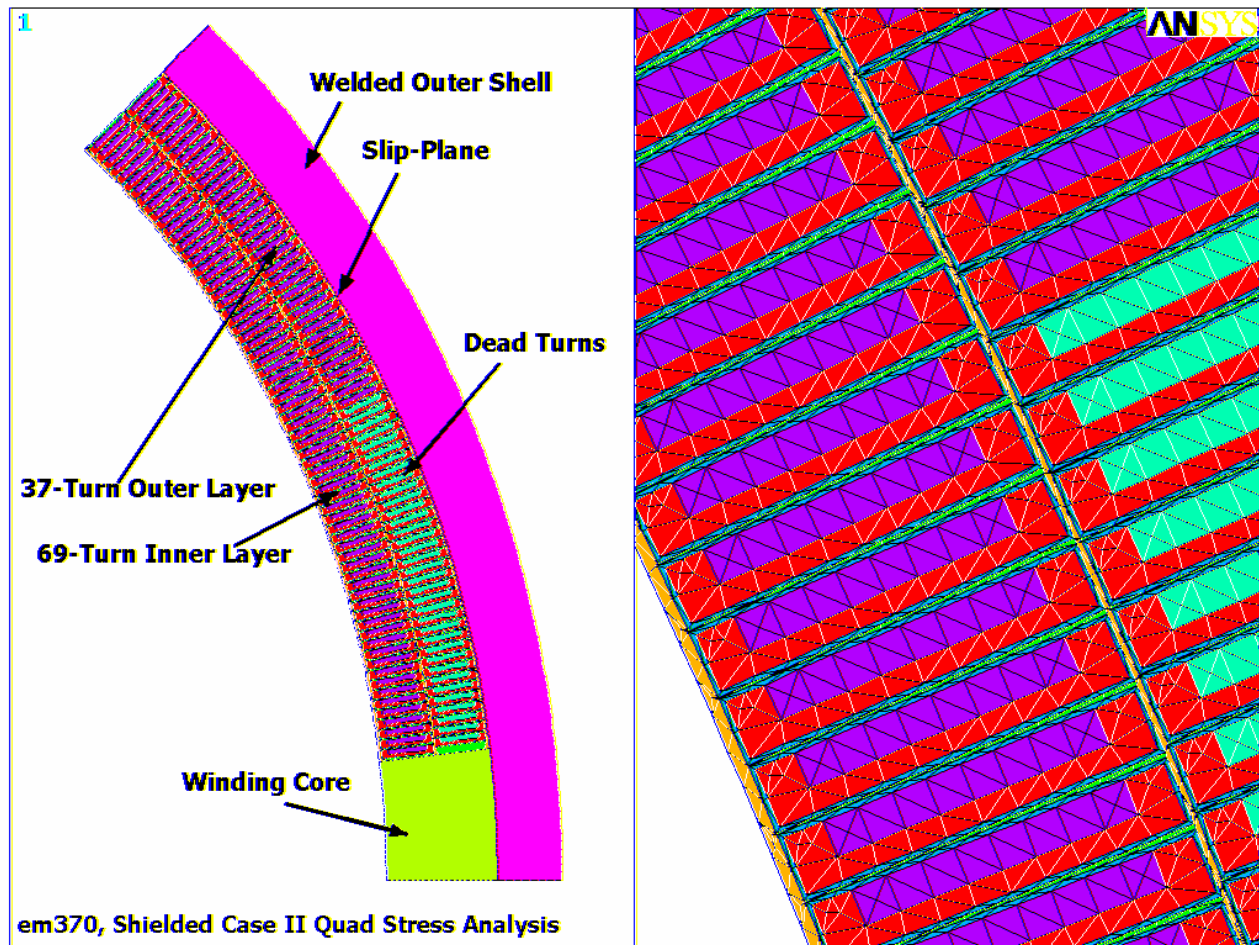
Fig. 2.0-1 Overview of 2D ANSYS model

The double-layer saddle coil is wound on a solid *Winding Core*. The core provides a continuous, circumferential load path through the winding pack, which is required to develop pre-compression. By selecting a core material with a low thermal contraction rate (such as Ti), some of the required winding pre-compression would be achieved during the cool-down from room temperature to 4K. This is a practical benefit since incorporating the preload during the magnet assembly will require some sort of hydraulic press system, and smaller means less expensive. Stainless steel is also a candidate material. But, it would not develop any winding pack preload during cool-down.

The conductor is assembled with the dimensions given in Table 2.0-1. Insulated turns of the inner layer are set on a 0.28755+0.0306 m radius, and align with rays originating at (0,0). The "+0.0306" component of the inner layer radius is an incremental change from the FY00 design, and came from the additional space required for shielding. Wedge-shaped spacers extend across the height of each layer to separate adjacent turns. These spacers could be eliminated if the conductor is key-stoned to the appropriate dimension. The turn-wrap, ground wrap and layer insulations are 0.2 mm, 0.5 mm and 0.25 mm thick epoxy-glass, respectively. The coil is contained by a TBD thick stainless steel shell. A frictionless slip-plane exists between the coil pack and the external shell. However, it is unlikely that any relative motion will occur here if the coil pack is pre-compressed to the appropriate level.

Table 2.0-1 SSC Cable-in-Cu-Channel Dimensions

Geometric Parameter	Dimension
SSC Cable radial build (height)	12.3 mm
SSC Cable tangential build (width)	1.62 mm
Cu Channel radial build (height)	15.9 mm
Cu Channel tangential build (width)	0.26 mm
Turn wrap insulation thickness	0.20 mm
Layer insulation thickness	0.25 mm
Ground Wrap insulation thickness	0.50 mm

Table 2.0-2 lists the material properties which are used in the model. Values for stainless steel and glass-filled epoxy insulation (G-10CR) come from the ITER material property data base. The cable is soldered into the channel void, and assumed to be well-packed with mechanical properties comparable to Cu.

Table 2.0-2 Material properties of magnets at 4K

Material	E_r [GPa]	θz [GPa]	r /K	θz /K	
Stainless Steel	207	207	10.4	10.4	0.28
Superconducting Cable	137	137	11.4	11.4	0.34
Copper	137	137	11.4	11.4	0.34
Glass-Filled Epoxy Insulation	22	32	25	8	0.21
Titanium	123	123	5.2	5.2	0.31

The model is loaded in five steps; one electromagnetic analysis, and four structural analyses.

1. 7.2 kA operating current to get fields and body forces
2. External shell pressure to simulate the preload applied just before welding the outer shell
3. Zero-out external pressure to simulate the assembled quad at room temperature
4. Cool-down to 4K
5. Apply EM body forces and an axial load (equal to the stored magnetic energy/length).

The analysis process is somewhat iterative since the amount of preload required to keep the turns in circumferential compression is not known a priori. A preload is included in the model by defining a reference temperature for the outer shell which is above the reference temperature of all other materials. The reference temperature is the temperature at which thermal contraction effects are zero. If the entire model is at 293K and the shell has a reference temperature of say 400K (while all other parts of the model have a reference temperature of 293K), then there will be a thermal strain in the shell which is reacted by the winding pack and core.

EM loads are then applied (Load Step 5), and the circumferential stresses in the turn wrap insulation are checked for though-thickness tension. Regions of circumferential tension are indications of areas which will experience relative motion while the coil is energized (and de-energized). This motion will not only impart energy into the coil (which could lead to a quench), but it could also lead to a deterioration of the

insulation. The shell's reference temperature is adjusted until all (or most) of the turn insulation remains in compression for the design-basis operating condition.

Having established the optimum preload (shell reference temperature), the analysis returns to Load Case 2: external shell assembly pressure. This is also an iterative process. The objective of the load case is to determine the magnitude of the external pressure which is required during the final closure weld of the shell, to achieve the desired winding pack preload. The external pressure is varied until the circumferential shell stress is driven to zero.

Of course, the magnitude of the require mechanical preload is a function of the winding core material and circumferential extent. Clearly, the use of a low contraction rate core (such as Ti) will require less mechanical preload than a higher contraction rate core (such as SS). Analysis of both Ti and SS core options are presented.

VII.3 Results

The results of the SS and Ti winding core analyses are presented in Sections 3.1 and 3.2, respectively. Numerical results of the Cu channel and external shell, and aspects of the insulation system, are listed in Tables 3.1-1 and 3.1-2. A few representative stress contour plots are also included and discussed.

The tabulated results indicate that the SS winding core design requires a very large preload, which results in borderline or excessively high stresses in the Cu, SS shell and insulation system. When the Ti winding core is used, the room temperature preload is substantially smaller, and the resulting stresses seem acceptable.

The external pressure applied during assembly is required to ensure turn-to-turn compression when the coil is energized. This pressure is 40% large for the SS winding core design (19 MPa) compared to the Ti winding core design (13.5 MPa). In this particular configuration, the mechanical preload produces a substantial portion of the maximum system stress levels. The attached stress plots help illustrate this result.

Table 3.1-1 Stress Summary (SS Winding Core)

Structural Component	Stress Category	Unit	Stress Value	Allowable Stress
Cu Channel	Mem + Bend	MPa	**300**	300
	Peak	MPa	323-229-323…	$>10^4$ cycles
Turn-Wrap Insulation	Normal	MPa	**250**	200
	In-Plane	MPa	112	150
	Shear/Normal	% OK	89	100
External Shell	Membrane	MPa	**170**	176
	Mem + Bend	MPa	200	310
	Peak	MPa	133-228-133…	$>10^4$ cycles

Table 3.2-1 Stress Summary (Ti Winding Core)

Structural Component	Stress Category	Unit	Stress Value	Allowable Stress
Cu Channel	Mem + Bend	MPa	200	300
	Peak	MPa	184-282-184…	$>10^4$ cycles
Turn-Wrap Insulation	Normal	MPa	182	200
	In-Plane	MPa	105	150
	Shear/Normal	% OK	86	100
External Shell	Membrane	MPa	120	176
	Mem + Bend	MPa	131	310
	Peak	MPa	115-199-115…	$>10^4$ cycles

3.1 SS Winding Core Results

Fig. 3.1-1 is a plot of the stress intensity in the Cu channel during the preloading operation. The rams press against the outer shell to develop the necessary preload, and produce a room-temperature stress intensity of ~300 MPa in the inner lugs of the inner layer Cu channel. We shall ignore for now the highly localized peak of 370 MPa which occurs at the 45° symmetry plan. Assuming a Cu cold work of 50%, the tensile yield stress at 293K is about 300 MPa. Local stresses must be kept below this yield stress value. Clearly, the level of stress in this design is right at (and possibly above) the material's allowable value.
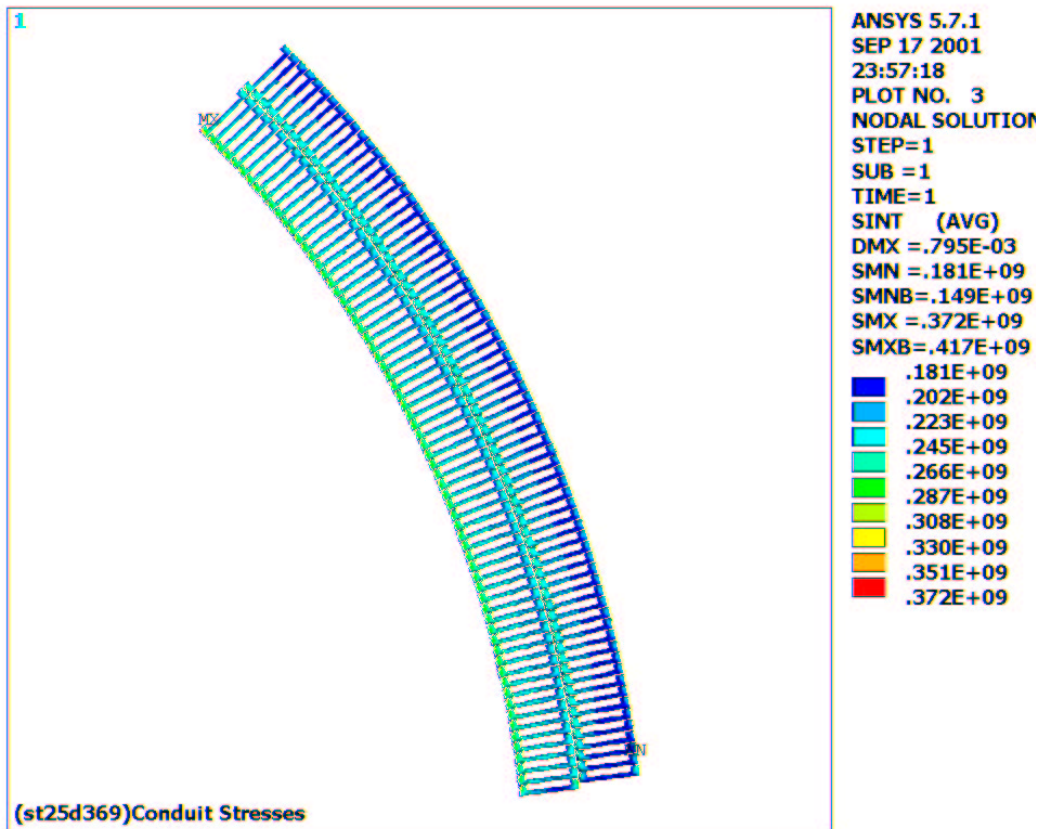
Fig. 3.1-1 Stress Intensity [Pa] in Cu channel from assembly preload only

Fig. 3.1-2 is a plot of the stress intensity in the Cu channel when the magnet is cooled to 4K and fully energized (producing 10.3 T/m). The peak stress intensity in the Cu channel is 323 MPa. This is also a highly localized stress. But, now it occurs at 4K, and the material's yield and ultimate strengths (400 and 490 MPa, respectively) are substantially higher than at room temperature.

The local average channel stress is about 220 MPa. Let's assume a Cu cold work of 50%. Typical design rules require that the local stress remain below $1.5S_m$, where S_m is the lesser of (2/3x400=267 MPa) or (1/2x490=245 MPa). Therefore, the allowable local stress is 367 MPa. Clearly, the level of stress in the Cu is well within these allowable stress limits, especially since the dominant stress is compressive, and far less likely to cause a break than a tensile stress.
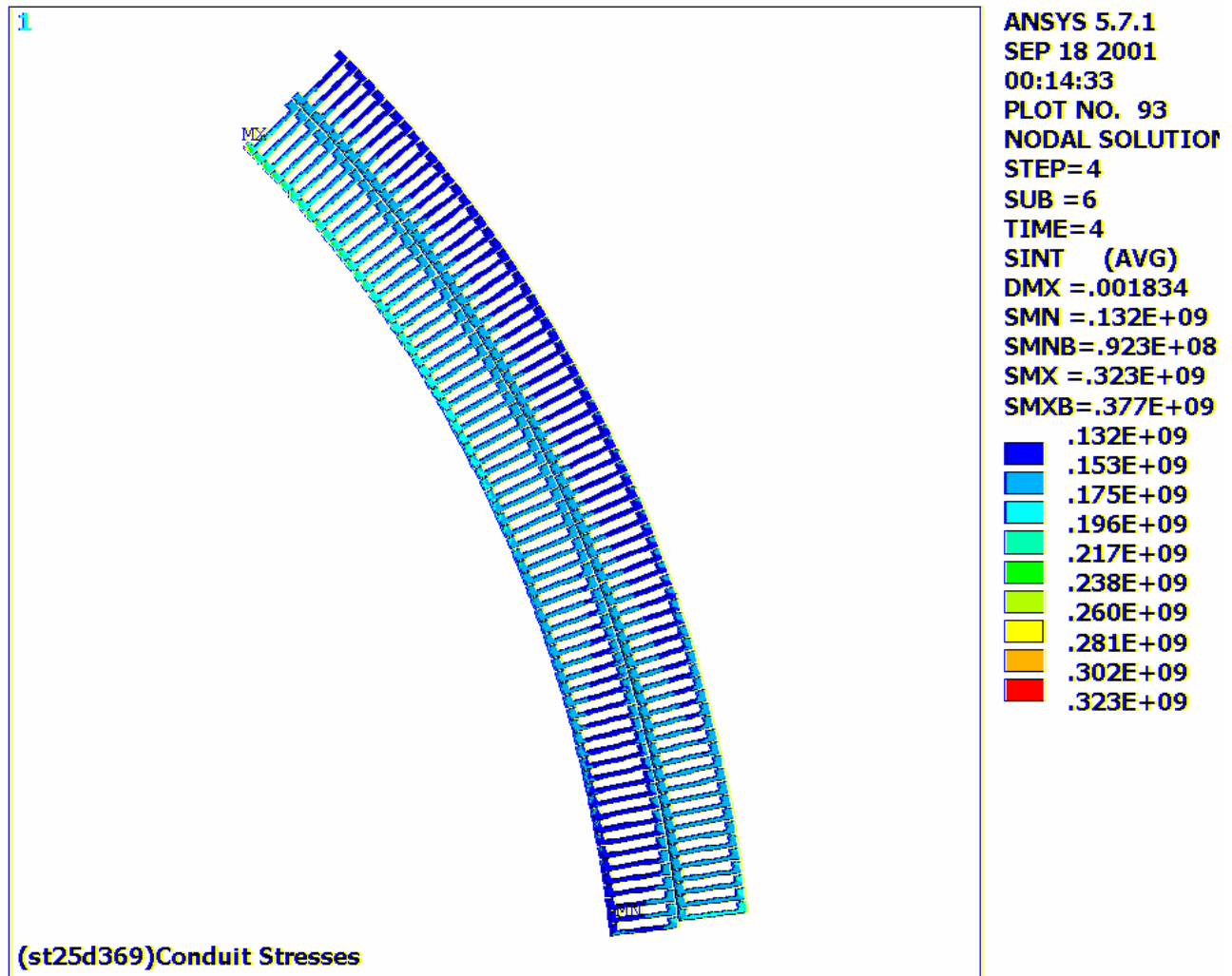
Fig. 3.1-2 Stress Intensity [Pa] in Cu channel from EM, differential thermal contractions and assembly preload load.

Fig. 3.1-3 is a plot of the normal (through-thickness) stresses in the turn wrap insulation. The numbers are comparable to the stresses in the Cu channel, since the circumferential load passes through both of these structural elements: about 250 MPa compression. Stresses at other operating conditions are less. The room temperature ultimate compressive strength for an E-glass filled epoxy such as G10 is about 400 MPa. Divide by two to get a room temperature design stress of 200 MPa. This turn insulation is above the room-temperature material limit.
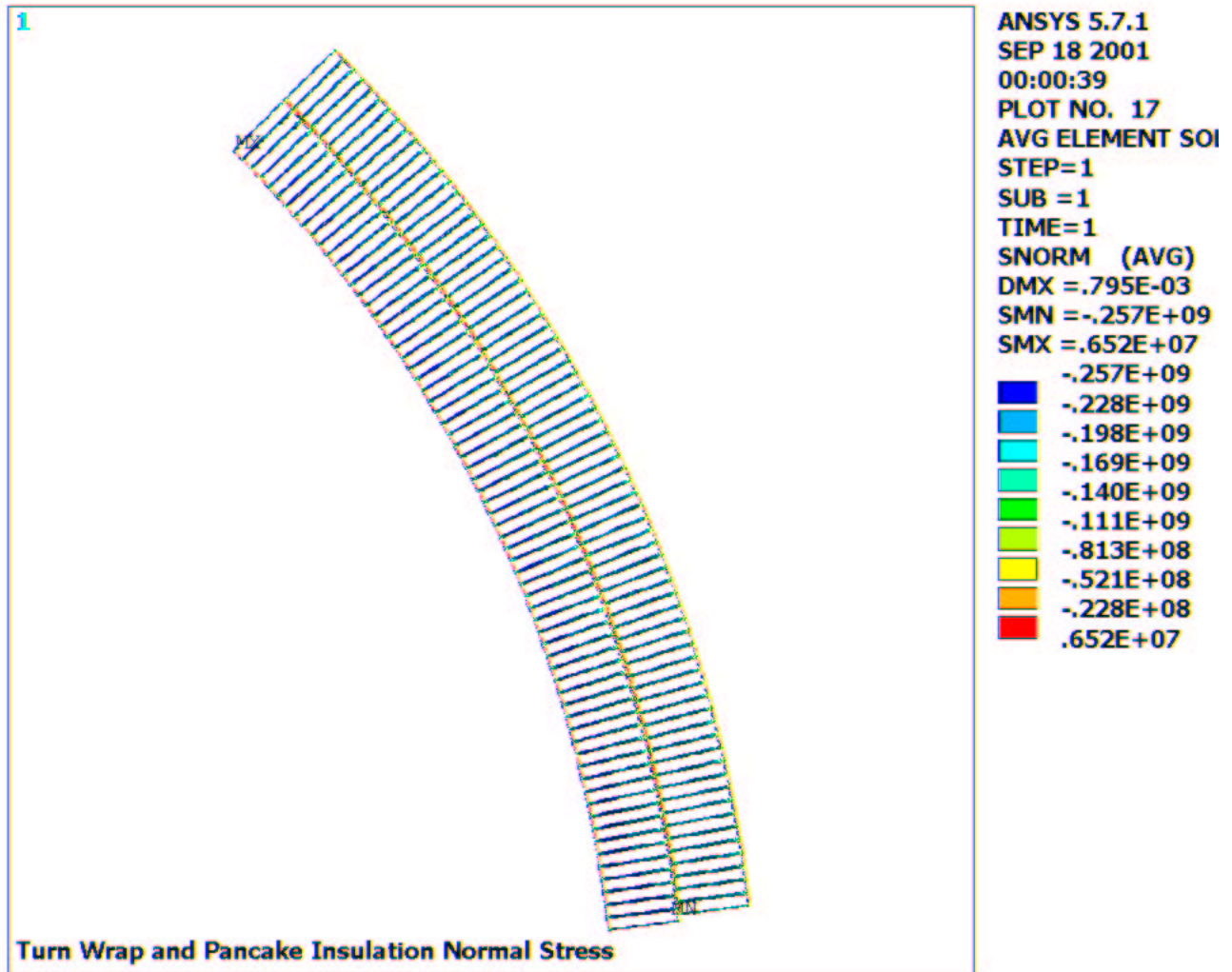
Fig. 3.1-3 Normal stress [Pa] in turn-wrap insulation from assembly preload

Fig. 3.1-4 is a plot of the in-plane stresses in the turn wrap insulation during the 4K, energized coil load case. In-plane insulation stresses are lower than this at all other load conditions. The material has a lower ultimate strength compared to the through thickness compressive stress limit reported above. The room temperature, in-plane ultimate strength is about 300 MPa. A factor of two yields a conservative design value of 150 MPa. The plot shows that the maximum stress is 112 MPa. This is a peak value, while the contour plot indicates that 60 MPa is more representative of the stress field. Conservatively comparing a 4K stress to a RT allowable indicates that the in-plane insulation stresses are well within the design criteria.
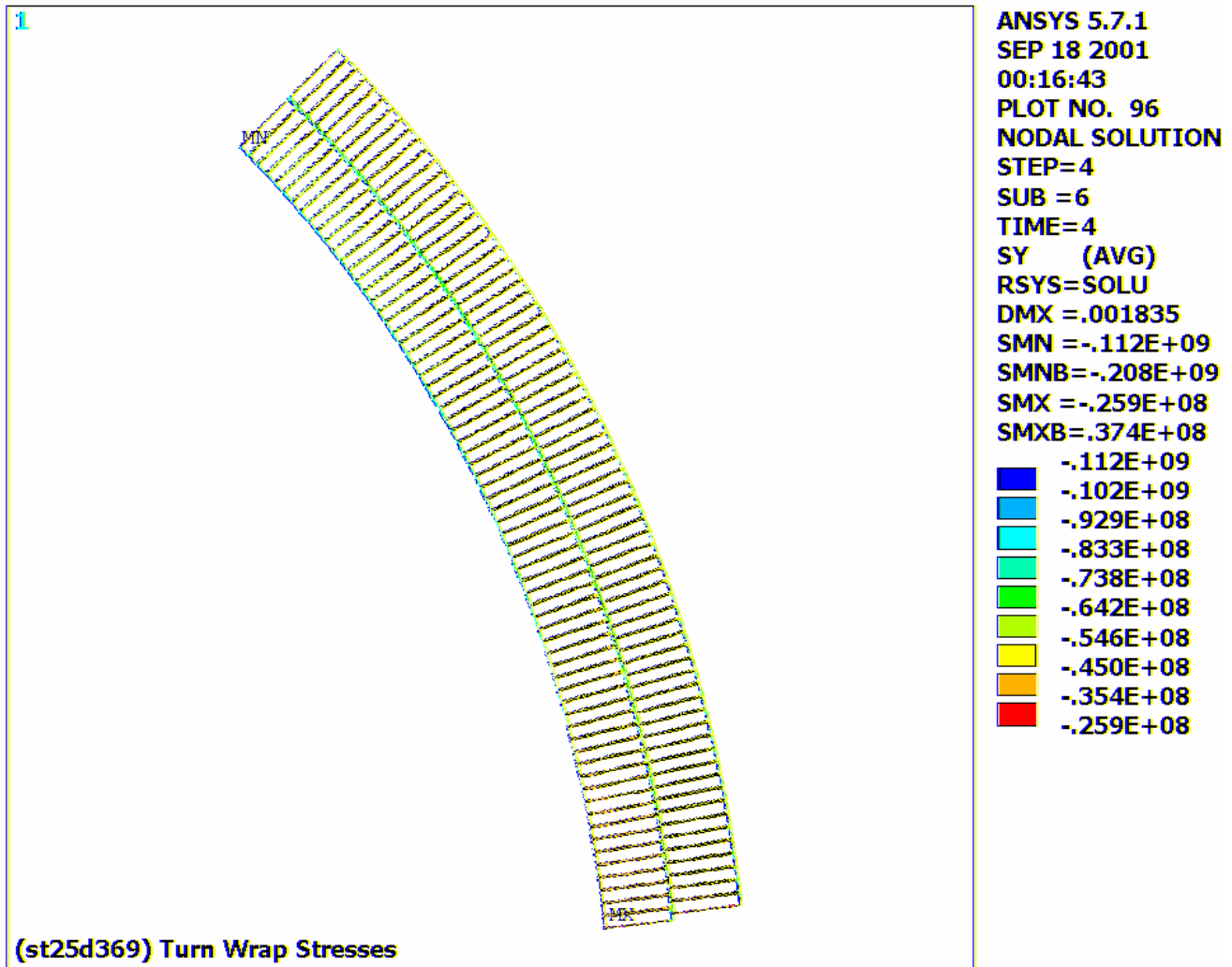
Fig. 3.1-4 In-plane stress [Pa] in turn-wrap insulation from EM, differential thermal contractions and assembly preload load

Fig. 3.1-5 is a plot of the hoop stress in the 3.0 cm thick external shell during the 293K, post-closure weld load case. Not only are these stresses larger than the 4K, energized coil load case, the allowable stress is also considerably lower at room temperature than it is at 4K. Away from welds, the average stress should be no more than 2/3 of the yield stress (310 MPa), or 207 MPa. Near a weld, with an efficiency factor of say 0.85, the average stress allowable becomes 176 MPa. Here, the average stress is about 170 MPa. The maximum stress can be as high as the yield stress, or about 310 MPa. Here, the maximum stress ~200 MPa. So, both criteria are met. Clearly, the average stress criteria would not be met with a thinner external shell.
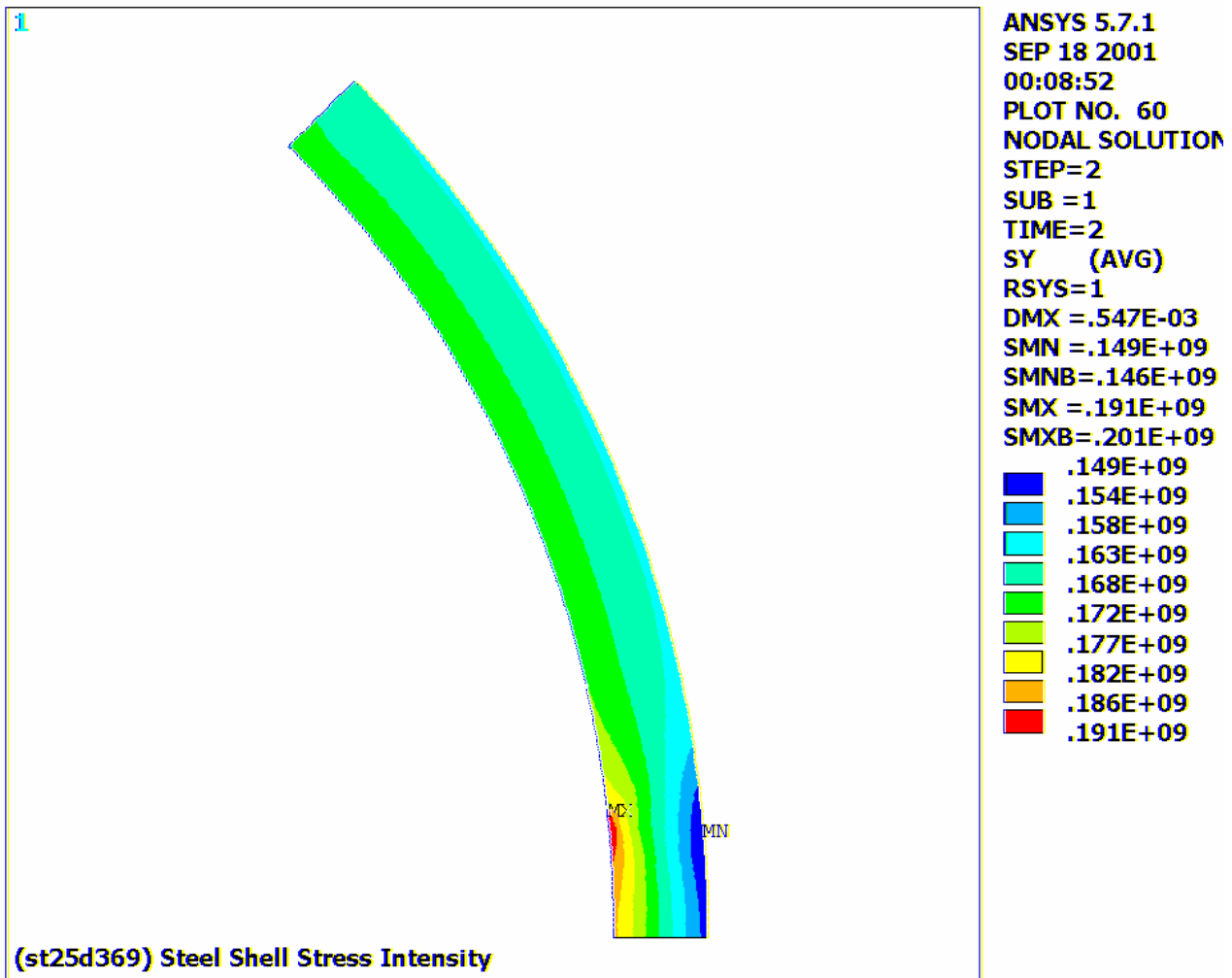
Fig. 3.1-5 Stress intensity [Pa] in SS shell from assembly preload

The saddle winding looks like a curved beam in axial compression, which leads to bending stresses (tension on one side, compression on the other) when the coil is energized. The objective of the external shell is to provide a circumferential preload which ensures compression throughout the winding pack when the coil is energized. This will minimize relative motion within the winding pack, and between the winding pack and the shell. The benefit is improved training characteristics and a more structurally stable insulation system. Sometimes it is easier to evaluate the condition of the insulation system by looking at the elements which fail the criteria (as opposed to looking at the elements which pass the

criteria). Fig. 3.1-6 is a plot of the insulation elements which fail the shear/compression criteria. The title indicates that 11% of the insulation fails the criteria.

If we follow the acceptance criteria adopted by the TPX fusion magnet program of the mid-90s[35], the results shown here can be considered acceptable (even though some of the insulation fails the criteria) since no "failures" in the insulation span between adjacent conductors, and there are no continuous in-plane delaminations greater than the dimension of the conductor unit cell.
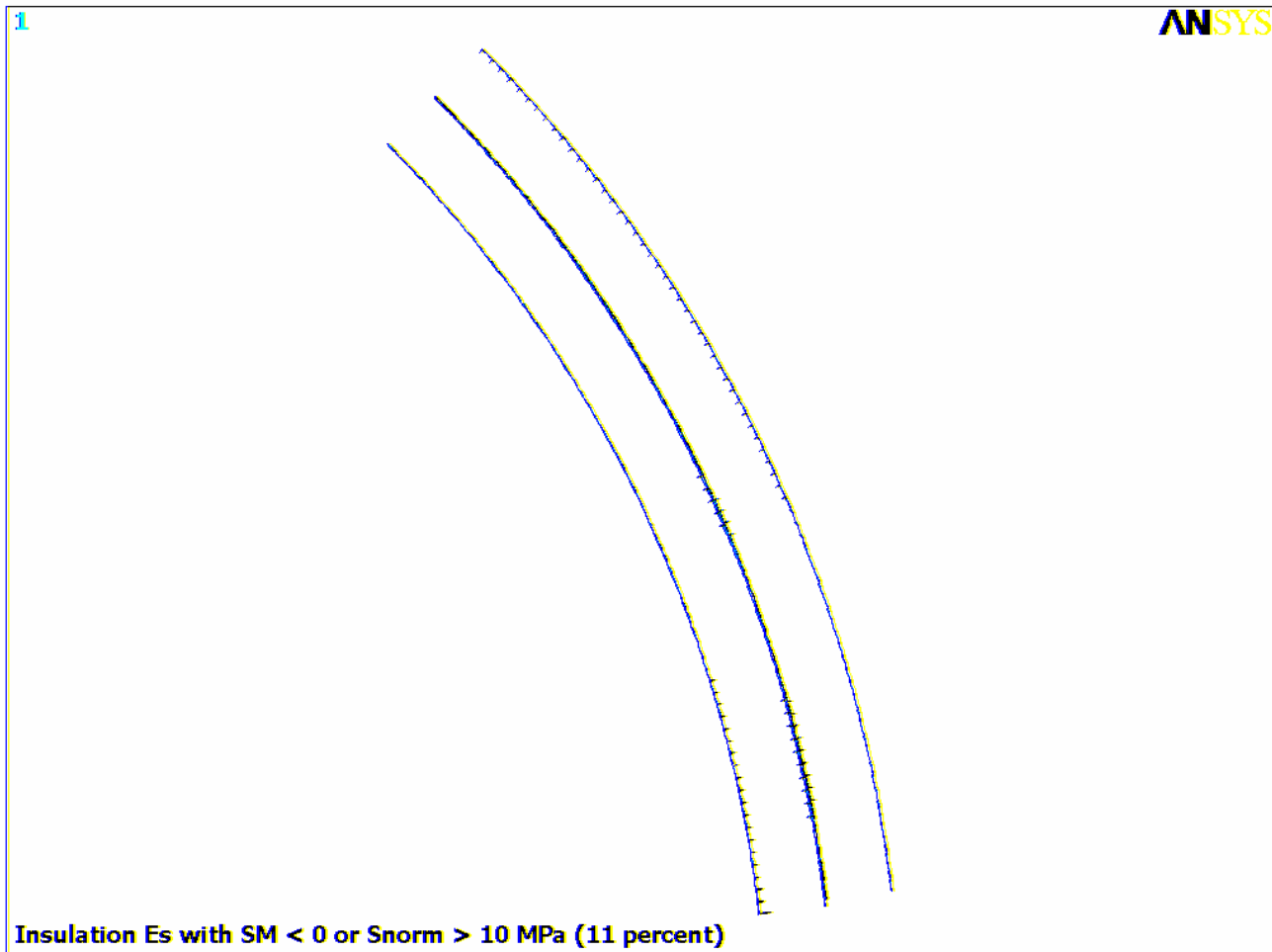
Fig. 3.1-6 Turn insulation elements which fail the shear/compression stress criteria

---

[35] P. Sanger, "TPX Magnet Insulation Large Scale Verification Test Program," TPX Magnet System Poloidal Field Magnet Preliminary Design and Manufacturing R&D, Contractor Preliminary Design Review, Volume 5 – Manufacturing R&D, Westinghouse, Northrop Grumman, Everson Electric, August 1995.

3.2 Ti Winding Core Results

Fig. 3.2-1 is a plot of the stress intensity in the Cu channel during the preloading operation. The rams press against the outer shell to develop the necessary preload, and produce a room-temperature stress intensity of ~200 MPa in the inner lugs of the inner layer Cu channel. Assuming a Cu cold work of 50%, the tensile yield stress at 293K is about 300 MPa. Local stresses must be kept below this yield stress value. Clearly, the level of stress in this design (including the 260 MPa peak stress) is well below the material's allowable value.
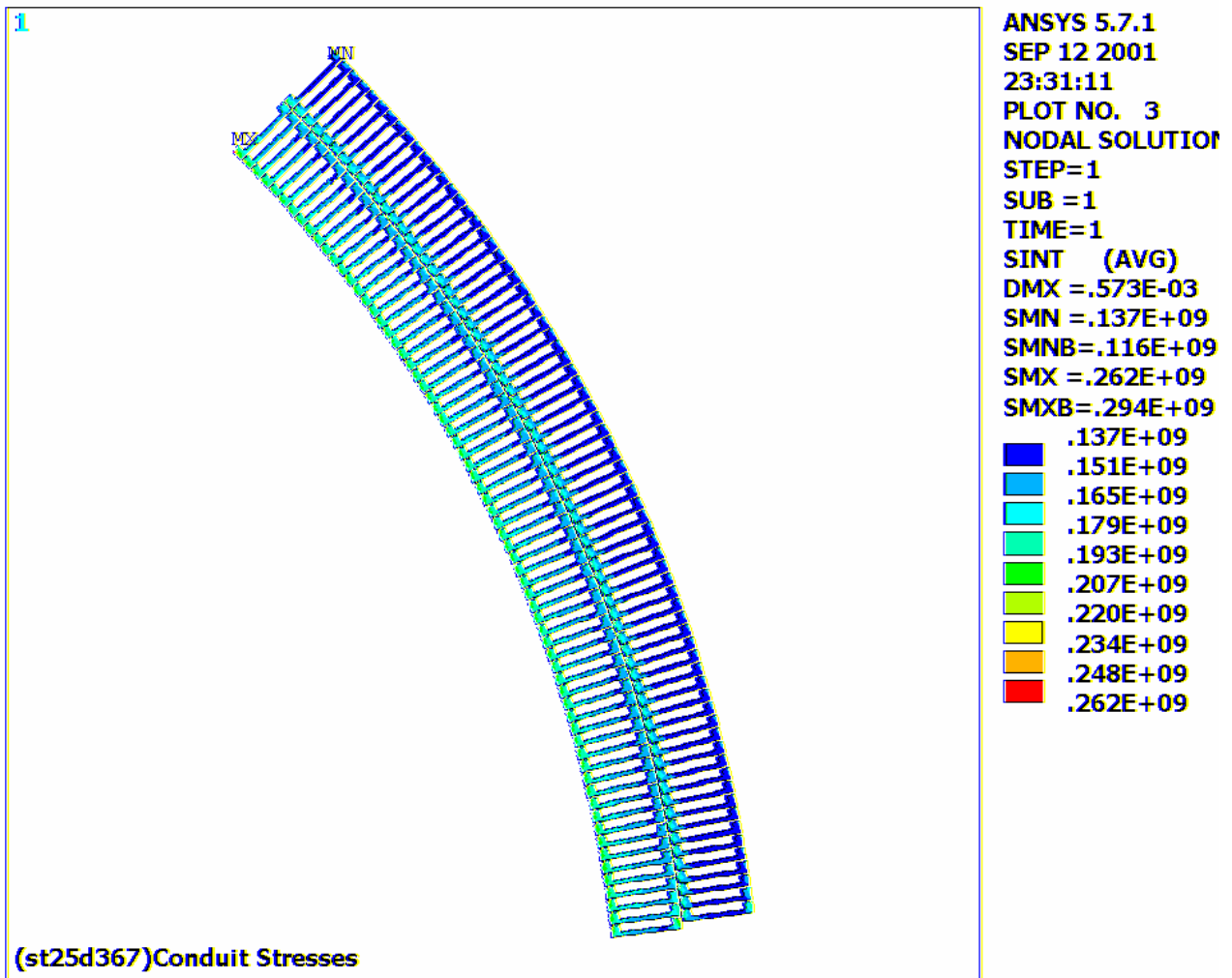
Fig. 3.2-1 Stress Intensity [Pa] in Cu channel from assembly preload only

Fig. 3.2-2 is a plot of the stress intensity in the Cu channel when the magnet is cooled to 4K and fully energized (producing 10.3 T/m). The peak stress intensity in the Cu channel is 280 MPa. This is also a highly localized stress. But, now it occurs at 4K, and the material's yield and ultimate strengths (400 and 490 MPa, respectively) are substantially higher than at room temperature.

The local average channel stress is about 200 MPa. Let's assume a Cu cold work of 50%. Typical design rules require that the local stress remain below $1.5S_m$, where S_m is the lesser of (2/3x400=267 MPa) or (1/2x490=245 MPa). Therefore, the allowable local stress is 367 MPa. Clearly, the level of stress in the Cu is well within these allowable stress limits, especially since the dominant stress is compressive, and far less likely to cause a break than a tensile stress.
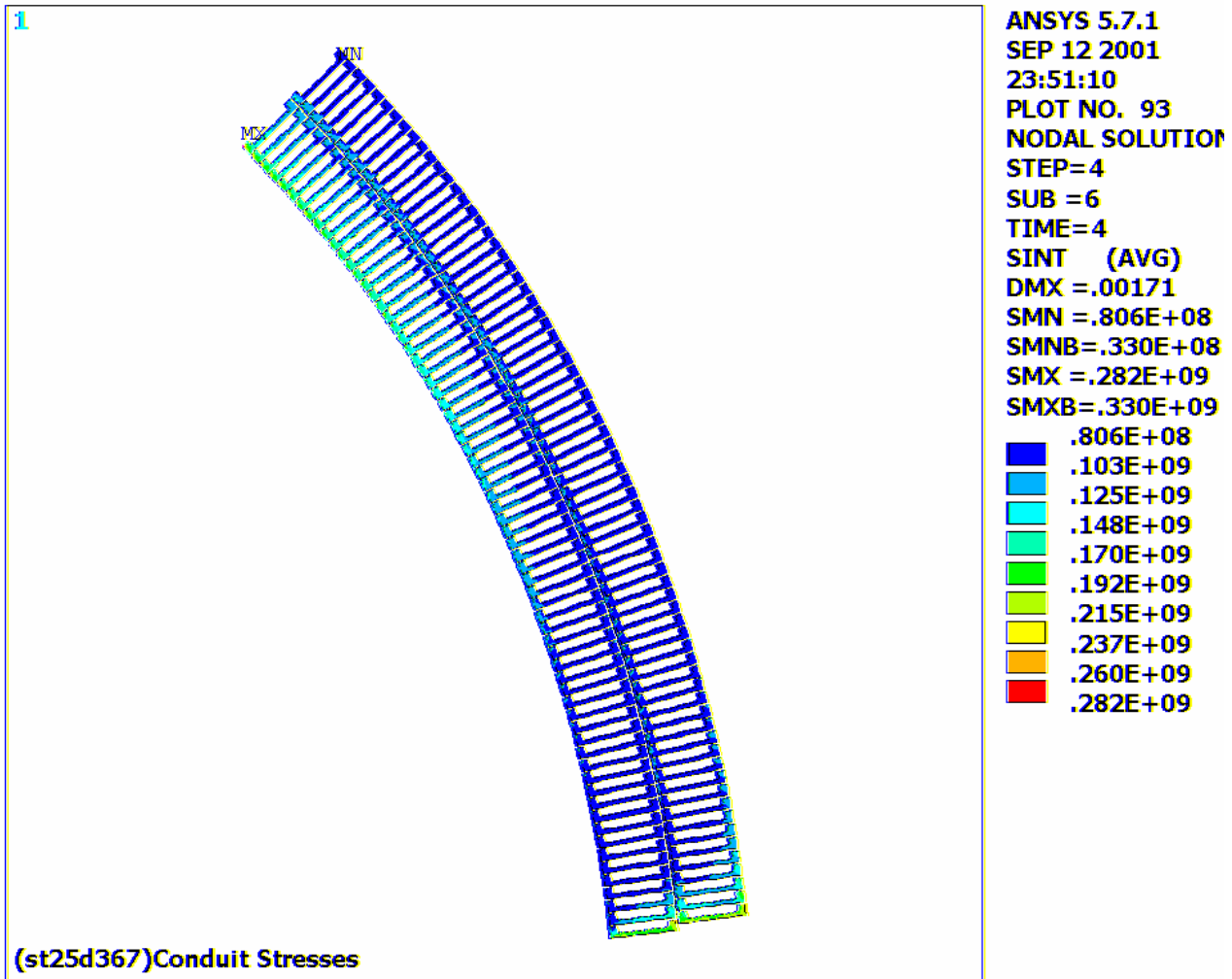
Fig. 3.2-2 Stress Intensity [Pa] in Cu channel from EM,
differential thermal contractions and assembly preload load

Fig. 3.2-3 is a plot of the normal stresses in the turn wrap insulation. The numbers are comparable to the stresses in the Cu channel, since the circumferential load passes through both of these structural elements: about 180 MPa compression. Stresses at other operating conditions are less. The room temperature ultimate compressive strength for an E-glass filled epoxy such as G10 is about 400 MPa. Divide by two to get a room temperature design stress of 200 MPa. This turn insulation is within the room-temperature material limit.
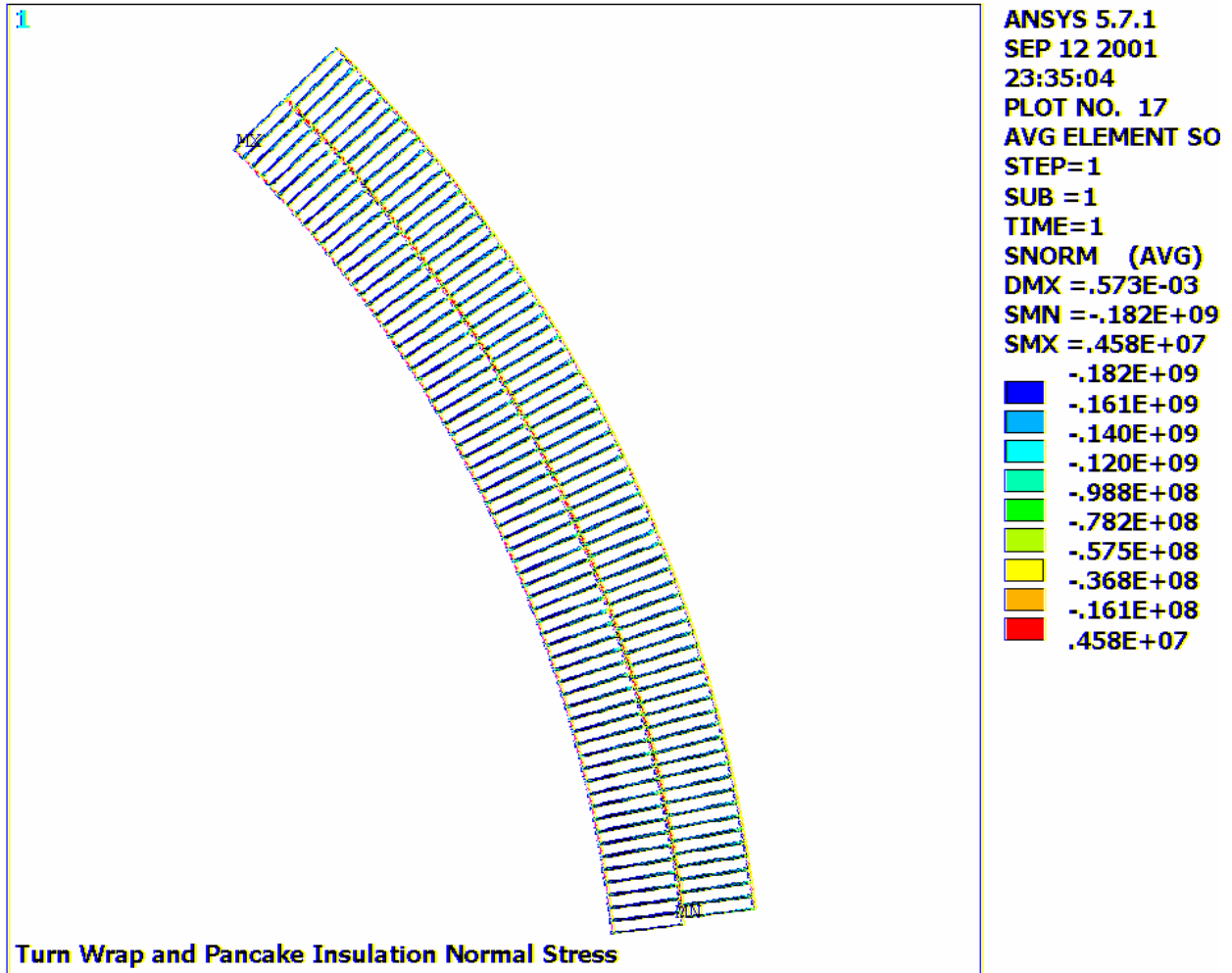
Fig. 3.2-3 Normal stress [Pa] in turn-wrap insulation from assembly preload

Fig. 3.2-4 is a plot of the in-plane stresses in the turn wrap insulation during the 4K, energized coil load case. In-plane insulation stresses are lower than this at all other load conditions. The material has a lower ultimate strength compared to the through thickness compressive stress limit reported above. The room temperature, in-plane ultimate strength is about 300 MPa. A factor of two yields a conservative design value of 150 MPa. The plot shows that the maximum stress is 105 MPa. This is a peak value, while the contour plot indicates that 50 MPa is more representative of the stress field. Conservatively comparing a 4K stress to a RT allowable indicates that the in-plane insulation stresses are well within the design criteria.
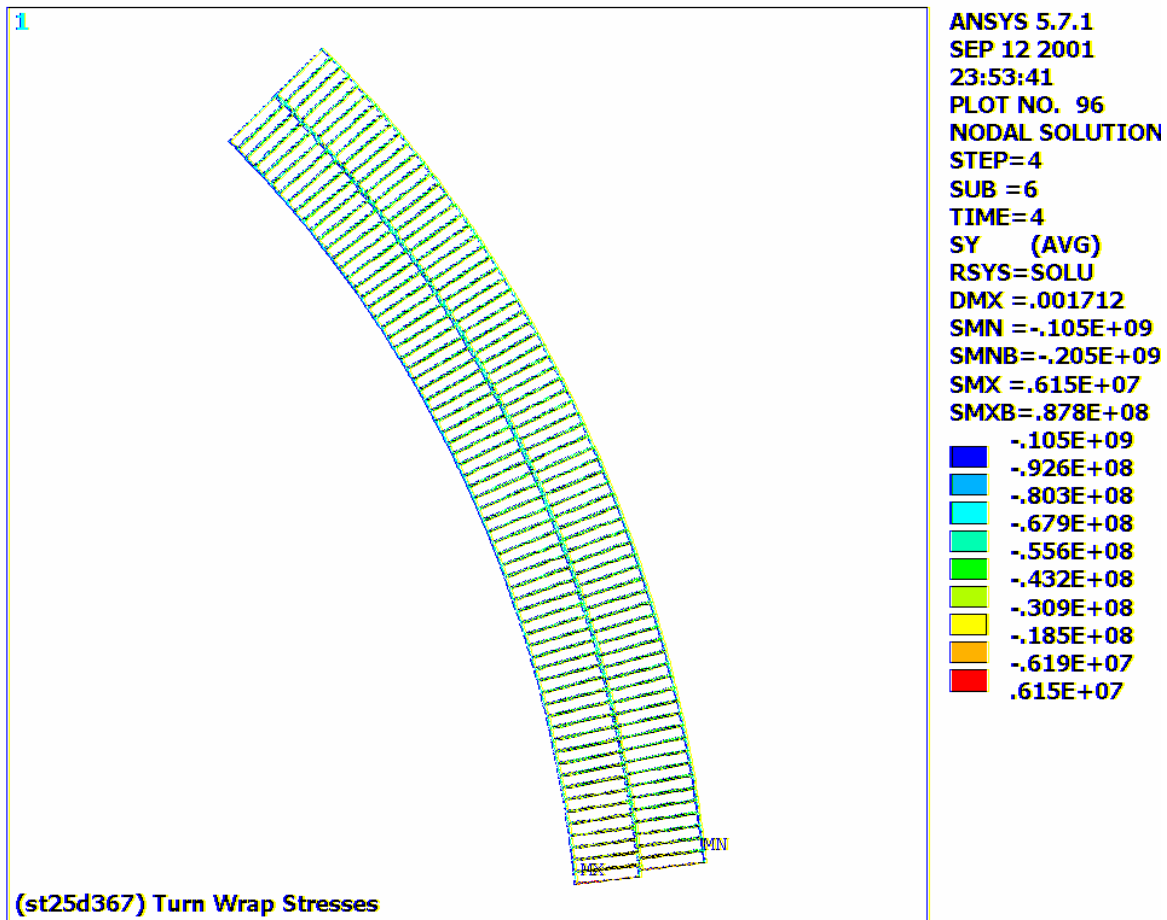
Fig. 3.2-4 In-plane stress [Pa] in turn-wrap insulation from EM, differential thermal contractions and assembly preload load

Fig. 3.2-5 is a plot of the hoop stress in the 3.0 cm thick external shell during the 293K, post-closure weld load case. Although these stresses are not as large as the 4K, energized coil load case (200 MPa max stress), the allowable stress is considerably lower at room temperature than it is at 4K. Away from welds, the average stress should be no more than 2/3 of the yield stress (310 MPa), or 207 MPa. Near a weld, with an efficiency factor of say 0.85, the average stress allowable becomes 176 MPa. Here, the average stress is about 120 MPa. The maximum stress can be as high as the yield stress, or about 310 MPa. Here, the maximum stress ~130 MPa. So, both criteria are met. This shell thickness is slightly conservative, and provides some margin to the design.
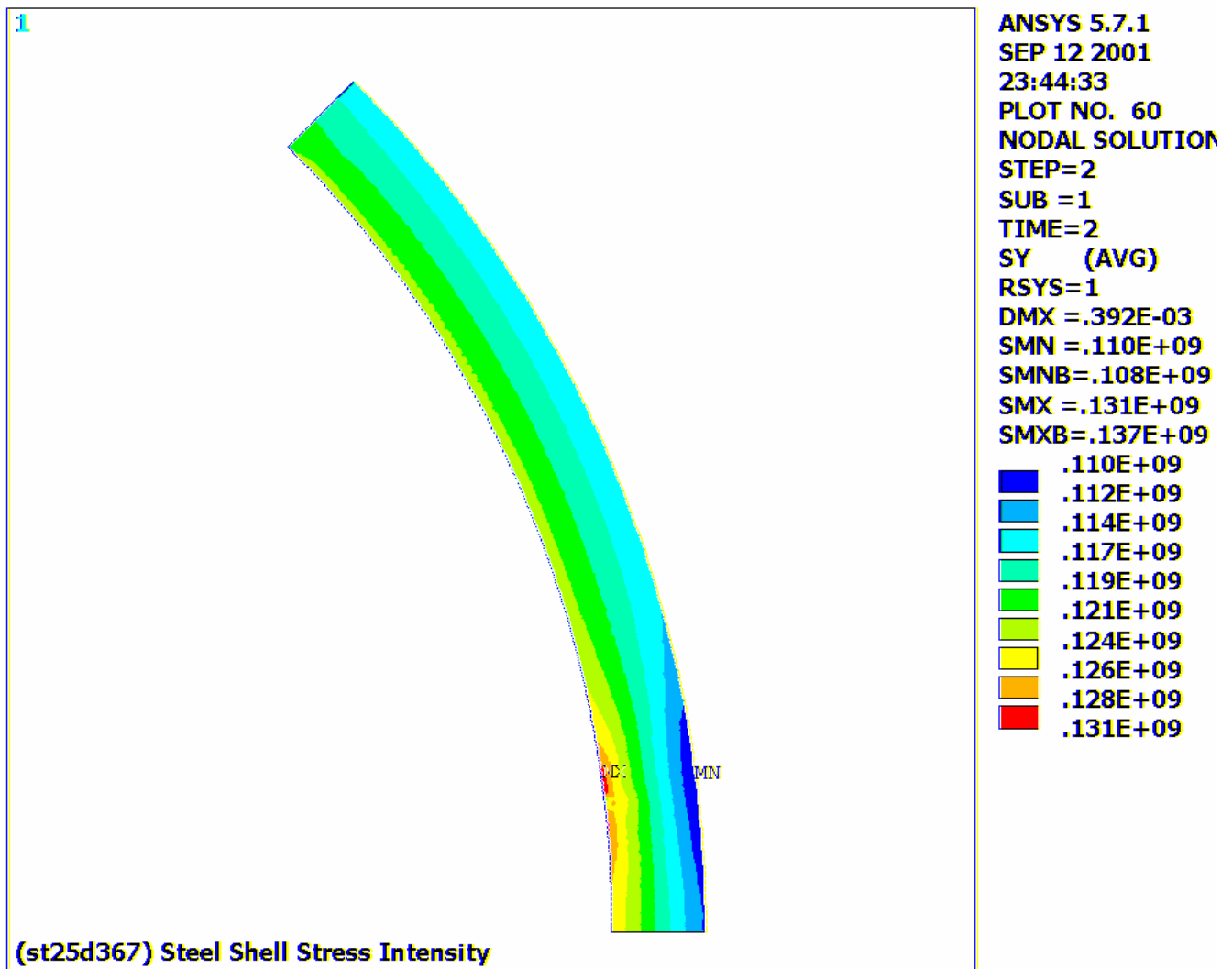
Fig. 3.2-5 Stress intensity [Pa] in SS shell from assembly preload

Fig. 3.2-6 is a plot of insulation elements that fail the shear/compression criteria. The title indicates that 14% of the insulation fails the criteria. The result is very similar to that reported for the SS winding core design, with one exception. Here, the inner turns of each layer are bonded to the low-α Ti winding core. The substantially dissimilar αs of glass-filled epoxy insulation and Ti produce a mechanical constraint that results in some turn-to-turn tension as illustrated in greatly exaggerated displacement plot of Fig. 3.2-6. This tension leads to a "failure" of the criteria (inner layer, near the Ti winding core). A design (and modeling) improvement would allow relative motion between these two parts during cool-down.
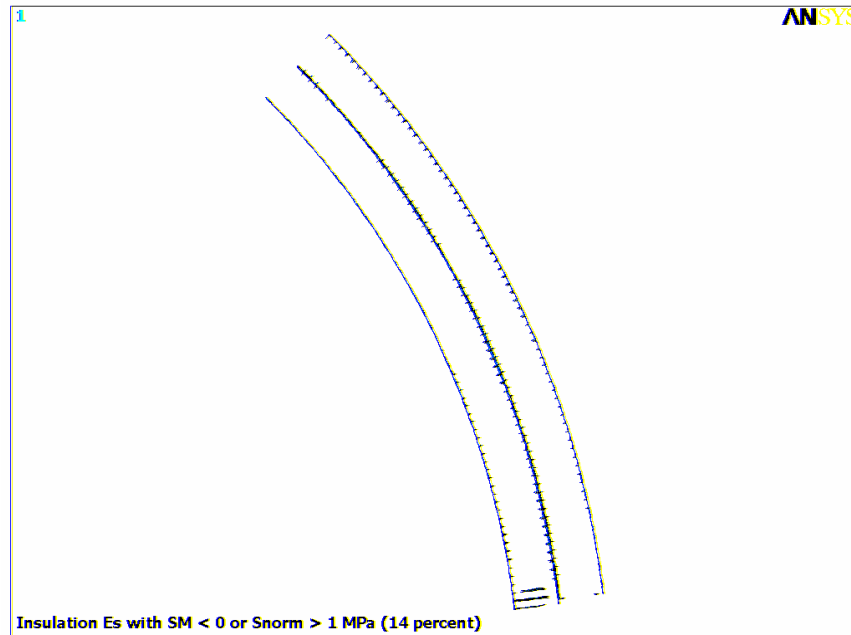
Fig. 3.2-6 Turn insulation elements which fail the shear/compression stress criteria
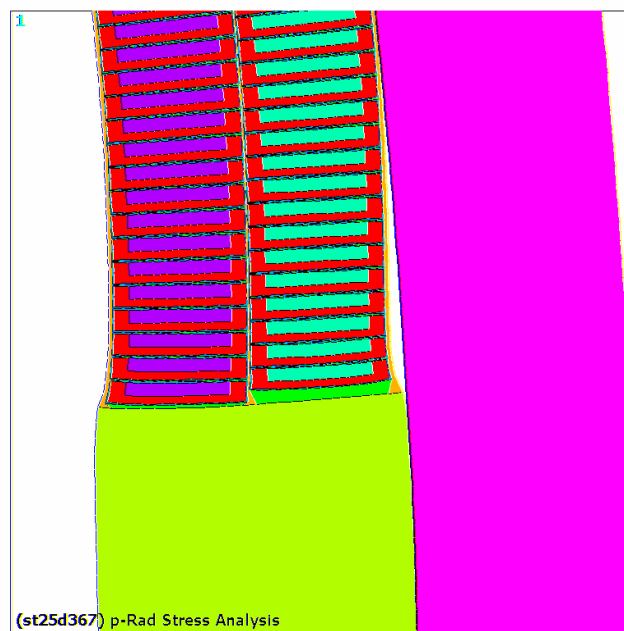
Fig. 3.2-7 Exaggerated Deformed shape
(winding pack stuck to winding core, cooled to 4K and energized)

3.3 Fatigue Evaluation

The copper channel and SS shell peak stress history are listed in Tables 3.1-1 and 3.2-1. A fatigue failure is driven by the stress range, and not simply the peak stress value. The analysis evaluates stresses at each of the four significant points in the operating cycle of the magnet: (293K, assembly preload), (293K, 0 EM), (4K, 0 EM), and (4, full EM). Results indicate that the maximum stress range is conservatively taken to be 100 MPa in the Cu and the stainless steel shell.

Fig. 3.3-1 shows the fatigue properties of annealed Oxygen-free Cu at various temperatures. A design point can be constructed by dividing the 4K stress at 10^4 cycles by two. A failure at this many cycles would require a stress range of 150 MPa. This is well above the 100 MPa stress range seen here. An alternating stress of 100 MPa in the stainless shell is even less critical, as indicated by the fatigue curve shown in Fig. 3.3-2. Therefore, it appears as if the cyclic operation of the magnet will not produce a crack in the Cu channel section or the SS external shell structure.
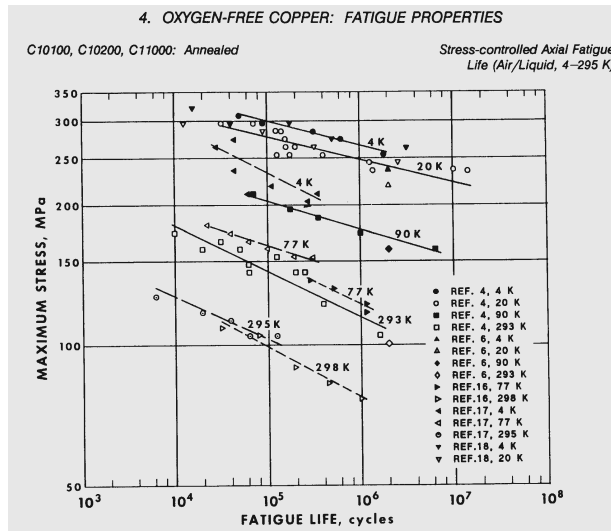

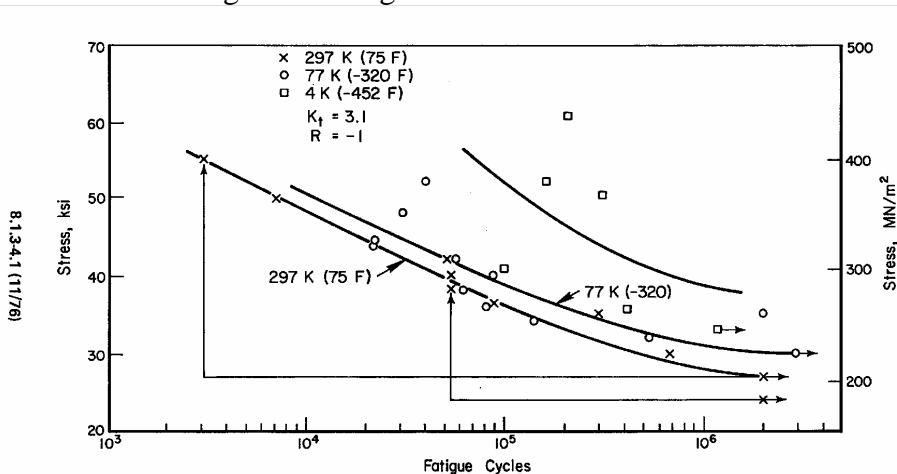Fig. 3.3-1 Fatigue curve for Annealed Cu

Fig. 3.3-2 Fatigue curve notched annealed 304L SS

59

3.4 Assembly Preload Requirement

Analysis series st25d369 and st25d367 are used to determine the mechanical preload requirements and operating stresses for the SS and Ti winding core magnet configurations, respectively. The external shell pressure P at outer radius R, is required to push the shell into a zero circumferential stress state (i.e., as it exists just after welding and before the orthogonal ram sets are relaxed). This can be converted to a ram force by integrating the pressure over a ±45° arc at the shell outer radius:

$$\text{Ram Force per meter} = \int P \, R \, \cos(\theta) \, d\theta = (2)^{0.5} PR$$

The shell outer radius is 0.381 m for this shielded Case II design, and the pressure is 13.5 MPa for the Ti winding core, and 19 MPa for the SS winding core. This results in a ram force of 7.3 MN/m for the Ti winding core and 10 MN/m for the SS winding core.

Chapter 8: Stability[36]

VIII.1 EXECUTIVE SUMMARY

Since the previous study [1] of the stability of the AHF Case II conductor certain changes both in design of the winding, and in the definitions of the radiation pulse deposition have been made. The beam energy deposition has been calculated by Mokhov[37].They are specified in [2, 3]. In particular, the radiation pulse deposition was changed to $\Delta Q = 0.35$ J/kg, and the interval between shots was increased to 20 seconds. Another change is related to the fact, that now the inner bore tube is at the same time the inner wall of the He vessel, so for the purpose of the conductor stability analyses this surface shall be considered adiabatic.

Stability of the AHF conductor was evaluated using simple models.

The adiabatic heating of the conductor due to a single radiation pulse at $\Delta Q = 0.35$ J/kg [1] shows a temperature rise to 6.28 K.

In the case of a single radiation pulse for the winding pack permeated with 2% isochoric internal He thermal equilibrium is reached at 4.4 K.

For the design with a potted winding the 20 s interval between the pulses is sufficient to transfer all heat deposited during the radiation pulse into He through the outer surfaces of the winding.

VIII.2 ADIABATIC TEMPERATURE RISE

The simpliest analysis of the temperature rise in the SC cable during the radiation pulse depositing $\Delta Q = 0.35$ J/kg [1] is using adiabatic assumptions. Assuming that SC has tspecific heat of Cu (see

---

[36] AHF-MIT-ARadovinsky-012202-01, A.L. Radovinsky, "Stability of the AHF Case II Conductor Update," January 22, 2002

[37] Los Alamos Report LA-UR-02-0210, N.V. Mokhov and P.L. Walstrom, "Beam-Lens interaction study with MARS14," Nov 21, 2001

Addendum) we can find the temperature after the pulse, T_2, as a function of the temperature before the pulse, T_1, from equation,

(1) $$\int_{T_1}^{T_2} Cpcu(T)*dT = \Delta Q$$

Figure 1 shows adiabatic temperature rise due to a series of consecutive pulses separated by 20 s intervals. Note that during the first shot temperature rises from 4.2 K to 6.28 K.
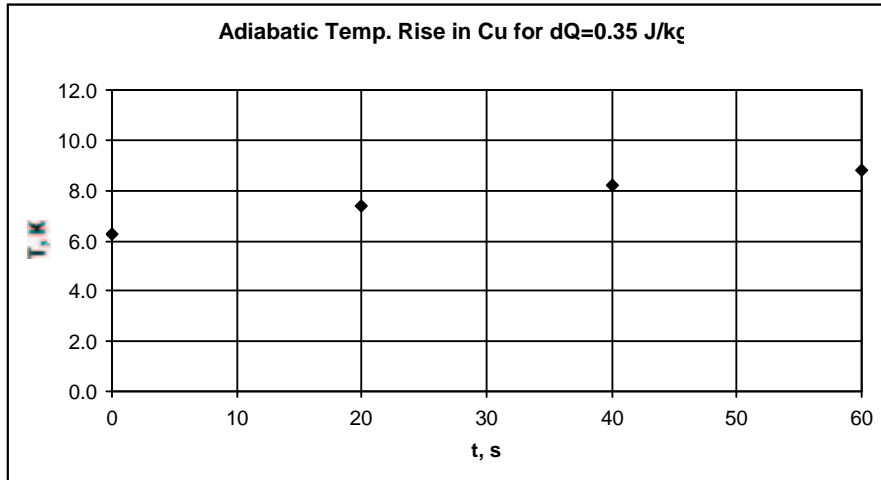

Fig. 1 Adiabatic temperature rise due to a series of consecutive pulses separated by 20 s intervals

Figure 2 shows adiabatic temperature rise after the first pulse from initial 4.2 K as a function of specific energy deposition, ΔQ.
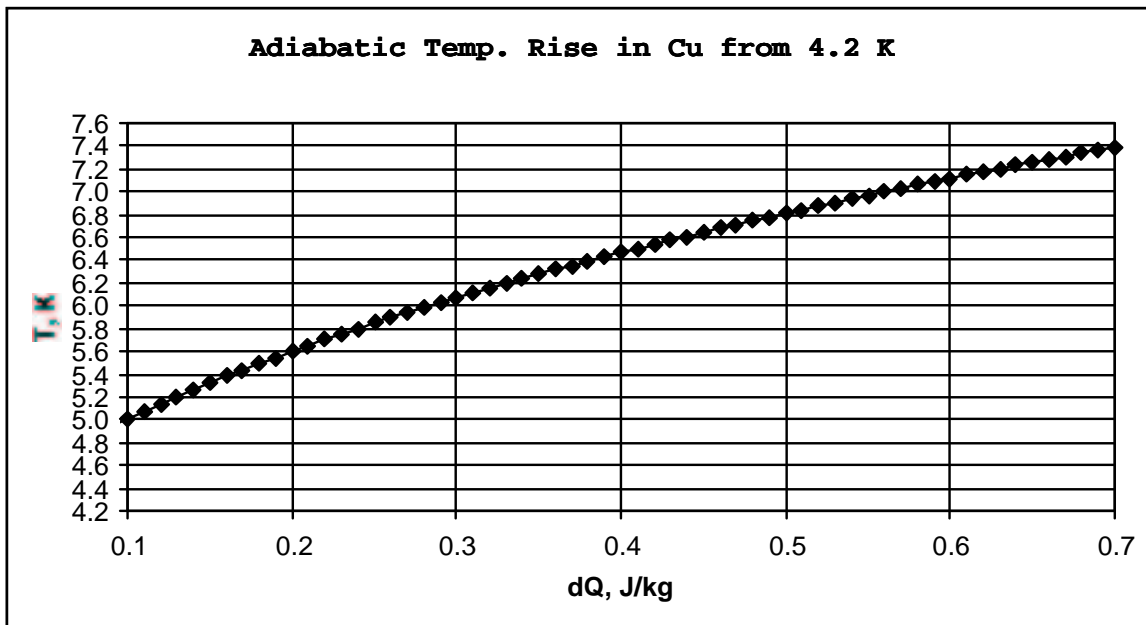

Fig. 2 Adiabatic temperature rise after the first pulse from initial 4.2 K
as a function of specific energy deposition, ΔQ

VIII.3 HELIUM PERMEATED DESIGN

To evaluate the effect of the radiation pulse in case of a winding pack permeated with 2% internal He the following equation was used,

$$(2) \qquad h^{He}(T_\infty) - h^{He}(T_0^{He}) = -\frac{W * h * Dcu}{0.02 * 1.02 * (W + 2 * Thti) * (h + 2 * Thti) * Dhe} \int_{T_0^{Cu}}^{T_\infty} Cpcu(T) * dT$$

Here on the left side we have the change of enthalpy in the helium due to temperature growth from $T^{He}_0 = 4.22$ K to T_∞ calculated at constant density, $Dhe = 125$ kg/m^3 using subroutines of a computer program TOKSCPF [4]. On the right side there is an equivalent enthalpy recalculated from energy lost by copper due to cooldown from $T^{Cu}_0 = 6.28$ K to the same, final temperature, T_∞.

Figure 3 shows that the solution of equation (2) is about $T_\infty = 4.4$ K.
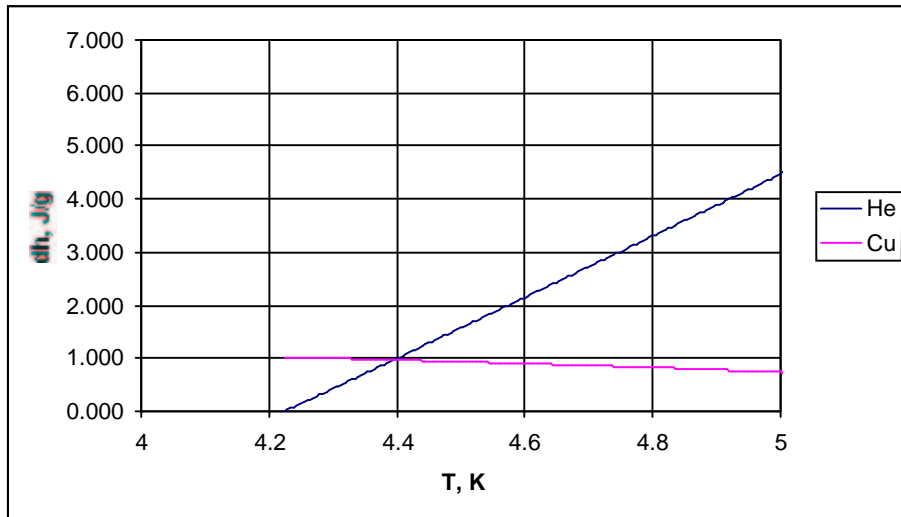

Fig. 3 Graphic solution of equation (2)

POTTED DESIGN

To evaluate the adequacy of heat exchange through the He-facing surface of a potted winding a simple 1D model was developed, and solved using Mathematica software package. The model is shown in Fig. 4. The unknowns are seven temperatures shown in Fig.4. Temperature distribution between the surfaces is assumed to be linear. Heat flux from the He-facing surface into He is calculated by formula

$$q = \min[2000, 14919 * (T-4.2)^{1.67}], [W/m^2]$$

where T is Tho or Thi for outer and inner surface, respectively. This formula is valid for (T-4.2)<0.8 K which showed to be fulfilled in the solution. The adiabatic boundary condition at the inner bore tube is forced by constant temperature, Tssl, through the the thickness of the SS layer.
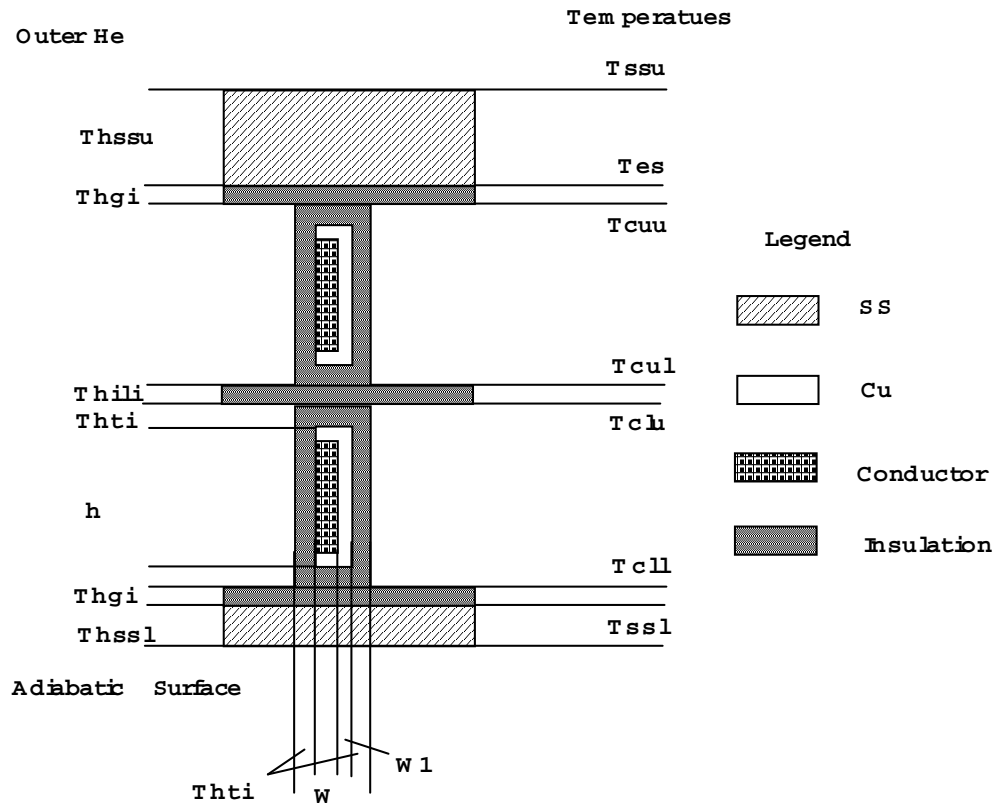
Fig. 4 The model for heat transfer calculations

The following dimensions and initial conditions were used.
H=16 mm, W=2.6 mm, W1=1 mm, Thti=Thili=Thgi=0.25 mm, Thssu=20 mm, Thssl=3.17 mm.
At t=0 s: Tcuu=Tcul=Tclu=Tcll= 6.28 K, Tssu=Tes=Tssl=4.98 K. The latter reflect the adiabatic temperature rise in SS calculated by a formula similar to (1).

Figures 5 show the anchor temperatures as a function of time for two consecutive pulses. The initial conditions for the second pulse are recalculated using (1) from temperatures corresponding to t=20 s after the first pulse. However, since all the final temperatures are essentially 4.2 K, the difference between the temperatures at the ends of the pulses is negligible. At the 'hottest', adiabatic end of the model temperature ratcheting based on two periods is 0.015 K.

Figure 6 shows heat transfer through the upper surface as a function of time.
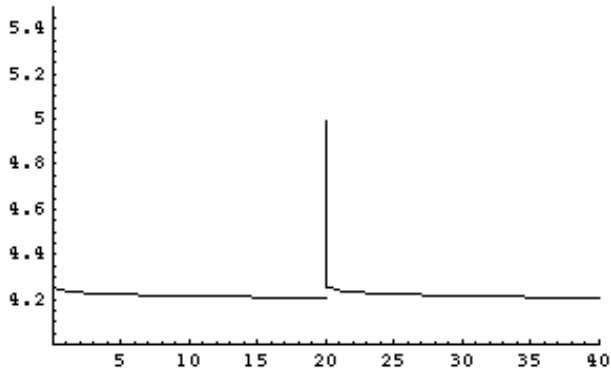
Fig. 5.a Tssu(t)

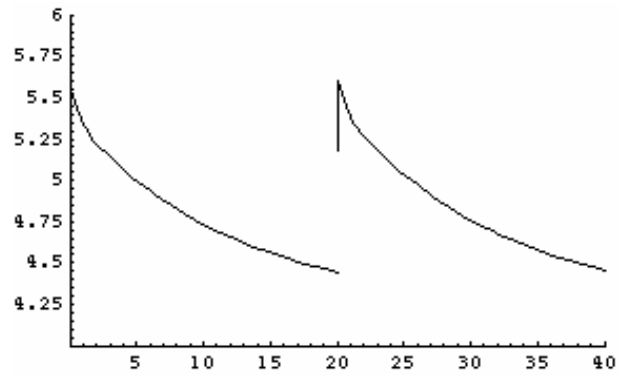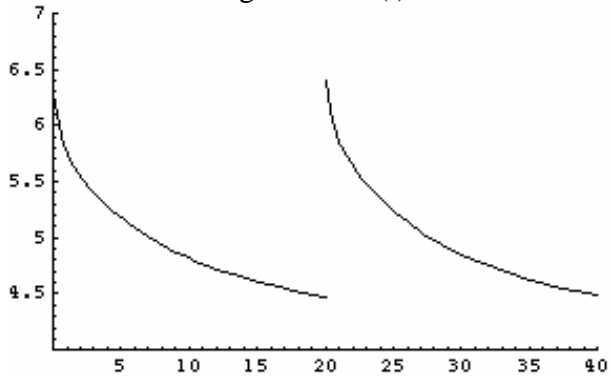Fig. 5.b Tes(t)

Fig. 5.c Tcuu(t)
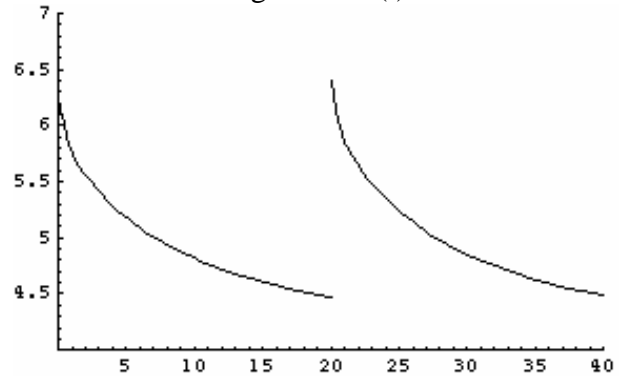
Fig. 5.dTcul(t)
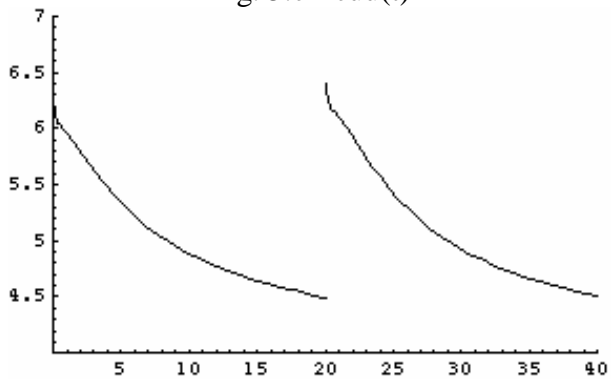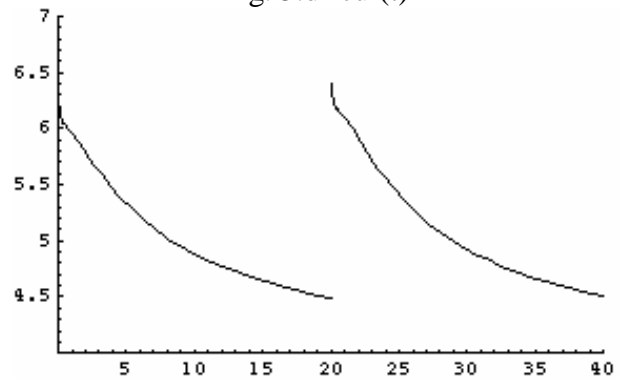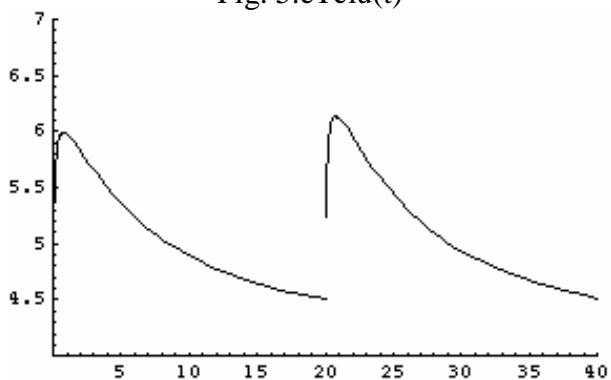

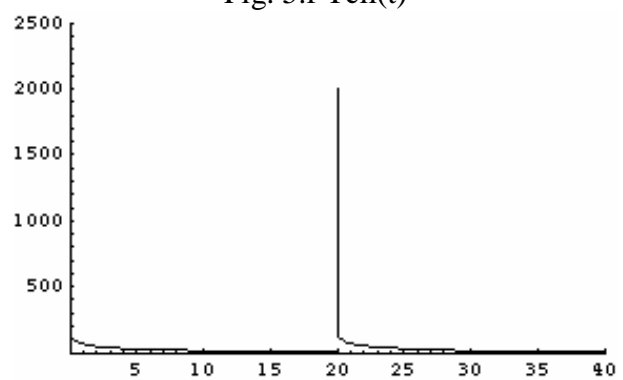Fig. 5.eTclu(t)

Fig. 5.f Tcll(t)

Fig. 5.g Tssl(t)

Fig. 6 qo(t), W/m2

64

References:

1. AHF-MIT-ARadovinsky-070300-01, A. L. Radovinsky, " Stability of the AHF Conductor," July 3, 2000

2. Joel H. Schultz, "AHF Quadrupoles Design Description Document, Rev. 0," January 1, 2002, AHF-MIT-JHSchultz-010902-01

3. N.V. Mokhov and P.L. Walstrom, "Beam-Lens interaction study with MARS14," November 21, 2001, Los Alamos Report LA-UR-02-0210,

4. Joel. H. Schultz, TOKSCPF, computer program.

Chapter 9: Protection

9.1. Executive Summary

Quench parameters were calculated by Smith[38] for the two options of using an external dump resistor or an external heater, using a method similar to a previous quench study[39] of the AHF Case I quadrupoles. Two quads are housed within one cryostat and are assumed to be in series, thus forming a doublet. Two protection approaches are considered: 1) dump resistor, and 2) internal heaters. In the case of using a dump resistor, the dump resistor is placed across both coils of the doublet following quench detection. Conductor and quads of this doublet are defined by Figures 1 and 2[40], respectively, along with supplementary information from Myatt[41], who provided the stored energy of 6.7 MJ per quadrupole.

The quench model divides each quad winding into elements with differential length, radius and azimuthal extent. The model includes the turn and layer insulation within the winding and also the stainless steel pole piece and outer mandrel, which are allowed to participate in heat sinking but not in eddy current conduction. The region between the end turns of adjacent quadrants is assumed to be a perfect thermal insulator, so the only boundary between adjacent quadrants for heat conduction is through the insulation along the shared straight lengths. Heat flux at all inner and outer boundaries of the quad (i.e., inside ri and outside ro) is assumed to be zero. The model solves numerically for the temperature of each element at each time step through simple energy balance. The program allows either a dump resistor or internal heaters as magnet quench-protection measures. These protection measures, which are an optional selection in the program, are initiated by the program after the coil resistive zone voltage rises above an input detection threshold, assumed throughout to be 0.2 V.

Heating due to ac and coupling losses in the windings is ignored. To simplify the calculations, the current sharing temperature in the NbTi cable is assumed to be 6.89 K everywhere. This value approximates the current sharing temperature at the average value of the field in the winding. Also, for now, magneto-resistance effects in the copper are ignored. Copper RRR is assumed to be 100.

An initial normal zone size consisting of a single conductor with a length of 9.9 cm was generally used in this study.

The conclusions of this analysis are:

---

[38] AHF-MIT-BASmith-022402-01, B.A. Smith, "Quench Calculation for AHF Case II Quad Doublet," February 24, 2002

[39] AHF-MIT-BASmith-070800-01

[40] AHF-MIT-JHSchultz-010902-01

[41] Email from L. Myatt, 2/21/02

- A 0.2-Ohm dump resistor will provide adequate protection to the coil, limiting the maximum temperature to about 77.4 K, while limiting the dump voltage to 1469 volts (7343 A * 0.2 Ohm), and the coil normal voltage to 104 V.

- Heaters sized to deliver about 5.3 watts per meter of conductor to each of layers 1 and 2 (or 20 kW per four-quadrant quad) are sufficient to protect the coils. Maximum resistive zone voltage about 800 V, and the hot spot temperature is 128 K.

9.2 Analysis

Modeled geometry

The turn cross-section used in this analysis is shown in Figure 1, and the cross-section of a single quadrant within the quad is shown in Figure 2. The red, cross-hatched portion of the cross-section in Figure 2 is filled with insulated-conductor-like material, which carries no current, but can participate in heat sinking. A 20 mm thick stainless steel mandrel (not shown in Figure 2) is located radially outward of the outer turns layer, and is assumed to be in intimate contact with the second layer turns.
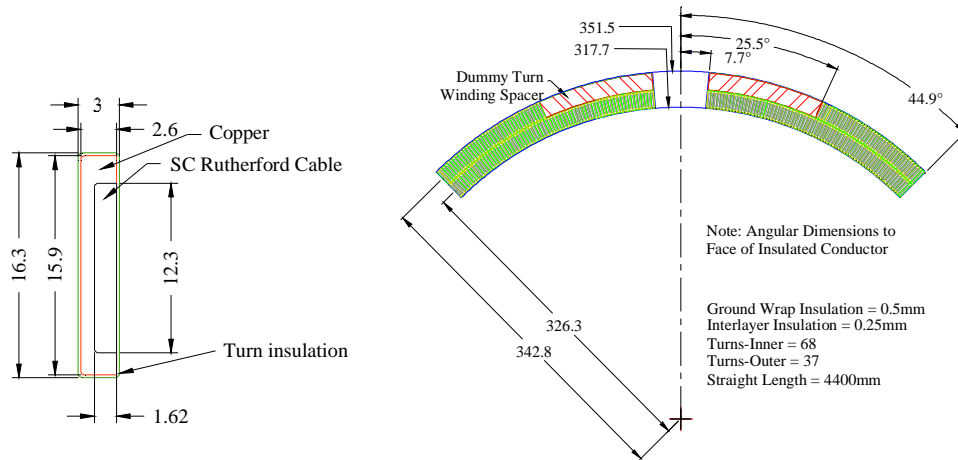

Figure 1
Cross-section of AHF Quadrupole Turn

Figure 2
Winding Cross-section, One Quadrant

Calculational approach and assumptions

Since the model element dimensions are allowed to exceed the turn dimension, material-averaged properties are taken for the thermal conductivity and specific heat. The program accesses stored, temperature-dependent values for copper, insulation and stainless steel. Time step size must be adjusted to be small enough such that the calculated temperature rise for any element at a given temperature is sufficiently small that the specific heat for the materials, which varies as a higher power

of the temperature, does not change greatly for the calculated temperature rise of the time step. This adjustment of the time step size is done manually.

Other assumptions in the model include RRR of the copper of 100. Magneto-resistance effects are ignored for now. Also, the two quads in the doublet are assumed to be in thermal isolation, but the adjacent quadrants within a quad are coupled via conduction through their common boundary.

The initial quench zone was chosen in the $_{.} = /4$ turn (Figure 2) as it continues into the end turn region, and about ¼ of the distance around the end turn. Since the end turns of each quadrant are insulated from the end turns in the adjacent quadrant, heat is not conducted from this region as rapidly as it is at a location along the straight length of the winding. In fact, initial normal zones located in the straight section tend to result in coil hot spots that migrate to this end-turn region.

Only one of the two quadrupoles in the doublet was modeled explicitly. This was done to keep calculation time to a minimum. In the case of dump resistor, the quench is assumed to propagate only in the coil in which the normal zone is initiated. In the case with winding heaters, however, the heaters should be energized in both quads upon detection of a quench in one quad. The heaters will then induce a quench in the second quad. Since the second quad is modeled only implicitly, the resistance in the second quad is assumed to follow that of the first but with a time delay associated with the quench detection time. A small error arises with this resistance assumption in the heater case because the resistance of the first quad is calculated based on the real rate of energy generation, which is, in turn, based on the current being at a specified value and a specified time. Current in the two quads, which are in series, must be the same. In the first quad, the resistance-time profile is precisely aligned with the current-time profile, but in the second quad, the resistance-time profile is slightly delayed relative to first, but it is nevertheless matched with the same current profile as is used in the first quad. Thus, the heating assumed in the second quad is slightly higher that it should be, because the current is no longer as high as it was in the case of the first quad when the resistance profile was calculated. As long as the detection voltage threshold is small enough to result in a small detection time delay the resulting error should be small.

9.3 Results

Results for three different protection schemes are presented:
1) dump resistor
2) winding heaters

In all cases, the integral of $J_{Cu}^2 dt$ was found to be in close agreement with the predicted hot spot temperature. Also, the sum of the energies dissipated internally and in the dump resistor matches the stored energy of the doublet, 13.4 MJ. These are valuable checks that the program is working correctly.

Dump Resistor

For this case a 0.2 dump resistor is placed across the doublet following quench detection. With a total doublet energy of 13.4 MJ, the dump resistor should be placed external to the doublet cryostat. For an initial normal zone size of 9.9 cm, the quench is detected in about 58 ms, and the dump is initiated. At the initiation of the dump, the 0.2 dump resistor will develop a voltage of 1469 volts.

Figures 3-5 show the current decay, coil normal zone voltage, and selected magnet temperatures, including the hot spot temperature in the winding. The normal zone voltage peaks at 104 V. The hot spot temperature is limited to 77.4 K. With the dump-resistor-protection scheme, the total amount of energy dissipated in the single quad absorbing the energy in the doublet is about 1.02 MJ, or 7.6% of the total doublet stored energy. An adiabatic calculation shows that when 1.02 MJ are dumped into a single quad (4 quadrants), the heat capacity of the quad (copper plus steel) is sufficient to limit the final equilibrium temperature to about 27 K. As can be seen in Figure 8, the steel mandrel and pole elements lag significantly in temperature rise due to the lower thermal conductivity and higher specific heat of steel compared with copper, and the thermal resistance of the coil insulating materials. Indeed, this is the reason that the hot spot and adjacent element temperatures peak in value and then fall slightly as the current dies away. Heat is being conducted from the hotter elements into the balance of the magnet, including the steel. The 0.2   dump resistor appears to provide a reasonable compromise between coil-temperature rise and dump voltage for the Case II quad doublet design.

Winding Heaters

Winding heaters offers an alternative protection solution to the use of dump resistors. The disadvantage of this approach is that the winding now must absorb the entire energy of the doublet, rather than dissipating a large fraction of the energy in an external dump resistor. This results in higher winding temperatures and longer cooldown times following quench. The benefit of this approach, however, is that the winding temperature gradients are much smaller than for the dump resistor case, since the heaters cause all coil-section temperatures to rise uniformly after quench detection. This results in lower thermal stresses in the winding. The plots shown in Figures 6-8 provide the results for this study. In this approach heaters are placed between the two radial winding layers. A more practical approach would be to have the heaters placed in the outer mandrel steel, but the quench code is not written to accommodate heat conduction in this fashion. The heaters are assumed to be capable of delivering about 5.3 W/m of conductor into each of the turns of layer 1 and layer 2. This value has not been optimized. With an initial normal zone of 9.9 cm, the quench is detected at 58 ms, and the heaters are energized. The winding hot spot temperature with heater protection climbs to 130 K (Figure 8), and the normal zone voltage peaks at about 800 volts (Figure 7). As with the dump resistor case, the temperature in the steel lags considerably. If the heaters are shut off after about 5 seconds, each winding temperature would ultimately fall to an equilibrium temperature of 48 K in both quads. This is calculated from the the adiabatic absorption of the doublet stored energy (13.4 MJ) plus the heater energy (102 kJ in 5 s by the thermal mass of the winding plus steel.
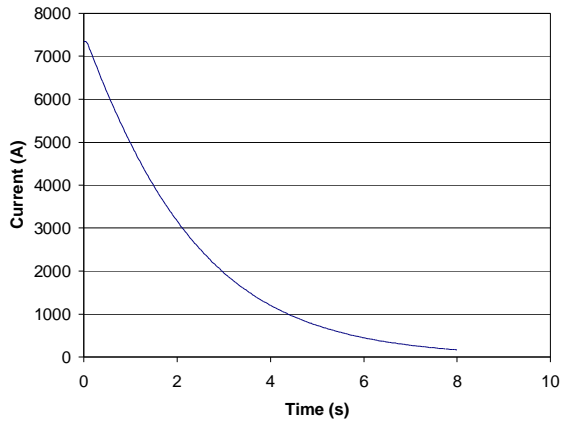
Figure 3
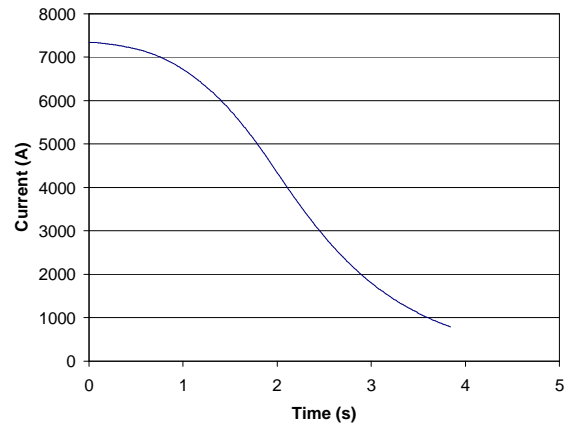Current Decay after Quench
and Dump with R_{dump} = 0.2 Ohm

Figure 6
Current Decay after Quench for Case with
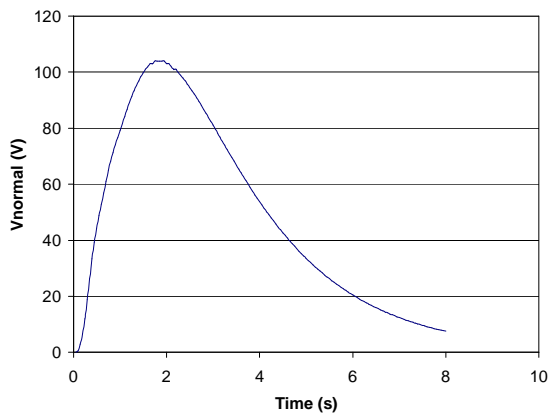Winding Heaters

Figure 4
Coil Resistive Zone Voltage after Quench
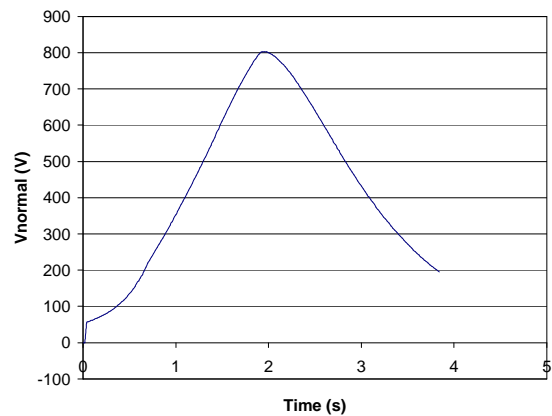and Dump with R_{dump} = 0.2 Ohm

Figure 7
Coil Resistive Zone Voltage after Quench for Case
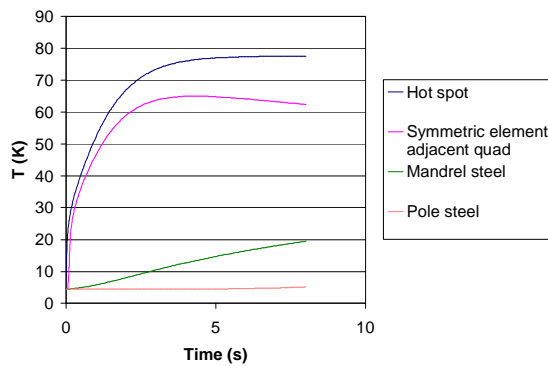with Winding Heaters

Figure 5
Hot Spot and Other Temperatures after Quench
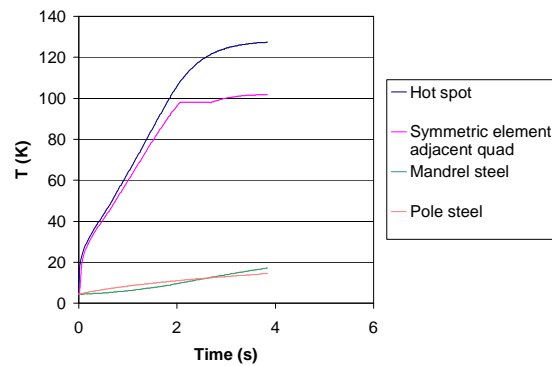and Dump with R_{dump} = 0.2 Ohm

Figure 8
Hot Spot and Other Temperatures after Quench for
Case with Winding Heaters

Chapter 10: Conclusions

The design description and final report document integrates coil dimensions and performance for the Case II quadrupole magnet system.

A conceptual design of a Case II quadrupole doublet has been completed that meets the specifications for the Advanced Hydrotest Facility. The designs was based on cable-in-channel NbTi conductors, cooled by liquid helium, similar to the Hall C quadrupoles in the Thomas Jefferson National Accelerator Facility. An iron yoke, absent in the previous year's design, was included in order to eliminate field and force coupling between Case I and Case II magnet systems.

The winding is precompressed radially and azimuthally by an outer 3 cm steel can with an assembly preload of 7.3 MN/m and a low thermal thermal contraction titanium pole piece. Structural analysis shows the steel can, titanium poles, and copper conductor within their stress allowables. Compression in the insulation system is everywhere below 180 MPa. The analysis also indicates that a slip-plane between the insulation and the titanium pole-piece would eliminate tension everywhere in the winding.

A stainless steel cold-warm rod assembly supports cold mass gravity loads..Cold-warm gravity supports for the cold mass. The relative contraction of the assembly and the cold mass is taken up in a vacuum bellows with adjusting nuts for magnetic centering of the cold mass in the cryostat. Each rod terminates in a spherical ball and clevis pin that are rigidly attached to each other, and that can slide along and rotate about the axis of the pin through the adapter bearing. These support unbalanced magnetic as well as gravity loads.

Three-dimensional field leakage analyses showed that the field due to the Case II quadrupoles appearing anywhere in the beam line, focused by the Case I quadrupoles, is under half a gauss, at least an order of magnitude less than the allowable limit of 10 gauss. Extensive calibration of two methods of field calculation was required to obtain this solution.

Systematic field harmonic errors, due to coil design rather than tolerances, meet the specifications for systematic error. The 6th and 10th harmonics are less than 10^{-4}, as are all other higher harmonics.

The use of a collimator to reduce coil heating lowers the peak energy deposition in the first quadrupole to $\Delta Q=0.35$ J/kg. The interval between shots was also increased to 20 seconds. These two improvements greatly improved the feasibility of a NbTi winding. The peak temperature after a single pulse is 6.28 K. Temperature ratcheting on successive pulses, separated by 20 seconds, is negligible, even with cooling only on the outside of the outer steel can.

Analysis of the design showed that it meets structural, protection, and long-term heat removal allowables with margin in all of the components. With the addition of a collimator, the designs also have margin with respect to stability against nuclear heating and are no longer heated into the superconductor current-sharing regime, even on a transient basis. However, it is unclear whether design and calculational uncertainties guarantee stability in a coil based on NbTi. A radical magnet design

solution that should solve the problem, but increase magnet cost, is the use of Nb_3Sn, instead of NbTi, which would improve the energy margin by an order of magnitude. The investigation of this design option is the next task to be completed in the study of Case II quadrupoles.

A quadrupole doublet can be protected either by an external dump resistor, using a single pair of leads or by an internal heater. Using an external resistor, the terminal-terminal voltage is 1,470 V and the peak temperature is 77 K. With an internal heater, the internal resistive voltage is 800 V and the peak temperature is 130 K.

Appendix: Log of AHF Memoranda

AHF-LANL-PWalstrom-040901-01, Peter Walstrom, " Case 2 Iron Yoke Specifications," April 9, 2001
AHF-MIT-LMyatt-042001-01, R. Leonard (Len) Myatt and Joel H. Schultz, "Restatement of LANL FY01 Guidelines as Design Specifications," April 20, 2001
AHF-MIT-LMyatt-042501-01, R. Leonard (Len) Myatt, " Effectiveness of Asymmetric Shielding in Case II Quads," April 25, 2001
AHF-MIT-LMyatt-050601-01, R. Leonard (Len) Myatt, "Shielding Case II Quads with 3D Iron," May 6, 2001
AHF-MIT-LMyatt-051101-01, R. Leonard Myatt, "Shielding Case II Quads with 3D Iron, Part II," May 11, 2001
AHF-MIT-LMyatt-053101-01, R. Leonard (Len) Myatt, "Analysis of Shielding Results," May 31, 2001
AHF-MIT-LMyatt-060401-01, R. Leonard Myatt, "Analysis of Shielding Results," June 4, 2001
AHF-MIT-LMyatt-062001-01, R. Leonard Myatt, "2D Parametric Shielding Study," June 20, 2001
AHF-MIT-LMyatt-062201-01, R. L. Myatt, "Shielding Case II Currents, Part II," June 22, 2001
AHF-MIT-JHSchultz-0713-01, Joel H. Schultz, "MIT Informal Proposal – AHF Prototype Development Task," July 13, 2001
 AHF-MIT-LMyatt-071601-01, R. Leonard (Len) Myatt, "2D Turn-Count Optimization for Shielded Case II Quads," July 16, 2001
AHF-MIT-LMyatt-0720-01, R. Leonard (Len) Myatt, "Fringe fields at the Case II Beam, Revised Winding Radius," July 20, 2001
AHF-MIT-LMyatt-0723-01, R. Leonard Myatt, "2D Turn-Count Optimization for Revised Case II Quad Shield," July 23, 2001
AHF-MIT-LMyatt-073001-01, R. Leonard Myatt, "Proposed modeling approximation for Future End-Turn Optimization Study," July 30, 2001
AHF-MIT-LMyatt-080201-01, R. Leonard (Len) Myatt, "Alternate Modeling Approximation for Future End-Turn Optimization Study," August 2, 2001
AHF-MIT-LMyatt-081201-01, R. Leonard Myatt, "Alternate Modeling Approximation for Future End-Turn Optimization Study," August 12, 2001
AHF-MIT-LMyatt-082601-01, R. Leonard (Len) Myatt, "End-Turn Optimization Study #1," August 26, 2001
AHF-MIT-LMyatt-090301-01, R. Leonard (Len) Myatt, "Case II Quad Conductor Strain from End-Turn Bend Radius," September 3, 2001
AHF-MIT-LMyatt-090701-01, R. Leonard (Len) Myatt, "Case II Field Errors the LANL-Way," September 7, 2001
AHF-MIT-LMyatt-091901-01, R. Leonard (Len) Myatt, "2.5D Stress Analysis of Shielded Case II Quadrupole," September 19, 2001
AHF-MIT-LMyatt-092601-01, R. Leonard Myatt, "2D Spacer Optimization for Shielded Case II Quads," September 26, 2001
AHF-MIT-LMyatt-100301-01, R. Leonard (Len) Myatt, "Case II Field Errors of Re-Optimized Straight-Length," Oct 3, 2001
AHF-MIT-LMyatt-102601-01, R. Leonard (Len) Myatt, "Re-Optimized End Turns in the Case II Quadrupole," October 26, 2001
AHF-MIT-ARadovinsky-103101-01, A.L. Radovinsky, "Progress with VF OPERA3D," October 31, 2001
AHF-MIT-ARadovinsky-111201-01, A.L. Radovinsky, "Matching VF vs. ANSYS Results," November 12, 2001

AHF-MIT-JHSchultz-010902-01, Joel H. Schultz, "AHF Quadrupoles Design Description Document, Rev. 1," January 9, 2002

AHF-MIT-ARadovinsky-011502-01, A.L. Radovinsky, "Case I Shielding from Case II Coil," January 15, 2002

AHF-MIT-ARadovinsky-012202-01, A.L. Radovinsky, "Stability of the AHF Case II Conductor Update," January 22, 2002

AHF-MIT-BASmith-022402-01, B.A. Smith, "Quench Calculation for AHF Case II Quad Doublet," February 24, 2002

AHF-MIT-JHSchultz-022602-01, Joel H. Schultz et al, "Advanced Hydrotest Facility (AHF)Case II Quadrupole Design Study Final Report," February 26, 2002